# MSc Thesis

## A Lean Testing Methodology for the Inertia Parameters of Small Rocket Stages

D. Possamai

Delft University of Technology

TU Delft

# MSc Thesis

## A Lean Testing Methodology for the Inertia Parameters of Small Rocket Stages

by

D. Possamai

to obtain the degree of Master of Science
at the Delft University of Technology,
to be defended publicly on Monday January 1, 2024 at 10:00 AM.


| | | |
|---|---|---|
| Student number: | 5471923 | |
| Project duration: | January 9, 2023 – September 29, 2023 | |
| Thesis committee: | Dr. J. Sodja, | TU Delft, supervisor |
| | I. Uriol Balbin | TU Delft |
| | Stephan Schmid | RFA Portugal |



| | |
|---|---|
| Cover: | Redshift OTV Render by RFA |
| Style: | TU Delft Report Style, with modifications by Daan Zwaneveld |

An electronic version of this thesis is available at `http://repository.tudelft.nl/`.


TU Delft

# Abstract

This thesis presents the development, analysis, and testing of a comprehensive testing methodology for determining the mass, Center of Gravity (CoG), and principal Moments of Inertia (MoI) of small rocket stages. The methodology comprises five sequential tests, encompassing both static and dynamic procedures. The two static tests introduce innovative adaptations of established techniques. The multi-point weighing (MPW) method for the measurement of mass and horizontal CoG coordinates is modified into a suspended version, broadening its applicability, while the suspension method, measuring the CoG height, evolves into the Bifilar Suspension (BS) method, enhancing robustness and safety with the inclusion of an additional rope. The dynamic tests measure the body's MoI values, with the Bifilar Pendulum (BFP) method for roll MoI and the Compound Pendulum (CP) method for pitch and yaw MoI. Efficiency and cost-effectiveness are integral to the methodology, resulting in a streamlined testing campaign requiring minimal time and resource investment.

An analytical uncertainty analysis assessment explores the propagation of uncertainties in the employed methods, highlighting the impact of several parameters on the combined uncertainty on the results. Additionally, an analytical expression for the amplitude-dependent errors in dynamic tests is derived, providing a useful tool to predict such nonlinear effects. A simulation study numerically verifies the results from the uncertainty analysis, as well as the solution equations used for the methods.

The methodology's validation is carried out through three consecutive test campaigns. The results demonstrate the capability of the static tests to consistently determine mass and CoG coordinates with limited uncertainties. The BFP method achieves satisfactory accuracy, although unexpected deviations from the numerical predictions are observed. As for the CP method, multiple factors exert a large influence on the accuracy of the final results. Among the ones analyzed in this work are: the length of the ropes, the radius of gyration of the body, and the accuracy in the frequency measurement. Moreover, in both dynamic tests the type of suspension system is found to have an effect on the accuracy of the measurements.

While not all the intended objectives have been achieved, this thesis contributes to the understanding of testing methodologies for rocket stages, and offers insights into achieving accurate and precise results with simple and cost-effective methods.

# Contents

# List of Figures

# List of Tables

# Nomenclature

## Abbreviations

| Abbreviation | Definition |
|---|---|
| BFP | Bifilar Pendulum |
| BS | Bifilar Suspension |
| CoG | Center of Gravity |
| CP | Compound Pendulum |
| ESPA | EELV Secondary Payload Adapter |
| EOM | Equation Of Motion |
| FFT | Fast Fourier Transform |
| GNC | Guidance, Navigation, and Control |
| GUM | Guide to the Expression of Uncertainty in Measurement |
| MoI | Moment of Inertia |
| MPW | Multi-Point Weighing |
| OTV | Orbital Transfer Vehicle |
| PoI | Product of Inertia |
| RFA | Rocket Factory Augsburg |
| UAV | Unmanned Aerial Vehicle |

## Symbols

| Symbol | Definition | Unit |
|---|---|---|
| $a$ | Mounting radius of the ropes on the structure in the MPW method | [$mm$] |
| $A$ | Pendulum oscillation amplitude | [$^\circ$] |
| $b$ | Mounting radius of the ropes on the body in the MPW method | [$mm$] |
| $B_i$ | i-th attachment point of rope on body | |
| $D$ | CoG misalignment error in multi-filar pendulum | [$mm$] |
| $D^+$ | Dimensionless CoG misalignment error in multi-filar pendulum | |
| $err_I$ | Difference between the MoI value found through simulation and the one calculated by the CAD software on the model | [%] |
| $err_m$ | Difference between the mass value found through simulation and the one calculated by the CAD software on the model | [%] |
| $err_{x_G}$ | Difference between the $x$ coordinate of the CoG found through simulation and the one calculated by the CAD software on the model | [%] |
| $err_{y_G}$ | Difference between the $y$ coordinate of the CoG found through simulation and the one calculated by the CAD software on the model | [%] |

| Symbol | Definition | Unit |
|---|---|---|
| $err_{z_G}$ | Difference between the $z$ coordinate of the CoG found through simulation and the one calculated by the CAD software on the model | [%] |
| $f$ | Frequency of oscillation | $[Hz]$ |
| $F_A$, $F_B$ | Horizontal forces generating the restoring torque in bifilar pendulum | $[N]$ |
| $f_{exp}$ | Expected oscillation frequency | $[Hz]$ |
| $g$ | Gravitational acceleration | $[\frac{mm}{s^2}]$ |
| $G'_h$ | Perpendicular projection of the CoG onto the measurement plane | |
| $G''$ | Vertical projection of the CoG onto the MPW measurement plane with a tilted body | |
| $G'$ | Perpendicular projection of the CoG onto the MPW measurement plane with a tilted body | |
| $G$ | Center or gravity | |
| $h$ | Vertical distance between the rope attachment points on the body and on the structure in the MPW method | $[mm]$ |
| $I$ | Moment of Inertia | $[kg \cdot mm^2]$ |
| $I_{\zeta CAD}$ | MoI obtained from using the CAD value of $\zeta$ to solve the equation for the simulated problem, instead of the $\zeta$ coming from the CoG simulations | $[kg \cdot mm^2]$ |
| $I_{CAD}$ | MoI calculated by the CAD software on the CAD model of the body | $[mm]$ |
| $I_P$ | MoI about the pendulum axis in the compound pendulum method | $[kg \cdot mm^2]$ |
| $I_{stab}$ | MoI value obtained from converged frequency value | $[kg \cdot mm^2]$ |
| $k_t$ | Torsional stiffness | $[\frac{N \cdot m}{rad}]$ |
| $L$ | Rope length | $[mm]$ |
| $m$ | Mass of the body | $[kg]$ |
| $M_0$ | Initial mass | $kg$ |
| $M_p$ | Propellant mass | $kg$ |
| $m_{CAD}$ | Mass calculated by the CAD software on the CAD model of the body | $[kg]$ |
| $m_{susp}$ | mass of the specimen, determined through the suspension method | $[kg]$ |
| $N$ | Sample size | |
| $P_i$ | Rope tension measured by the load cell | $[N]$ |
| $R$ | Common rope mounting radius for multi-filar pendulum when the top and bottom radii are equal | $[mm]$ |
| $R^2$ | Coefficient of determination to assess goodness of linear regression | |
| $R_A$, $R_B$ | Horizontal distance of the rope attachment point to the CoG in multi-filar pendulum | $[mm]$ |
| $r_{CoG}$ | Distance of the CoG from the fulcrum in the balancing method | $[mm]$ |
| $r_{cw}$ | Position of the counterweight in the balancing method | $[mm]$ |
| $t_p$ | T-factor for student distribution | |
| $t_{acq}$ | Total acquisition time | $[s]$ |
| $t_{test,i}$ | Total time required for running a test the i-th time | $[s]$ |
| $t_{tot}$ | Total time required for running a test $N$ times | $[s]$ |
| $T_z$ | Torque about the $z$ axis | $[N \cdot m]$ |
| $v$ | Velocity | $[\frac{m}{s^2}]$ |

| Symbol | Definition | Unit |
|---|---|---|
| $v_e$ | Exhaust velocity | $[\frac{m}{s^2}]$ |
| $W_{cw}$ | Weight of the counterweight in the balancing method | $[N]$ |
| $w_i$ | Weight associated with the i-th result, used for inverce-variance weighting | |
| $W_i$ | Vertical component of measured load at the i-th load cell | $[N]$ |
| $W_{tot}$ | Total weight | $[N]$ |
| $\bar{x}$ | Mean value of quantity $x$ | |
| $x_{best}$ | Best estimate of an uncertain quantity | |
| $x_G$ | $x$ coordinate of CoG | $[mm]$ |
| $x_{G,CAD}$ | $x$ coordinate of the CoG calculated by the CAD software on the CAD model of the body | $[mm]$ |
| $x_{G,susp}$ | $x$ coordinate of CoG, determined through the suspension method | $[mm]$ |
| $x_i$ | i-th sample value of quantity $x$ | |
| $x_{max}$ | Maximum dimension of the body in $y$ direction | $[mm]$ |
| $y_G$ | $y$ coordinate of CoG | $[mm]$ |
| $y_{G,CAD}$ | $y$ coordinate of the CoG calculated by the CAD software on the CAD model of the body | $[mm]$ |
| $y_{max}$ | Maximum dimension of the body in $y$ direction | $[mm]$ |
| $z_G$ | $z$ coordinate of CoG | $[mm]$ |
| $z_{G,CAD}$ | $z$ coordinate of the CoG calculated by the CAD software on the CAD model of the body | $[mm]$ |
| $z_{max}$ | Maximum dimension of the body in $z$ direction | $[mm]$ |
| $\alpha_i$ | Inclination of i-th rope with respect to the direction of gravity | [°] |
| $\beta$ | Body tilt around the $x$ axis in the suspension method | [°] |
| $\Delta f$ | Frequency resolution of Fast Fourier Transform | $[Hz]$ |
| $\Delta f_{shift}$ | Frequency shift due to motion amplitude | $[Hz]$ |
| $\delta q$ | Uncertainty on quantity $q$ | |
| $\delta x_G$ | Deviation from correct measurement of $x$ component of the CoG due to body tilt in MPW | $[mm]$ |
| $\delta y_G$ | Deviation from correct measurement of $y$ component of the CoG due to body tilt in MPW | $[mm]$ |
| $\zeta$ | Compound pendulum arm length. | $[mm]$ |
| $\zeta_{CAD}$ | Compound pendulum arm length as measured directly on the CAD model | $[mm]$ |
| $\zeta_{opt}$ | Value of compound pendulum arm length that minimizes the combined uncertainty on the MoI | $[mm]$ |
| $\zeta_{opt,\zeta}$ | Value of compound pendulum arm length that reduces the $\zeta$-dependent uncertainty component to 0 | $[mm]$ |
| $\eta$ | Body tilt about the $x$ axis in multi-point weighing | [°] |
| $\theta_i$ | Short notation for the partial derivative of a quantity r with respect to a variable $x_i$: $\frac{\partial r}{\partial x_i}$ | |
| $\theta$ | Horizontal rotation angle about the CoG in multi-filar pendulum | $[rad]$ |
| $\ddot{\theta}$ | Angular acceleration of the body about the vertical axis going through the CoG | $[\frac{rad}{s^2}]$ |
| $\nu$ | Degrees of freedom | |
| $\xi$ | Body tilt about the $y$ axis in multi-point weighing | [°] |
| $\rho$ | Radius of Gyration | $[mm]$ |
| $\sigma_x$ | Sample standard deviation | |
| $\sigma_{\bar{x}}$ | Standard deviation of the mean | |
| $\tau$ | Period of oscillation | $[s]$ |

| Symbol | Definition | Unit |
|---|---|---|
| $\varphi$ | Pendulum angular displacement | $[rad, \circ]$ |
| $\varphi_G$ | Dimensionless CoG misalignment factor in multi-filar pendulum | |
| $\omega$ | Angular velocity | $[\frac{rad}{s}]$ |

# 1 Introduction

The main focus of this study is the development of a lean testing methodology for the determination of the inertia properties, or inertia parameters, of an Orbital Transfer Vehicle (OTV). This chapter provides some background on the problem, states the research questions, and discusses the methodology employed.

## 1.1. Background

The past few decades have seen a meteoric rise in the number of space launches, due to an increasing number of companies and agencies joining a sector that used to be dominated by just a few. In 2022, a record-breaking 180 rockets left the earth [1], bringing satellites to orbit for purposes such as communication, navigation, remote sensing, and scientific research. To place these satellites in their desired orbits, specialized spacecrafts called *Orbital Transfer Vehicles* (OTVs) are often used. These have the specific aim of bringing a payload from its current orbit to an orbit of destination. This is achieved through orbital maneuvers, which involve burning propellant to modify the orbit and reach either a transfer orbit or the destination orbit.

The first attempt at developing a vehicle of this kind happened in the early 1970's with *Space Tug* [2], a joint effort between Boeing and NASA to provide the agency with a flexible, modular vehicle that could be adapted to a variety of missions, from in-orbit servicing to lunar landing. Most of the vehicle was manufactured out of various aluminum alloys and was roughly 10.8 m tall and 4.3 m in diameter, with a fueled mass 20,600 kg. The project's funding was eventually cut in 1972 and never fully realized [3].

More recent examples tend to be much smaller in size and capabilities. This can be attributed largely to the much lower weight and volume of current-day payloads. For example, the Skyrora Space Tug is an OTV currently under development at UK-based company Skyrora. It features a height of 2 m and a diameter of 1.9 m and weighs 530 kg when fueled. It can provide 3.5 kN of thrust[1].

This thesis concerns itself with *Redshift*, the OTV currently in the final stages of development at Rocket Factory Augsburg (from here on referred to as RFA). The design of the vehicle is confidential, but for the purpose of this work, a qualitative description of its geometry is warranted. The OTV is built like a hollow truncated cone. At the top of this cone the payload can be mounted, while, inside the cone, the engine and propellant tanks are assembled symmetrically around the vertical axis. The total wet mass is of about 350 kg. The vehicle's envelope can be considered as a cube with edges of approximately 2 m, with a vehicle diameter of approximately $\frac{5}{4}$ of its height.

The success of an orbital maneuver largely depends on the accurate knowledge of the vehicle's inertia parameters. These are its mass, Center of Gravity (CoG), Moments of Inertia (MoI), and Products of Inertia (PoI). This thesis deals with the experimental determination of the first three.

[1] Source: https://www.skyrora.com/space-tug/ (accessed on 14/03/2023).

The mass influences the amount of propellant required for a given maneuver. According to the ideal rocket equation $\Delta v = v_e ln \frac{M_0}{M_0 - M_p}$, where $\Delta v$ is the change in velocity, $v_e$ is the exhaust velocity, which depends on the type of propellant used, $M_0$ is the mass before the maneuver, and $M_p$ is the mass of the ejected propellant. If $M_0$ increases, $M_p$ must increase as well to maintain the same value of the ratio $\frac{M_0}{M_0 - M_p}$. It follows that, for a given value of $v_e$, more propellant is needed to accelerate a heavier vehicle by a certain $\Delta v$.

The CoG position is fundamental to determine the thrust direction. For orbital change maneuvers the thrust must be directed through the CoG, so that no unwanted rotation happens. If, however, the aim is to change the spacecraft orientation, the thrust must be off-center, so that it produces a torque around the CoG. Here, the vehicle's MoI values come into play. These express its resistance to changes in its rotational motion, and are therefore important to calculate the required thrust for such attitude change maneuvers. Additionally, they determine the vehicle's stability to external forces such as atmospheric drag.

Lastly, the PoI are a measure of the amount of dynamic imbalance displayed when the body rotates around a certain axis and make up, together with the MoI, the inertia tensor. However, the former are much smaller than the latter for the considered class of vehicles, since symmetric bodies have no PoI with respect to axes that lie on the plane of symmetry. More generally, for any body and any point $O$ inside or outside of it, it is possible to choose a reference system centered in $O$ such that the inertia tensor with respect to it will be diagonal, i.e., all PoI will be equal to 0. The axes making up this system take the name of principal axes [4], [5]. The principal axes of a body can often be inferred by studying its symmetries. If the body presents a plane of symmetry, any axis perpendicular to it is a principal axis. The object under investigation in this study, like many rocket stages, presents two orthogonal planes of approximate symmetry, intersecting at the roll axis. This means that two of the principal axes are easily identified as the ones perpendicular to said planes going through the CoG, while the third principal axis is the roll axis itself. The usual requirement for spacecraft control is the knowledge of the MoI with respect to the pitch, roll, and yaw axes. In this case, the pitch and yaw axes are not exactly coincident with the principal axes of inertia, but the balanced design of the vehicle still allows for the assumption that the PoI are negligible.

## 1.2. Problem Formulation

The easiest way to obtain the inertia parameters of a body is from its CAD model. The vast majority of vehicles produced nowadays have an associated 3D model, from which the CAD software can compute the inertia parameters. In general, however, these values will differ from the ones of the final product due to, among others, design adjustments and imperfections introduced during manufacturing and assembly. No guidelines to estimate the magnitude of these deviations could be found in literature. The values extracted from the CAD model are therefore acceptable as estimates during the design phase but, for operations, higher reliability is required. For this reason, the physical vehicle (or an engineering model) is tested to obtain the experimental values of its inertia parameters.

Inertia parameters testing (or inertia testing) can be challenging, especially for the many small businesses with limited resources and facilities of which the NewSpace sector is currently largely populated. Conventional methods are either very expensive, like the ones involving complex robotics, or highly time-consuming, like the many methods for CoG measurement which require multiple setup reconfigurations [6]. This forces a trade-off between the two most valuable resources for an emerging business: time and money. This issue prompted the search for a lean testing methodology specifically tailored to small rocket stages. Here, leanness is used as a term to encompass both time efficiency and cost-effectiveness.

As a result, the research question that this thesis tries to address is: *How can the practical evaluation of the mass, CoG position, and MoI about the roll, pitch, and yaw axes of the Redshift OTV be optimized in terms of time and cost, while ensuring that all results maintain a maximum uncertainty of 10%, and can the methods be adapted for use in the evaluation of other small rocket stages?*

To answer this question, the following sub-questions will be addressed:

1. How can the current methods for mass, CoG, and MoI testing be adapted and combined to mini-

mize the total hardware cost for testing on the Redshift OTV?
2. How can the total time required for testing for mass, CoG coordinates, and roll, pitch, and yaw MoI on the Redshift OTV be minimized?
3. What is the predicted impact of the expected error sources on the results?
4. How can the testing procedure be verified and validated?
5. How can the methods be easily adapted to other small rocket stages?

This thesis attempts to answer the above research question by carrying out the development, verification, and validation of a time and cost-optimized testing methodology for the mass, CoG, and MoI of an OTV, easily adaptable to other small rocket stages in the future. The procedure incorporates a combination of static and dynamic techniques selected based on the specified requirements, among which were accuracy, time, and cost-efficiency.

## 1.3. Approach to Research

One of the very first steps necessary to develop a testing campaign is to define a list of requirements. These were discussed with experts within the company and served to specify the most important drivers and constraints. Once the requirements were defined, a literature study phase was performed to investigate the most widely employed methods for inertia testing. During this phase, the reported advantages and disadvantages of each were identified, with particular attention to those expected to have the greatest influence on the fulfillment of the requirements. This led to a trade-off study that excluded some of the methods. The remaining methods were then adapted and combined, leveraging the advantages of each of them to develop a new, combined testing methodology, optimized for time and cost-efficiency. The influence of all parameters expected to impact the accuracy of the measurements was derived analytically.

To verify the methodology, a virtual dynamic simulation of the test campaign was performed. This also made it possible to perform a sensitivity study: small variations were introduced in some input parameters to verify the resulting change in accuracy. Finally, the validation phase took place. The developed test campaign was performed first on a payload adapter as a pre-validation step, then on the OTV primary structure, and lastly on a simple hollow square beam. The uncertainties on the results of all experiments were estimated through the previously derived analytical equations, and the calculated values were compared to those predicted by the CAD software to draw conclusions on the accuracy and applicability of each test.

The data collection was performed in three consecutive stages: simulation, pre-validation testing, and validation testing. The purpose of the first step was to verify the testing methodology's results against reliable values. The tests were run virtually on the CAD model of the object, while the CAD software's mass property estimation tools provided the reference values. It was assumed in these simulations that the body, ropes, and test rig all behave as rigid bodies. This assumption is further discussed in Chapter 4. In addition to the simulated tests, a sensitivity analysis was performed on each method, to determine how the results varied with slight changes in the inputs. This served to simulate inaccurate measurements and their overall impacts on the results. The virtual tests were performed on the CAD model of the same body used for the pre-validation step which followed. This choice allowed for immediate comparison between the simulation results and the first available experimental results.

The intermediate step served as a simplified validation, with less variables that could influence the results, hence allowing for a focused examination of the testing methodology itself and of its core criticalities. This required a specimen with a geometry comparable to the OTV's, but simple enough to make the identification of the most critical variables affecting the tests as straightforward as possible. An EELV Secondary Payload Adapter (ESPA) was selected for this purpose. Other than its relatively simple geometry, the body presents the advantage of being predominantly composed of the same aluminum alloy, which further simplifies the problem.

Lastly, the test campaign was conducted on the OTV primary structure to validate the testing methodology for the specific use it was developed for. Some of the data from this phase is not explicitly mentioned in the text, as it needs to remain confidential for commercial reasons. Nonetheless, all data necessary for the reader to understand the degree of success achieved is present. Finally, due to

some unexpected results in the dynamic methods, the campaign was repeated one last time on a very simple specimen: a square hollow beam. The triple validation of the process allowed for a comprehensive comparison of results, which helped shed light on some of the hidden effects impacting the results, leading to a deeper understanding of the strengths and criticalities of the testing methodology.

The data obtained in all experimental phases was subjected to post-processing using the Python programming language. This process involved filtering and manipulating the raw experimental data to obtain reliable and accurate values to input into the solution equations.

## 1.4. Methodological Limitations

The development of the experimental methodology was subject to some important limitations. The most relevant of these were related to scheduling and costs. Due to the busy nature of the facility's testing schedules and the limited budget available, it proved necessary to make strategic decisions to make the procedure viable. For this reason. the more expensive or time-consuming methods were excluded, and the remaining techniques were modified and combined to create a time and cost-effective testing procedure. These limitations are tightly linked with the initial requirements of low cost and testing times. As such, addressing them naturally led to a high compliance with said requirements. The main challenge proved to be to simultaneously comply with the accuracy requirements.

Another limitation that was encountered was the limited availability of the required test stand, which was being used for regular testing on the rocket's fairing. Nonetheless, detailed schedule planning allowed all required test campaigns to be performed. Lastly, since some of the tests were to be performed on the primary structures of the OTV's flight model, precautions proved necessary to minimize the risk of damage. Virtual simulations of the full test campaign were run to make sure the object would not impact the ground or the test stand at any time. Additionally, all bolt holes used in the tests were protected with sealant to protect the OTV's surface coating.

## 1.5. Outline

The thesis is organized as follows: Chapter 2 describes the developed test campaign, starting with the requirements, then describing the selection process, and finally discussing the final testing methodology in detail. Chapter 3 presents the uncertainty analysis of each method, predicting the impact of error sources on the final uncertainties. Chapter 4 presents the outcome of a virtual simulation that was run to verify the complete test procedure before the physical testing campaign. Chapter 5 presents the results of the pre-validation campaign, in which one of the tests, the Compound Pendulum (CP) method, returned unacceptable results. This leads to Chapter 6, where the most influent parameters in the CP test are identified, and an optimization study is performed to reduce the uncertainties to acceptable levels and minimize test times. Chapter 7 presents the results of the validation campaign, performed on the OTV, as well as the ensuing campaign on a hollow beam. Finally, Chapter 8 provides recommendations for future work and draws the conclusions of the present one.

# 2

# Design of Experiments

This chapter presents the developed testing methodology. After a quick overview of the current state of the art, the process that led to the methodology definition is outlined. Then, the steps and material required for all tests involved are described in detail. The methodology aims to minimize time waste. The sequence in which the measurements are conducted plays a primary role in achieving this objective. For this reason, the methods will be presented in the same order in which they must be executed.

## 2.1. Requirements

As discussed in Chapter 1, the accuracy with which the mass, CoG, and MoI are known impacts the accuracy of the vehicle's maneuvers. For this reason, the requirements for the desired tests were discussed primarily with the Guidance, Navigation, and Control (GNC) team at RFA. This led to the definition of a set of functional (identified by the letter F), performance (P), environmental (E), schedule (S), and cost (C) requirements, listed in Table 2.1. Functional requirements F1-F4 describe the expected outcome of the tests, while performance requirements P1-P7 specify the desired quality of said outcome. These have been formulated in accordance with the company's specific needs. In particular, the uncertainty constraint of 10% on all results is based on the specifications of the control software, which is being developed by the RFA GNC experts to be robust to a 10% error on each inertia parameter. The requirements mention uncertainty rather than, for example, accordance with the CAD model because of the reason already introduced in Chapter 1, which is that the tests are needed precisely to obtain more reliable values than the ones predicted by the CAD software. The list proceeds with the environmental requirements E1 and E2, which are a practical description of the environmental conditions that the test needs to adapt to. Schedule requirement S1 reflects the need for a short testing campaign, taking a team of two a total of less than three days, while S2 is based on the company's schedule, which involved the OTV being shipped between the Portuguese and German sites. Lastly, the cost requirements deal with budget constraints.

## 2.2. State of the Art Overview

The papers by Schedlinski and Link [6] and Genta and Delprete [7] give a comprehensive overview of the current methods for the estimation of inertia parameters. The methods can be divided into static and dynamic methods. Static methods can only be used for the measurement of the mass and CoG. The MoI is a dynamic property of a body, depending on its mass distribution around the rotation axis, and can therefore only be determined through dynamic methods.

During the literature study phase, some methods emerged as the most promising based on their reported costs, testing times and accuracy. These are outlined and compared here.

**Table 2.1:** List of requirements for the inertia testing campaign on the OTV

| | | |
|---|---|---|
| Functional | F1 | The procedure shall provide sufficient data to determine the mass of the vehicle. |
| | F2 | The procedure shall provide sufficient data to determine the CoG coordinates of the vehicle. |
| | F3 | The procedure shall provide sufficient data to determine the MoI of the vehicle about its specified roll, pitch, and yaw axes. |
| | F4 | All results shall include justified uncertainty values. |
| | F5 | The development process shall generate scientific value. |
| Performance | P1 | The total uncertainty on the mass measurement shall be below 10% of the measured value. |
| | P2 | The total uncertainty on the determination of the $x$ coordinate of the CoG coordinate shall be below 10% of the vehicle's maximum dimension in $x$ direction. |
| | P3 | The total uncertainty on the determination of the $y$ coordinate of the CoG coordinate shall be below 10% of the vehicle's maximum dimension in $y$ direction. |
| | P4 | The total uncertainty on the determination of the $z$ coordinate of the CoG coordinate shall be below 10% of the vehicle's maximum dimension in $z$ direction. |
| | P5 | The total uncertainty on the measurement of the roll MoI shall be below 10% of the measured value. |
| | P6 | The total uncertainty on the measurement of the pitch MoI shall be below 10% of the measured value. |
| | P7 | The total uncertainty on the measurement of the yaw MoI shall be below 10% of the measured value. |
| Environmental | E1 | The test setup shall fit the RFA Portugal test facility. |
| | E2 | The test setup should fit the RFA Germany test facility. |
| Schedule | S1 | The full test campaign should not require more than 48 man-hours. |
| | S2 | All OTV tests shall be performed within the availability time window of the OTV structures at the RFA Portugal facility. |
| Cost | C1 | The cost for the company of newly bought hardware shall not exceed €5000. |
| | C2 | The cost for the company of newly bought hardware should not exceed €1000. |

### 2.2.1. Static Methods

Schedlinski and Link [6] identify three main static methods for inertia testing: the multi-point weighing, suspension, and balancing methods.

#### Multi-Point Weighing Method

In the multi-point weighing (MPW) method, the specimen is positioned onto a minimum of three load cells supporting its full weight ([8], [9]). These measure the interface forces at their respective locations. Assuming the load cells are vertically oriented, the total weight $W_{tot}$ is computed as the sum of the measured forces. Dividing this by the gravitational acceleration at the testing location, the mass of the body can be calculated.

The CoG coordinates $x_G$ and $y_G$ are computed through a weighted average of the coordinates of the load cells $x_{B_i}$ and $y_{B_i}$ over the interface forces $W_i$

$$\begin{bmatrix} x_G \\ y_G \end{bmatrix} = \frac{1}{W_{tot}} \sum_i \begin{bmatrix} x_{B_i} \\ y_{B_i} \end{bmatrix} W_i \tag{2.1}$$

One such measurement only yields the horizontal coordinates of the CoG. Two tests are needed to fully

determine the CoG position. Between the two, the body needs to be rotated to a different orientation.

The hardware costs are driven by the load cells. Depending on the desired quality and certifications, these currently oscillate between less than €50 and about €1000 each[1]. This makes the method potentially viable for low-budget applications, with room for improvement in case of stringent requirements and a higher budget.

The method is very reliable, with multiple sources reporting uncertainties lower than 0.5mm for the CoG coordinates ([8], [10], [11]) and lower than 0.05% for the mass ([8], [11]).

#### Suspension Method

In the suspension method, the specimen is hung by a rope multiple times, at different points. For each suspension, the rope line identifies the axis on which the CoG lies. The intersection of two or more of these axes pinpoints the CoG ([6], [12]).

The required hardware is very inexpensive. Modenini [12] reports achieving uncertainties around 1mm.

#### Balancing Method

The balancing method is performed by placing the body on one side of a beam balanced on top of a knife edge. A counterweight on the other side is shifted in position until equilibrium is reached [6]. The distance $r_{CoG}$ of the CoG from the fulcrum can be computed through the equation of equilibrium for torques

$$r_{cw} \cdot W_{cw} = r_{CoG} \cdot W_{tot}. \tag{2.2}$$

Here, $r_{cw}$ is the counterweight position $W_{cw}$ is its weight, and $W_{tot}$ is the weight of the specimen.

Three measurements at different orientations are needed to fully determine the CoG position. The testing hardware required can easily be procured for a very low price. Uncertainties below 0.5mm are reported [6].

### 2.2.2. Dynamic Methods

Dynamic methods involve the excitation of rigid-body motions. For this reason, they are naturally more complex than the static methods. Some of them, like the measurement robot method involve very expensive equipment. Others, like the run-down method, subject the body to potentially dangerous accelerations [6].

Three methods were identified as sufficiently safe and cheap for the scope of this work: the torsional pendulum, multi-filar pendulum, and compound pendulum. All of these rely on measuring the frequency of oscillatory motion and return one MoI value with each measurement. Therefore, three measurements are required to determine the three principal moments of inertia.

#### Torsional Pendulum Method

In the torsional pendulum method, the object is placed on a rotary table equipped with a rotational spring or torsion bar of known torsional stiffness $k_t$. If excited, the system will oscillate at a certain frequency $f$. The MoI $I$ around the oscillation axis can then be calculated as [6]

$$I = \frac{k_t}{(2\pi f)^2}. \tag{2.3}$$

For bodies as big as the OTV considered in this study, the hardware cost is driven by the cost of the table. This is highly variable, but can often cost more than 1000 euros[2]. The uncertainty on the resulting MoI values are reported by several sources to be below 1% ([10], [13]–[15]).

An important factor to consider about this method is that, for some bodies, it might not be easy to achieve all three perpendicular orientations needed to obtain the three principal moments of inertia. For example, the geometry of the Redshift OTV makes it easy to mount the body with the roll axis vertical, but the pitch and yaw configurations would require custom jigs.

[1] Sources: `www.amazon.de`, `www.vetek.com` (accessed on 18/04/2023).
[2] Source: `www.alibaba.com` (accessed on 18/04/2023).

### Multi-Filar Pendulum Method

In the multi-filar pendulum method, the object is suspended by multiple ropes, usually from two to four. An oscillating rotational motion is excited and, similarly to the torsional pendulum, the MoI follows from the frequency of oscillation $f$ ([6], [7]).

$$I = \frac{ab}{h}\frac{mg}{(2\pi f)^2} \tag{2.4}$$

Here, $a$ and $b$ are the mounting radii of the ropes, while $h$ is the vertical distance between the suspension plane on the body and the connection points on the rig. These parameters are highlighted in Figure 2.1, representing the bifilar version of the test. Lastly, $m$ and $g$ are the mass of the object and the gravitational acceleration.

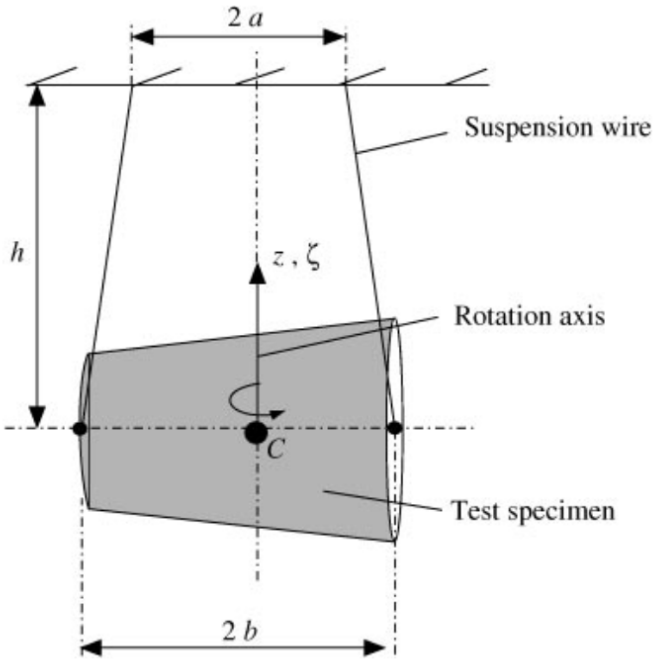


**Figure 2.1:** Principle of bifilar pendulum method [6]

Instead of the frequency, the period of oscillation $\tau$ can be used. Equation (2.4) then becomes

$$I = \frac{ab}{h}\frac{mg\tau^2}{4\pi^2} \tag{2.5}$$

Just like for the torsional pendulum, this method could be easily applicable for the roll MoI measurement of the OTV, but its application to the pitch and yaw MoI would be complicated. The necessary hardware consists of the ropes and a simple frame from which to suspend them. This can be built out of steel beams for less than 1000 euros[3]. Reported fractional uncertainties are around 1% ([16]–[18]).

### Compound Pendulum Method

In the compound pendulum (CP) method, the body is suspended by ropes and is made to oscillate around a horizontal axis. From the oscillation frequency, the MoI about the pendulum axis can be determined ([6], [19]).

$$I_P = \frac{mg\zeta}{(2\pi f)^2} \tag{2.6}$$

Here, $\zeta$ is the pendulum arm length, i.e., the vertical distance between the pendulum axis and the CoG of the body. In practice, this value can only be calculated if the vertical coordinate of the CoG is known.

[3] Source: `https://www.steelbeamsdirect.com/product/universal-beams` (accessed on 18/04/2023).

Therefore, if the CoG position is determined experimentally, this needs to be done prior to the CP test, and the errors in the vertical CoG coordinate will propagate to the MoI result.

The Huygens–Steiner theorem is then used to obtain the MoI about the axis parallel to the pendulum axis and going through the CoG of the body [20].

$$I = I_P - m\zeta^2 \tag{2.7}$$

Substituting Equation (2.6) into Equation (2.7) results in:

$$I = \frac{mg\zeta}{(2\pi f)^2} - m\zeta^2 \tag{2.8}$$

Like for the multi-filar pendulum method, the period can be used instead of the frequency, resulting in

$$I = \frac{mg\zeta\tau^2}{4\pi^2} - m\zeta^2 \tag{2.9}$$

The hardware needs are similar to those of the multi-filar pendulum. Very few sources were found discussing the uncertainties achievable with this method, and none apply it exactly as described above. In particular, Gabl et al. [20] achieved uncertainties of approximately 1% with a more expensive test stand involving a rigid swinging structure featuring a high accuracy inertial inclinometer. Blanes et al. [18] applied the CP principle to a small test stand to test padel rackets, achieving a standard deviation in the results of less than 0.4%. The body in this case is not suspended by ropes, but clamped at the height of the desired oscillation axis by a plastic jig that swings on bearings.

This method is easily applicable for the measurement of the OTV's pitch and yaw MoIs, since these measurements require the roll axis to be vertical. Applying it to the roll MoI would in general require custom jigs.

### 2.2.3. Trade-off analysis

Tables 2.2 and 2.3 give a schematic overview of the discussed methods. For each method, the tables list the cost, the required number of measurements, and uncertainty reported in relevant sources. This enables a trade-off, as the cost and uncertainty measurements represent respectively the cost and performance requirements, while the number of tests provides a qualitative idea of the involved testing times. In particular, the tables show that static testing is quite affordable, while the dynamic procedures are significantly more expensive. Here, exact cost values cannot be given, as the expenses depend on multiple variables such as the geometry and weight of the body, and the requirements on accuracy and time. Furthermore, the costs only refer to the hardware requirements of the methods. Manpower costs can be inferred by the number of measurements, since this impacts the testing times.

As shown in Table 2.2, the MPW test is marginally more expensive than the other two static methods, but compensates with very high accuracy. A further advantage is that this method allows the mass and CoG position to be determined at the same time, eliminating the need for an additional step to weigh the body. The suspension method presents a good trade-off of cost, uncertainty, and testing times. The balancing method, while presenting very low costs and uncertainties, presents higher testing times due to the need to reposition the body twice.

**Table 2.2:** Overview of static methods for CoG determination

| | Cost | Required number of tests | Reported Uncertainty |
|---|---|---|---|
| Multi-Point Weighing | Low | 2 | $< 0.5mm$ |
| Suspension | Very low | 2 | $\sim 1mm$ |
| Balancing | Very low | 3 | $< 0.5mm$ |

Among the dynamic methods presented in Table 2.3, the torsional pendulum presents very small uncertainties, but its cost is higher than that of the alternatives. The multi-filar pendulum and CP methods can achieve similar levels of accuracy with much lower expenses. This makes them more suited to the ends of this study.

**Table 2.3:** Overview of dynamic methods for MoI determination

| | Cost | Required number of tests | Reported Uncertainty |
|---|---|---|---|
| Torsional Pendulum | High | 3 | $< 1\%$ |
| Multi-Filar Pendulum | Medium | 3 | $\sim 1\%$ |
| Compound Pendulum | Medium | 3 | $\sim 1\%$ |

The comparison in Table 2.2 shows how, for mass and CoG estimation, the MPW and suspension methods are preferable to the balancing method due to the lower number of steps required. Both feature sufficient accuracy and low cost, and the mass can be directly obtained as a byproduct of the MPW test, without having to include a weighing step into the procedure. For these reasons, they are good candidates for an optimized methodology. Analogously, the multi-filar pendulum and CP methods were identified as the best options for MoI measurement, due to their sufficiently low uncertainties and the higher hardware cost of the torsional pendulum method. In order to define a simple, cost-effective, and time-efficient testing methodology, these preselected methods were analyzed in search of commonalities that could be exploited to reduce the total testing time and the overall hardware and manpower cost of the procedure.

Starting with the dynamic tests, evaluating all MoI values through either the multi-filar pendulum or CP method would require the body to be repositioned three times. I.e., after each measurement, the body would need to be rotated to a new orientation. Additionally, as discussed above, some orientations would prove challenging to achieve, namely the pitch and yaw configurations for the multi-filar pendulum, and the roll configuration for the CP. However, the shortcomings of each of these two methods can be compensated by the other. The roll MoI can be measured on a multi-filar pendulum, while yaw and pitch MoI values can be measured on a CP. This also reduces the time wasted on object repositioning, since the body is always kept vertical and only the ropes attachment points are shifted.

Regarding the multi-filar pendulum, a bifilar configuration (Bifilar Pendulum, BFP) fits the purpose of this study better than a trifilar or quadrifilar one. Two ropes can be mounted on a square rig, while a trifilar pendulum requires a circular rig for the three ropes to be equally spaced. The quadrifilar pendulum also presents this advantage, but the motion of a pendulum with more than three ropes can become irregular due to small transversal oscillations. Bifilar and trifilar pendulums do not present this risk [7]. A possible disadvantage of the BFP is that, if the CoG is not in-plane with the supporting ropes, the body will tilt and the pendulum oscillation will not happen about the exact intended axis. However, this effect was disregarded in this study since all tested bodies present a high degree of symmetry.

The chosen combination of methods for the MoI measurements requires a test rig from which the specimen is hung by multiple ropes. Out of the static tests considered, this setup only fits the suspension method. However, a suspended version of the MPW method was developed to measure the horizontal components of the CoG. This technique works analogously to the traditional MPW method, but is performed with the body suspended by three or more ropes equipped with tension load cells. This specific version appears to be novel, as no reference to it could be found in literature. This method was selected for the determination of the horizontal CoG coordinates due to its higher expected accuracy and simplicity compared to the suspension method.

To find the vertical CoG coordinate, another test is required. However, a second implementation of the MPW method would prove challenging, since it would require the body to be oriented differently, and the available mounting holes on the Redshift OTV are all in the same plane. The most practical solution has been identified as a modified suspension method. Instead of only one rope, two are supporting the body. The method has been therefore labeled *Bifilar Suspension* (BS). This method works similarly to the traditional method, except that it identifies the CoG plane, rather than the CoG axis. This plane, combined with the MPW results, is all that is needed to obtain the missing CoG coordinate. The bifilar variant is more robust than the traditional one, since two supports make the body more stable, and one angle measurement introduces less uncertainties than two. Additionally, the higher stability increases the safety of the test item. Both static methods in their selected variant are described more in detail in Section 2.3.

Based on the selected methods, five different tests are needed to measure all desired inertia parameters:

1. Suspended multi-point weighing (MPW)
2. Bifilar suspension (BS)
3. Bifilar pendulum (BFP)
4. Compound pendulum (CP) for pitch MoI
5. Compound pendulum for yaw MoI

These are executed in the order in which they are listed. The order has been devised to minimize the time needed for setup reconfiguration after each test. The transition from the MPW to the BS method only requires disconnecting one rope. Then, the two remaining ropes need to be repositioned to switch to the BFP configuration. Adding two more ropes connected appropriately brings the body to the CP configuration for pitch MoI measurement. Lastly, the ropes connection points are shifted on the body by $90°$ to achieve the yaw CP configuration.

## 2.3. Mass and CoG Determination

Two steps need to be performed to obtain all CoG coordinates: a MPW and a BS test. Both measurements also return the total mass of the body as a byproduct. In the first step, the body is suspended in a vertical orientation by three ropes. In the second one, one rope is detached to achieve a tilted orientation.

A custom coordinate system is introduced that simplifies the calculations. This is centered on one of the attachment points, with the $x$ axis pointing towards the following one in clockwise direction, the $z$ axis pointing downwards, and the $y$ axis completing the system, as shown in Figure 2.2.

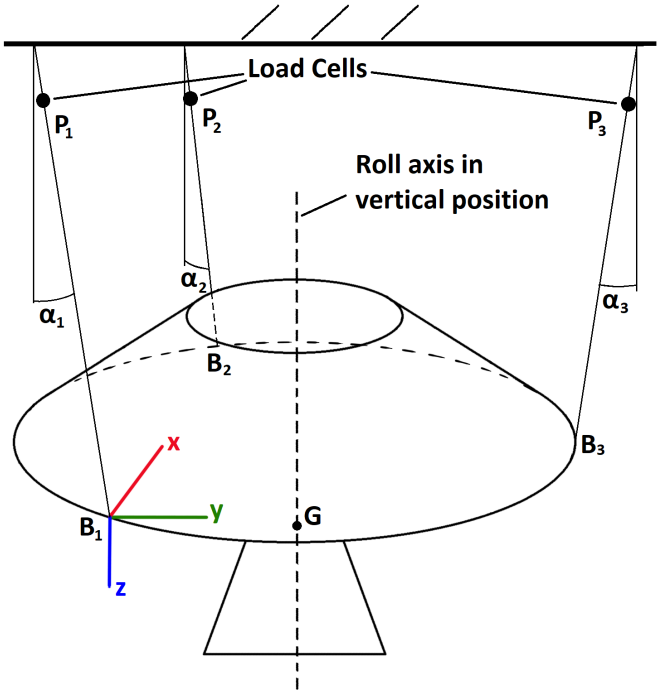


**Figure 2.2:** Schematic representation of the suspended multi-point weighing method

### 2.3.1. Suspended Multi-Point Weighing

The first phase consists in suspending the tested body using three ropes. The XY plane of the custom coordinate system is the measurement plane, and needs to be horizontal for the method to be equivalent to the traditional MPW method. As a consequence, the roll axis of the body is vertical.

As stated in Section 2.2.3, this variation of the method presents the benefit of requiring the same test setup as the other tests in the developed campaign. However, it also presents another advantage. The geometry of the Redshift OTV does not allow it to be supported by three or more load cells placed at the bottom, since it does not feature a flat surface there. Therefore, a custom test rig would be required featuring a hole where the body can be inserted in order for it to lie on the outer ring, which is the part designed to support the weight. The suspended version bypasses this issue. If the body has accessible holes, its geometry is only marginally important. This considerably widens the range of applicability of the method.

To suspend the body in the desired configuration, steel wire rope is used. This is connected to a turnbuckle on one end and an eye bolt on the other. The eye bolt is bolted to the specimen. The turnbuckles are used to adjust the length of each rope until the tilt of the body is below $0.5°$ in all directions. This is measured with an inclinometer.

The load cells used for the MPW and BS tests are S-type cells with M12 holes on both sides. The top eye bolt is connected to an eye bolt on the rig through a carabiner. The rope is connected to the cell by hooking the turnbuckle to a shackle on the bottom eye bolt of the cell. The full rope assembly is depicted in Figure 2.3. Three of these are used for the chosen configuration.

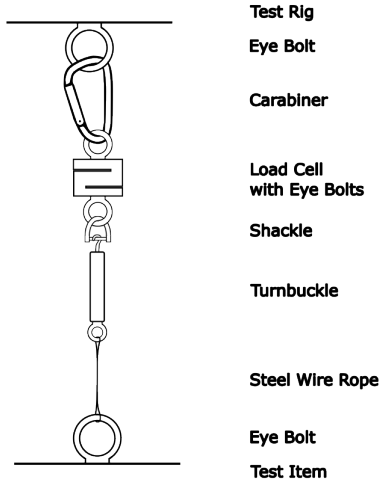


**Figure 2.3:** Rope assembly for MPW and BS

As shown in Figure 2.2, the ropes holding the body are not, in general, vertical. In this case, an inclinometer must be used to measure the inclination $\alpha_i$ of each rope with respect to the direction of gravity. Therefore, for each rope $i$, the vertical component of the supported load is calculated as

$$W_i = P_i \cdot \cos(\alpha_i) \tag{2.10}$$

where $i = 1, 2, 3$ for a trifilar configuration, and $P_i$ is the rope tension measured by the load cell. To obtain accurate $P_i$ measurements, the load cell acquisition time should be of at least 4 minutes to allow the inevitable swinging motion to be dampened.

The sum of the vertical components returns the total weight of the body.

$$W_{tot} = \sum_i W_i \tag{2.11}$$

The mass can easily be calculated by dividing $W_{tot}$ by the gravitational acceleration at the testing location.

$$m = \frac{W_{tot}}{g} \tag{2.12}$$

Substituting Equation (2.10) into Equation (2.12) results in

$$m = \frac{\sum_i P_i \cos(\alpha_i)}{g} \tag{2.13}$$

Equation (2.1) can then be rewritten as

$$\begin{bmatrix} x_G \\ y_G \end{bmatrix} = \frac{1}{W_{tot}} \sum_i \begin{bmatrix} x_{B_i} \\ y_{B_i} \end{bmatrix} P_i \cos(\alpha_i) \tag{2.14}$$

This equation returns the horizontal components of the CoG, given the horizontal components of the load cells, the orientations of the ropes, and the measured loads. The positions of the suspension points $(x_{B_i}, y_{B_i})$ can be measured directly on the CAD model. This is justified by the assumption that the uncertainty introduced by measuring the coordinates by hand would be comparable or larger than the manufacturing imperfections.

### 2.3.2. Bifilar Suspension

For the second measurement, the roll axis of the body is brought to a tilted orientation by disconnecting one of the ropes, as shown in Figure 2.4, while the remaining two are left untouched. The object will naturally settle with its CoG directly below the line connecting the two remaining supports, i.e., the $x$ axis.

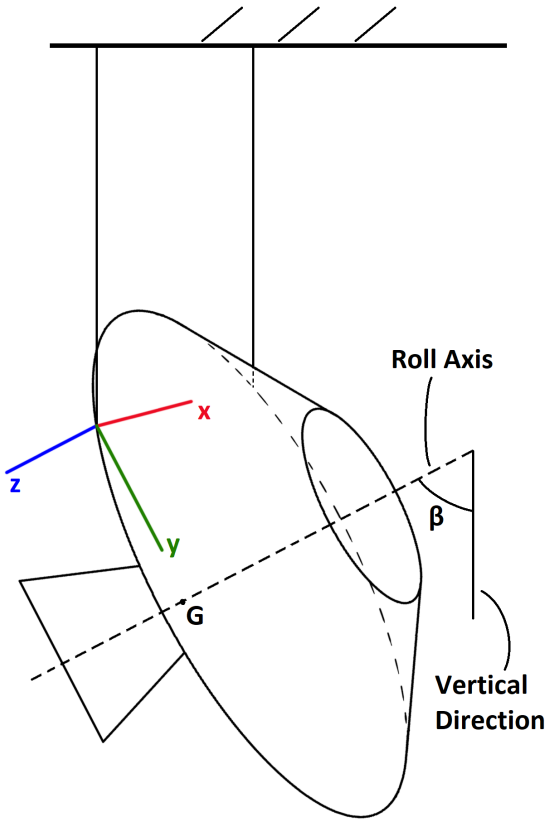


**Figure 2.4:** Schematic representation of the BS method

Figure 2.5 illustrates the two reference frames involved. The fixed, horizontal frame (superscript h), and the tilted one (superscript t). $G^{(t)}$ is the CoG position in the tilted configuration. $G'_h = (x_G, y_G, 0)$

represents the perpendicular projection of the CoG onto the body's horizontal plane, obtained as the result of the MPW test. The angle $\beta$ is the achieved tilt. This parameter is measured with an inclinometer and combined with the MPW results to calculate the CoG height.

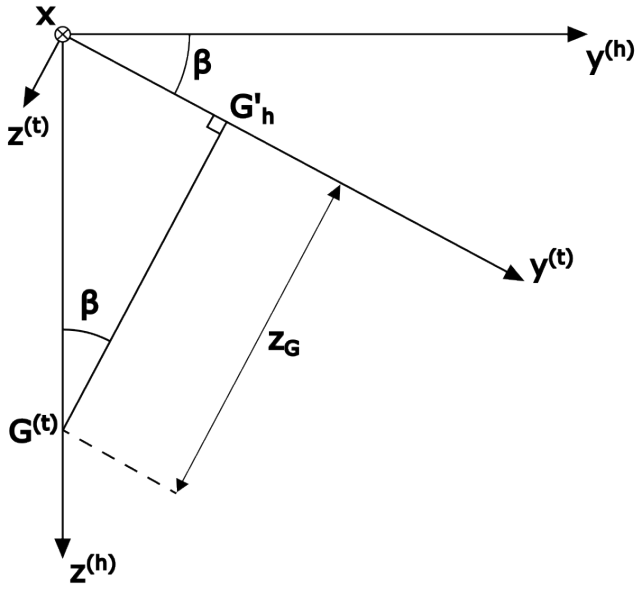


**Figure 2.5:** The $z$ coordinate of the CoG is determined by the tilt angle $\beta$ and the projection of the CoG onto the $y$ axis of the tilted frame

The equation for the vertical CoG coordinate $z_G$ is easily found. Assuming the rotation between the two measurements happens around the $x$ axis as in Figure 2.5, the CoG height can be calculated as:

$$z_G = \frac{y_G}{\tan(\beta)} \tag{2.15}$$

During this step it is also possible to measure the tension on the two remaining ropes, and again apply the formulas for MPW, to obtain additional estimates for $x_G$ and the mass. Since only two ropes are present, $y_G$ cannot be obtained here. The mass is calculated through Equation (2.13), while the equation for $x_G$ is the first line of Equation (2.14), applied to two ropes.

$$x_G = \frac{1}{W_{tot}}(x_{L_1} P_1 \cos(\alpha_1) + x_{L_2} P_2 \cos(\alpha_2)) \tag{2.16}$$

## 2.4. MoI Measurement

The MoI measurement strategy exploits the complementary relationship between the optimum application of the multi-filar pendulum (in its bifilar variant) and that of the CP. The former is used to measure the roll MoI, while the latter is used to measure the pitch and yaw MoIs.

### 2.4.1. Bifilar Pendulum

The BFP setup is schematically illustrated in Figure 2.1. For this configuration it is important that the roll axis is vertical. Otherwise, the measurement axis will not be the desired one. To make this possible, the CoG must approximately lie on the vertical plane going through the two attachment points. Otherwise, the body will tilt to achieve equilibrium. The scope of the methodology presented in this work is limited to roughly axisymmetric bodies, for which this condition is often verified, or easily achievable by adding small masses to achieve balance. Otherwise, in case of an unbalanced mass distribution in the tested body, the use of a trifilar or quadrifilar pendulum would remove this issue. Additionally, to achieve a

vertical roll axis, the two ropes should be carefully prepared so that they are of very similar length. A guideline backed by the observations in this study is that the body tilt once mounted should be smaller than $1°$ for negligible impacts on the results.

An accelerometer is placed on the measurement plane, with the measurement axis tangential to the rotational movement. If a triaxial accelerometer is available, it can be oriented with the $x$ axis tangential to the motion, measuring the tangential acceleration, the $y$ axis pointing towards the center of rotation, measuring the centripetal acceleration, and the $z$ axis pointing upwards, measuring the vertical motion of the body. This is shown in Figure 2.6. This way, all three axes are able to capture the oscillating

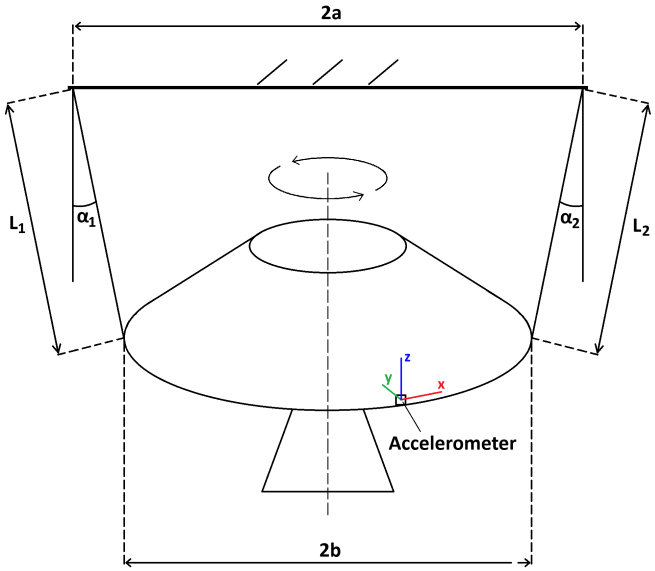


**Figure 2.6:** Schematic representation of the BFP method, showing the orientation of the accelerometer axes

motion, providing a higher number of estimates.

The signal will be a periodic wave, the frequency of which corresponds to the frequency of oscillation $f$. The frequency is obtained in post-processing through a Fast Fourier Transform (FFT) of the signal. The total acquisition time for the accelerometer is $200s$. This stems from the fact that the FFT algorithm discretizes the frequency domain into steps of

$$\Delta f = \frac{1}{t_{acq}} \tag{2.17}$$

Where $t_{acq}$ is the total acquisition time. Therefore, $t_{acq} = 200s$ will lead to a frequency resolution of $0.005Hz$ on each of the acquisitions.

Another important factor impacting the accuracy of the FFT is leakage. The FFT algorithm takes the input signal and repeats it a number of times to simulate the integration between $-\infty$ and $+\infty$ that characterizes the analytical Fourier transform. Therefore, if the sampled signal does not contain an integer number of periods, there will be a sharp transition between each subsequent repetition of the signal [4]. This is illustrated in Figure 2.7. A common way to reduce this effect is to multiply the signal by a window function equal to 0 at the extremes and to 1 in the middle. This way, the acquired signal begins and end with 0, and the transitions are smoothed out. This is the approach chosen in this work.

The roll MoI is obtained through Equation (2.4). Here, the mounting diameters $a$ and $b$ are taken directly from the CAD model. Like for the suspended MPW, the uncertainties introduced by the measurement would likely be larger than the ones due to the manufacturing imperfections. The mass $m$ comes from the results of the previous tests. Lastly, the vertical distance $h$ between the rope connection points on the test rig and on the body can either be directly measured with a tape measure or

[4] Source: `https://community.sw.siemens.com/s/article/windows-and-spectral-leakage` (accessed on 23/08/2023).

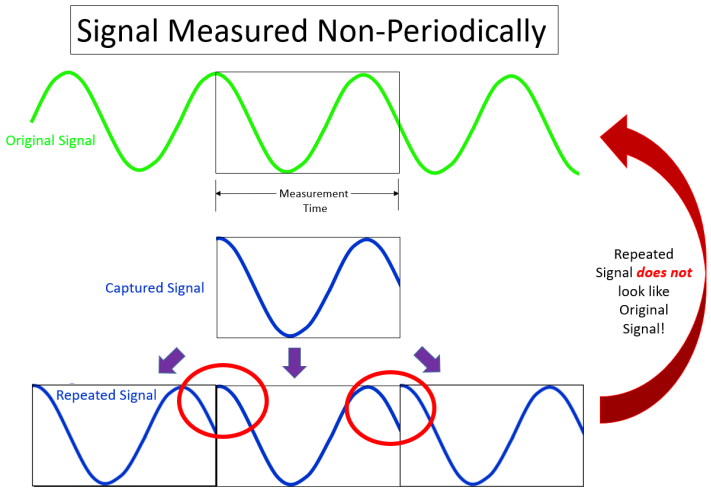


**Figure 2.7:** Effect of performing a FFT on a signal that does not contain an integer number of periods. Source: `https://community.sw.siemens.com/s/article/windows-and-spectral-leakage` (accessed on 23/08/2023).

calculated as the average of the ones calculated for each rope

$$h_i = L_i \cos(\alpha_i) \tag{2.18}$$

Where $L_i$ is the length of the i-th rope, measured between the centers of the two eye bolts, and $\alpha_i$ is its tilt. The former approach (direct measurement) introduces less sources of uncertainty and is preferable when the body's width is close to the test rig's, making it easy to measure the vertical distance between the two. For this reason, this was employed for the OTV tests. The latter is used when the body is much less wide than the rig, like in the case of the ESPA tests.

For the BFP test, the suspension system is very simple. Since the tests showed that turnbuckles and other stiff parts caused a shift in the measured frequency, the body is suspended solely by two steel ropes, each connecting one eye bolt on the body with one on the test rig. In the pre-validation testing phase on the ESPA, the rope assembly featured load cells to assess if they could accurately capture the motion, which would have made the accelerometer unnecessary, reducing the hardware cost. The turnbuckles were also part of the system, since they were meant to help with adjusting the body orientation and their effect on the results was still unknown. In later tests, both of these parts were removed.

### 2.4.2. Compound Pendulum

To determine the pitch and yaw MoI, the CP method is applied twice. Between the two measurements, the body is rotated $90°$. Figure 2.8 illustrates the two configurations.

Like for the BFP method (see Section 2.4.1), the oscillating motion of the CP is acquired 5 consecutive times with an accelerometer. In this case, the sensor is oriented in the direction of the swinging movement. The frequency of the signal will correspond to the frequency of oscillation $f$. As in the BFP, the acquisition length is $200s$ and the signal is windowed to reduce leakage.

The other parameters required to solve solution Equation (2.8) are the mass $m$, which directly results from the suspended MPW test, the gravitational acceleration $g$, which depends on the testing location, and the pendulum arm length $\zeta$, calculated as

$$\zeta = h + z_G \tag{2.19}$$

Here, $h$ is calculated analogously to how described in Section 2.4.1 for the BFP, while $z_G$ is the vertical coordinate of the CoG obtained through the static tests. This is added, rather than subtracted, because the $z$ axis of the body is oriented downwards.

The rope assembly used for this test is similar to the one for the BFP, but with two ropes connected to the same point on the structure, forming an inverted V shape. Two of these assemblies are used

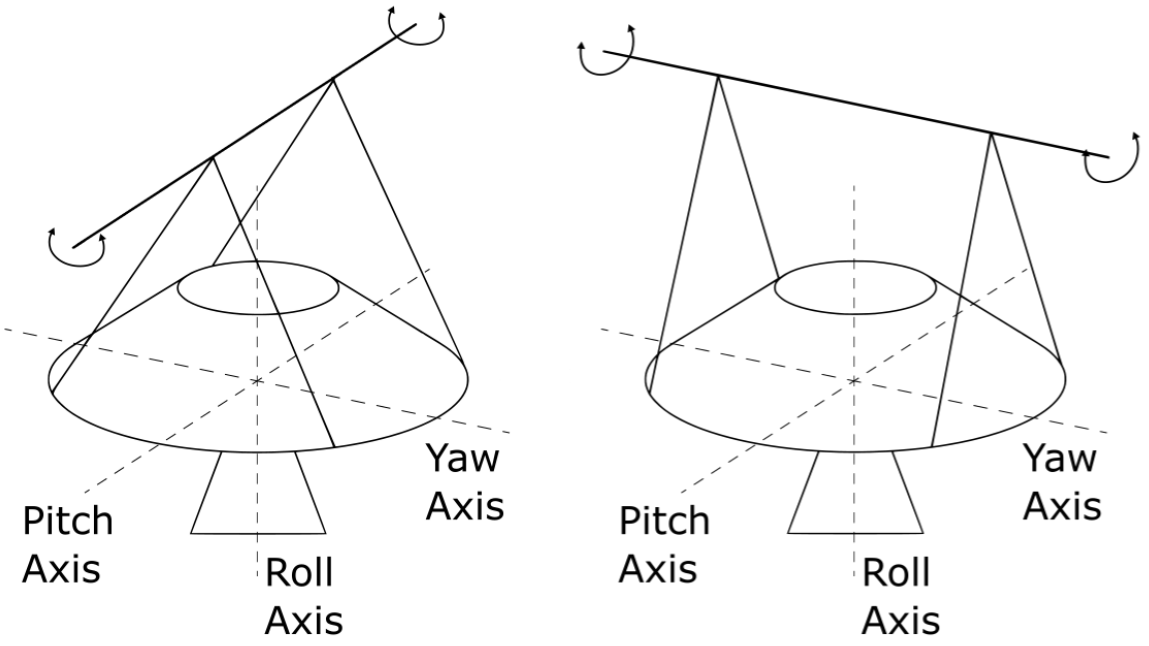


**(a)** Pitch configuration

**(b)** Yaw configuration

**Figure 2.8:** The two CP configurations

for the test, forming a setup resembling a swing. Here, too, the turnbuckles are absent. Therefore, the ropes must be prepared with precision. However, in this study it was found that four ropes can be prepared with deviations in length of less than 1 mm with relative ease.

## 2.5. Test Setup

The test setup is composed of a test rig from which the body is hung in several ways using steel wire rope. The test rig used for all tests in this thesis, shown in Figure 2.9, is a very stiff structure made of modified HEB beams of $160mm$ width. This was designed to support the rocket's fairing during the static tests, which involve loads several orders of magnitude higher than the ones associated with the tests described here. For this reason, the rig's flexibility is neglected in this study.

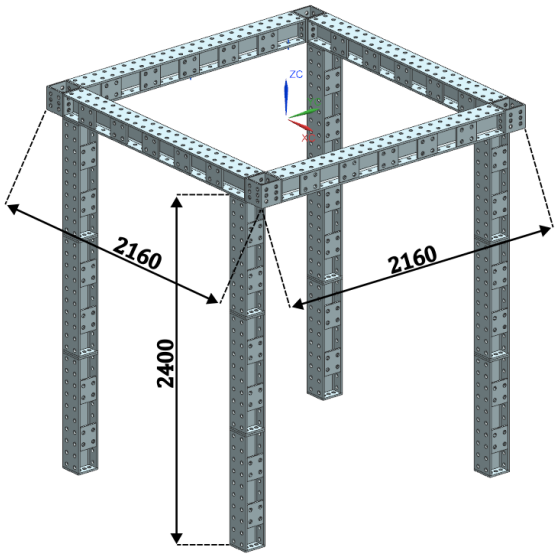


**Figure 2.9:** CAD model of test rig. Dimensions are in mm.

Despite not being explicitly stated in the requirements, it is of interest to the company, and even more to this thesis, that the developed testing methodology be easily adaptable to other assemblies of similar geometry to the OTV. For this reason the test setup was designed to be modular and mostly composed of off-the-shelf components. No custom jigs were used, which also contributed to keep the costs down. The test rig described above is indeed made of custom parts, but can be substituted by any frame built out of sufficiently stiff beams. The ropes support the body through holes that are part of the body geometry, eliminating the need for adapters. Therefore, the only requirement is that the body present such holes. This is likely to be true for many small rocket stages, which need the holes to interface with the other sections of the rocket. A list of all the equipment used in the tests can be found in Section A.1.

# 3

# Uncertainty Analysis

Measurement results are always expressed with a related uncertainty range. The best estimate $x_{best}$, usually the mean of the measured values, is followed by a $\pm$ symbol and the uncertainty margin $\delta x$:

$$x = x_{best} \pm \delta x. \tag{3.1}$$

This identifies a range, between $x_{best} - \delta x$ and $x_{best} + \delta x$, in which the value of the measurand can be said with confidence to lie [21]. This chapter deals with the estimation of uncertainties in the measurements. A theoretical background section introduces the most relevant concepts. Then, the theory is applied to the testing methodology that is the object of this thesis.

## 3.1. Theoretical Background

The theoretical basis for uncertainty analysis in this work is provided by three main sources. The two books *An Introduction to Error Analysis: The Study of Uncertainties in Physical Measurements* by Taylor [21] and *Experimentation, Validation, and Uncertainty Analysis for Engineers* by Coleman et al. [22] provide a detailed overview of all necessary steps in the uncertainty analysis process. Meanwhile, the ISO *Guide to the Expression of Uncertainty in Measurement (GUM)* [23] sets the standards for how uncertainties should be treated in measurements and experiments, in order to make results repeatable and comparable.

### 3.1.1. Errors and Uncertainties

The subtle distinction between the terms *error* and *uncertainty* often causes confusion. This work adopts the definitions of the *GUM* [23]. Here, the error is defined as the difference between the real value of the measurand and the measured value. Errors can be random or systematic, depending on whether they scatter the results evenly around the measurand value, or always on the same side (e.g., by excess). By definition, the error cannot be known, as this would require knowing the real value. Conversely, the uncertainty is a 'parameter, associated with the result of a measurement, that characterizes the dispersion of the values that could reasonably be attributed to the measurand'.

The uncertainty on a measurement is then an estimate of the effect of error sources on the result. Therefore, they can be linked to random or systematic effects. Random effects can be corrected by repeating the measurement several times and calculating an average. Conversely, systematic effects are not detectable in a statistic way, and must be assessed based on intuition and careful analysis of the test procedure [21].

The uncertainty on a single parameter can be assessed by statistical analysis of a series of observations (Type A evaluation) or by other means (Type B evaluation), such as relying on data from previous test campaigns featuring the same method. On the other hand, the uncertainty on a result obtained combining multiple uncertain values is calculated by propagating the uncertainties of the inputs into the output.

### 3.1.2. Propagation of Uncertainties

When the test result is calculated combining multiple measured quantities, the uncertainties on those quantities influence the result.

The general formula for error propagation for functions of several variables, is derived by Taylor [21] under the assumption of small uncertainties, and is in compliance with the *GUM* [23]. When the uncertainties are independent and random (i.e., each source is unaffected by the others), the various components can be combined in quadrature.

$$\delta q = \sqrt{\left(\left|\frac{\partial q}{\partial x}\right|\delta x\right)^2 + ... + \left(\left|\frac{\partial q}{\partial z}\right|\delta z\right)^2} \tag{3.2}$$

If, on the other hand, the uncertainties are either not independent or not random, the uncertainty must be calculated as an upper bound, resulting in a higher value.

$$\delta q \leq \left|\frac{\partial q}{\partial x}\right|\delta x + ... + \left|\frac{\partial q}{\partial y}\right|\delta y \tag{3.3}$$

### 3.1.3. Type A Evaluation of Standard Uncertainties

While systematic errors are hard to predict and detect, random errors can be spotlighted and compensated for by repeating the measurement a large number of times [21]. This generates a scatter of results. Uncertainty estimation becomes then a problem of statistics.

#### Normal Distribution

As demonstrated by Taylor [21], if the error sources are small and random in nature, the values from repeated measurements will follow a normal distribution. In this case, the best estimate after $N$ measurements can be taken as the mean value $\bar{x}$ of the measurements $x_i$.

$$x_{best} = \bar{x} = \frac{1}{N}\sum_{i=1}^{N} x_i \tag{3.4}$$

Then, the uncertainty in a single measurement can be estimated as the sample standard deviation.

$$\sigma_x = \sqrt{\frac{1}{N-1}\sum_{i=1}^{N}(x_i - \bar{x})^2} \tag{3.5}$$

Any single measured value will then lie within $\bar{x} \pm \sigma_x$ with 68% confidence.

Similarly, the uncertainty due to random errors $\delta x_{rand}$ on the best estimate $x_{best}$ corresponding to 68% confidence can be computed as the standard deviation of the mean $\sigma_{\bar{x}}$ [21].

$$\delta x_{rand} = \sigma_{\bar{x}} = \frac{\sigma_x}{\sqrt{N}} \tag{3.6}$$

In the *GUM* [23], this is referred to as the standard uncertainty. It follows from the above equation that the uncertainty in the best estimate will slowly decrease with increasing measurement repetitions.

#### T-Distribution

When the sample size $n$ is small, typically $n < 30$, the difference between the sample (experimental) standard deviation and the population (real) standard deviation becomes important. In this case, the Student distribution, or t-distribution, can be used for more conservative uncertainty estimates [23]. This is similar to the normal distribution as it is also symmetric with zero mean.

The t-distribution is characterized by its *degrees of freedom* $\nu$. In particular, if the $N$ observations conducted to estimate a single quantity are independent:

$$\nu = N - 1 \tag{3.7}$$

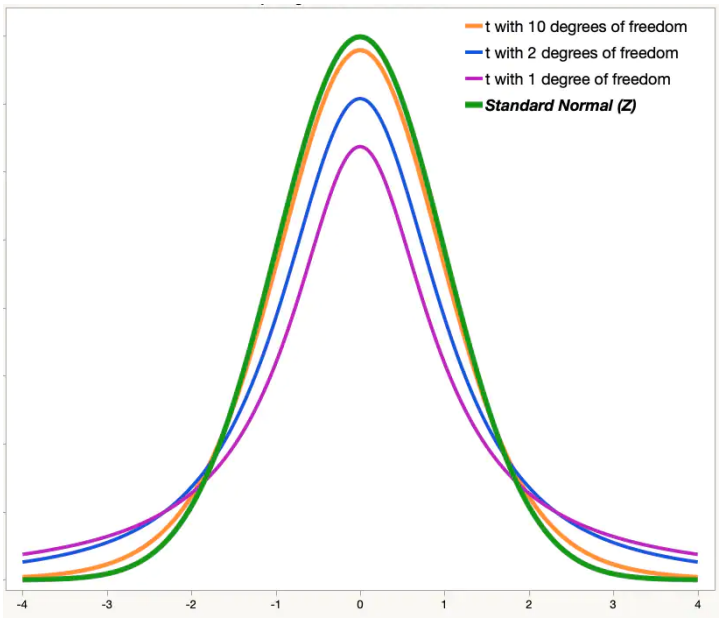


**Figure 3.1:** Comparison between three t-distributions and a normal (Z) distribution. Source: `https://www.jmp.com/en_us/statistics-knowledge-portal/t-test/t-distribution.html` (accessed on 18/04/2023).

An interesting property of the t-distribution is that, as $\nu$ approaches infinity, the t-distribution approaches a normal distribution [23]. This is shown in Figure 3.1.

The statistical uncertainty of a series of measurements that follows a t-distribution is calculated as

$$\delta x = t_p(\nu) \cdot \sigma_{\bar{x}}. \tag{3.8}$$

Where $t_p$ is the t-factor. Given the desired confidence level and the value of $\nu$, $t_p$ can be obtained for a wide variety of cases from the table in Appendix B. Since $t_p > 1$ for any finite value of $\nu$, the uncertainty values for the t-distribution will always be more conservative than for the normal distribution.

### Propagation of Statistical Uncertainty and Confidence Levels

As introduced in Section 3.1.2, if a test result is calculated combining multiple parameters, its uncertainty is determined by propagating the uncertainties on the parameters. In particular, if the parameters are independent and their respective uncertainties have been determined statistically, the standard deviation of the result can be estimated by combining the standard deviations of the parameters through Equation (3.2) [22].

$$\sigma_r = \sqrt{\left(\left|\frac{\partial r}{\partial x}\right|\sigma_x\right)^2 + \ldots + \left(\left|\frac{\partial r}{\partial z}\right|\sigma_z\right)^2} \tag{3.9}$$

Conversely, if the parameters are interdependent, Equation (3.3) must be used.

Once the standard uncertainty $\sigma_r$ is determined, the uncertainty associated with the desired confidence level can be calculated through Equation (3.8). To determine the approximate degrees of freedom $\nu_r$ of the combined result and hence select the appropriate t-factor, the Welch–Satterthwaite formula [22] can be used:

$$\nu_r = \frac{[\sum_{i=1}^{J}(\theta_i^2 s_i^2 + \theta_i^2 b_i^2)]^2}{\sum_{i=1}^{J}\left[\frac{(\theta_i s_i)^4}{\nu_{s_i}} + \frac{(\theta_i b_i)^4}{\nu_{b_i}}\right]} \tag{3.10}$$

Here, $\theta_i$ is a short notation for the partial derivative $\frac{\partial r}{\partial x_i}$ of the result r with respect to a variable $x_i$, while $s_i$ and $b_i$ are estimates of the standard deviation of, respectively, the random and systematic error distribution on the same variable $x_i$.

Coleman and Steele [22] argue that the use of this formula is often not necessary. The presence of the fourth power in each term makes it so that, if one or more terms are dominant, the others can be

neglected. If there is one dominant term $x_i$, the degrees of freedom of the result are approximately the same as those of that term, $\nu_r \approx \nu_i$. If there is a number $M$ of dominant terms of the same magnitude and the same degrees of freedom $\nu_a$, the degrees of freedom of the results are calculated as

$$\nu_r = M\nu_a \tag{3.11}$$

### 3.1.4. Type B Evaluation of Standard Uncertainties

In some cases, the best estimate of a measured quantity is not obtained through statistical analysis of repeated observations. Then, the standard uncertainty must be estimated using scientific judgement, based on the available knowledge of the variability of the measurement. According to the *GUM* [23], common sources of such knowledge can be:

- Previous measurement data
- Experience with or general knowledge of the behavior and properties of relevant materials and instruments
- Manufacturer's specifications
- Data provided in calibration and other certificates
- Uncertainties assigned to reference data taken from handbooks

If the uncertainty is provided by the manufacturer or by another source as a multiple of a standard deviation, the standard uncertainty can be calculated by simply dividing the quoted value by the multiplier [23].

In some cases, it can be assumed that, for all practical purposes, a measurement will lie within $x_{min}$ and $x_{max}$ with probability equal to $1$. Then, the best estimate $x_{best}$ can be taken as the average of the two values, with associated variance [23]

$$\sigma^2_{x_{best}} = \frac{(x_{max} - x_{min})^2}{12} \tag{3.12}$$

The *GUM* [23] treats all standard uncertainties, be them from type A or type B evaluation, the same way. Therefore, when calculating the combined uncertainty, Equation (3.9) can be used, regardless of the types of the input uncertainties. In particular, this is relevant when combining uncertainties due to random and systematic sources.

### 3.1.5. Combining Multiple Measurements of the Same Quantity

It is good practice, in testing, to repeat the result acquisition multiple times, in order to compare all results and achieve a level of confidence higher than that of any of the single measurements. To combine these independent results, the method of inverse-variance weighting can be used. This involves a weighted average in which each result is assigned a weight inverse to their variance [21].

$$w_i = \frac{1}{\sigma_i^2} \tag{3.13}$$

As a result, more precise values will have a larger impact on the calculated best estimate. The best estimate is calculated from $N$ independent results as:

$$x_{best} = \frac{\sum_{i=1}^{N} w_i x_i}{\sum_{i=1}^{N} w_i} \tag{3.14}$$

The variance on this best estimate is calculated as:

$$\sigma^2_{x_{best}} = \frac{1}{\sum w_i} \tag{3.15}$$

This last result is obtained by deriving from Equation (3.14) the influence of each measurement $x_i$ on the weighted average $x_{best}$, and combining them in quadrature according to Equation (3.2).

## 3.2. Application to the Problem

This section applies the theoretical basis presented above to the problem at hand. The influence of all parameters explicitly appearing in the solution equations of the chosen methods is derived, along with the influence of other factors that, according to the assumptions made, could have a relevant impact.

### 3.2.1. Mass and CoG Determination

The mass and CoG of the body are calculated through the MPW and the BS methods. This section first derives the analytical expressions for the sensitivity of all results to the input parameters, and then assesses the potential influence of a tilted body orientation.

#### Sensitivity to Input Parameters

The influence of the parameters $P_i$ and $\alpha_i$ on Equation (2.13) for mass calculation is expressed by the following two equations:

$$\frac{\partial m}{\partial P_i} = \frac{\cos(\alpha_i)}{g_0} \tag{3.16}$$

$$\frac{\partial m}{\partial \alpha_i} = \frac{-P_i \sin(\alpha_i)}{g_0} \tag{3.17}$$

These can be assumed independent and random, and be combined in quadrature to obtain the combined uncertainty on the mass:

$$\delta m = \sqrt{\sum_{i=1}^{3} \left[ \left( \frac{\partial m}{\partial P_i} \delta P_i \right)^2 + \left( \frac{\partial m}{\partial \alpha_i} \delta \alpha_i \right)^2 \right]} \tag{3.18}$$

In the same way, the uncertainty on the CoG coordinates can be estimated by deriving the influence of the explicit parameters on Equations (2.14) and (2.15). From Equation (2.14), the influence of the explicit parameters $x_{B_i}$, $y_{B_i}$, $P_i$ and $\alpha_i$ on the measured horizontal coordinates $x_G$ and $y_G$ can be derived. The same expressions are valid if new estimates are calculated during the BS step.

$$\frac{\partial x_G}{\partial x_{B_i}} = \frac{W_i}{W_{tot}} \tag{3.19}$$

$$\frac{\partial x_G}{\partial y_{B_i}} = 0 \tag{3.20}$$

$$\frac{\partial x_G}{\partial P_i} = (x_{B_i} - x_G) \frac{\cos(\alpha_i)}{W_{tot}} \tag{3.21}$$

$$\frac{\partial x_G}{\partial \alpha_i} = (x_G - x_{B_i}) \frac{P_i \sin(\alpha_i)}{W_{tot}} \tag{3.22}$$

$$\frac{\partial y_G}{\partial x_{B_i}} = 0 \tag{3.23}$$

$$\frac{\partial y_G}{\partial y_{B_i}} = \frac{W_i}{W_{tot}} \tag{3.24}$$

$$\frac{\partial y_G}{\partial P_i} = (y_{B_i} - y_G) \frac{\cos(\alpha_i)}{W_{tot}} \tag{3.25}$$

$$\frac{\partial y_G}{\partial \alpha_i} = (y_G - y_{B_i}) \frac{P_i \sin(\alpha_i)}{W_{tot}} \tag{3.26}$$

All the above parameters are obtained independently, and for each of them the random errors are assumed to be predominant over the systematic ones, since all instruments will undergo calibration

before use. The uncertainty due to the explicit parameters can then be calculated according to Equation (3.2), considering that each load cell $i$ generates its own uncertainty.

$$\delta x_G = \sqrt{\sum_{i=1}^{3} \left[ \left( \frac{\partial x_G}{\partial x_{B_i}} \delta x_{B_i} \right)^2 + \left( \frac{\partial x_G}{\partial P_i} \delta P_i \right)^2 + \left( \frac{\partial x_G}{\partial \alpha_i} \delta \alpha_i \right)^2 \right]} \tag{3.27}$$

$$\delta y_G = \sqrt{\sum_{i=1}^{3} \left[ \left( \frac{\partial y_G}{\partial y_{B_i}} \delta y_{B_i} \right)^2 + \left( \frac{\partial y_G}{\partial P_i} \delta P_i \right)^2 + \left( \frac{\partial y_G}{\partial \alpha_i} \delta \alpha_i \right)^2 \right]} \tag{3.28}$$

Lastly, the explicit parameters involved in Equation (2.15) for the CoG height are $y_G$ and $\beta$. Their respective influence can be derived as:

$$\frac{\partial z_G}{\partial y_G} = \frac{1}{\tan(\beta)} \tag{3.29}$$

$$\frac{\partial z_G}{\partial \beta} = -\frac{y_G}{\sin^2(\beta)} \tag{3.30}$$

It is interesting to note from Equation (3.30) how the uncertainty due to the inclination grows very quickly as $\beta$ gets small. This reflects the high uncertainty generated by finding the intersection between two lines of similar inclination (Figure 3.2).

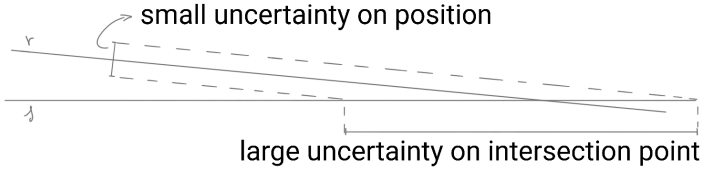


**Figure 3.2:** Uncertainty in the determination of the intersection between two lines of similar inclination

Combining the two components, the total uncertainty on the CoG height is determined

$$\delta z_G = \frac{\partial z_G}{\partial y_G} \delta y_G + \frac{\partial z_G}{\partial \beta} \delta \beta \tag{3.31}$$

Here, the terms are not added in quadrature since they are not independent. Substituting Equations (3.29) and (3.30) into Equation (3.31) results in

$$\delta z_G = \frac{1}{\tan(\beta)} \delta y_G - \frac{y_G}{\sin^2(\beta)} \delta \beta \tag{3.32}$$

Here, the signs can be kept as they are, instead of taking the absolute value of the components as in Equation (3.3). This is due to the fact that it is known that positive errors on $y_G$ will cause positive errors on $z_G$, while positive errors on $\beta$ will cause negative errors on $z_G$.

### Influence of Body Inclination on Suspended Multi-Point Weighing

The inclination of the body at the moment of testing will affect the results of the MPW measurement. As discussed in this paragraph, assuming the body's roll axis is perfectly vertical when it is not can generate large errors. Figure 3.3 shows a fixed, horizontal plane, and an inclined plane, representing the body's horizontal measurement plane. The fixed frame is identified by the superscript $(f)$. The two angles $\eta$ and $\xi$ are measured by placing the inclinometer in two perpendicular directions on the measured object. In this case, Equation (2.14) would return the coordinates of the vertical projection

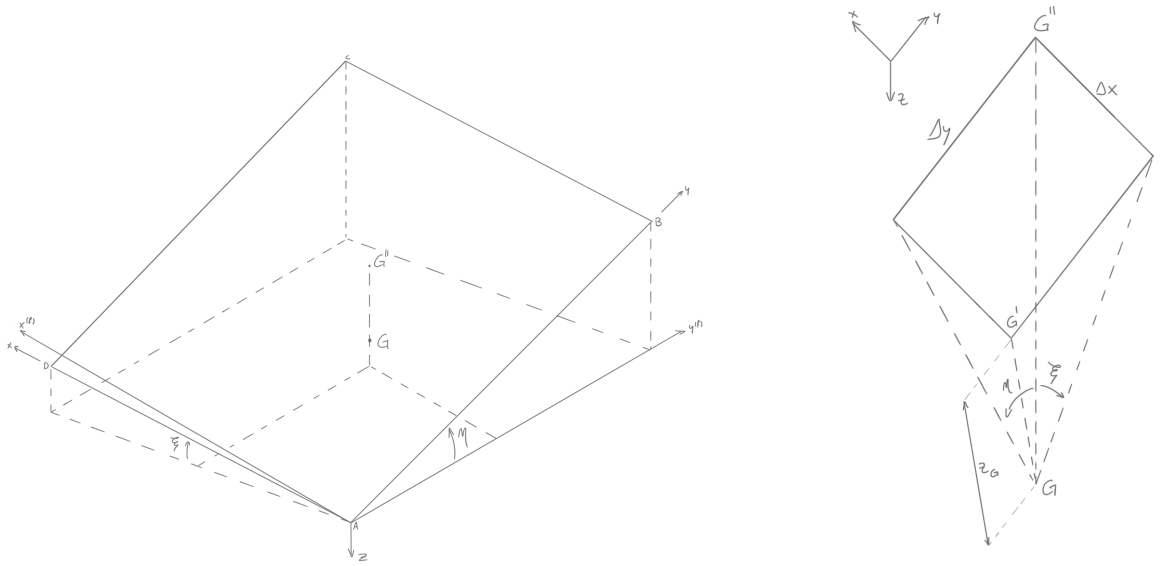


**(a)** Wide view **(b)** Detail view

**Figure 3.3:** Influence of body inclination in CoG determination through multi-point weighing

of the CoG $G''$, rather than the perpendicular projection $G'$. This generates a deviation $\Delta x_G$ along the $x$ direction of the vehicle, and $\Delta y_G$ along the $y$ direction of the vehicle.

$$\Delta x_G = z_G \cdot \tan(\xi) \tag{3.33}$$

$$\Delta y_G = z_G \cdot \tan(\eta) \tag{3.34}$$

The error is then dependent on the CoG height or, more precisely, on its distance $z_G$ from the measurement plane.

Instead of treating the tilt as a source of uncertainty, the solution equation can be rewritten to incorporate such deviation. Equation (2.14) then becomes

$$\begin{bmatrix} x_G \\ y_G \end{bmatrix} = \frac{1}{W_{tot}} \sum_i \begin{bmatrix} x_{B_i} \\ y_{B_i} \end{bmatrix} P_i \cos(\alpha_i) - z_G \begin{bmatrix} \tan(\xi) \\ \tan(\eta) \end{bmatrix} \tag{3.35}$$

The drawback of this approach is that, according to Equation (2.15), $z_G$ is only known after $x_G$ and $y_G$. An iterative process can be used to calculate all coordinates. $z_G$ is initially assumed equal to the value from the CAD, and then updated at each iteration with the result. The advantage is that the body inclination does not contribute to the overall uncertainty of the procedure, if not for the measurement uncertainty of the instrument, which is in most cases negligible.

In this work, the effect of the body inclination is neglected. The rope length is adjustable, so the tilt angles $\xi$ and $\eta$ can be reduced until the inclinometer shows values smaller than 0.5° in both directions. This will cause the deviations $\Delta x$ and $\Delta y$ to be smaller than $0.01 \cdot z_G$. Moreover, given the geometry of the Redshift OTV and the position of the chosen suspension points, $z_G$ is about one tenth of $x_G$. The errors would then be $\Delta x \approx \Delta y \approx 0.001 \cdot x_G$. For these reasons, these effects are expected to have a very small impact on the results. Future engineers should reflect on whether these assumptions are also valid for their system and, if not, use the information contained in this paragraph to compensate for the generated errors.

### 3.2.2. Bifilar Pendulum

The uncertainty on the BFP measurements is influenced by the uncertainty on the explicit parameters in Equation (2.4). However, other factors must be considered, such as the CoG misalignment with respect to the pendulum axis, as well as nonlinear effects due to large oscillations.

#### Sensitivity to Input Parameters

From Equation (2.4), the variables affecting the results can be identified as $m$, $\tau$, $h$, $a$, and $b$. The influence of each of these parameters can easily be derived from the equation. The procedure is shown below for the mass $m$.

$$\frac{\partial I}{\partial m} = \frac{ab}{h}\frac{g}{(2\pi f)^2} \tag{3.36}$$

Then, multiplying by the uncertainty on the mass $\delta m$ and dividing by $I$ to obtain the fractional uncertainty:

$$\frac{\frac{\partial I}{\partial m}\delta m}{I} = \frac{1}{m}\delta m \tag{3.37}$$

Analogously, the fractional uncertainty contributions of the other parameters can be derived.

$$\frac{\frac{\partial I}{\partial f}\delta f}{I} = -\frac{2}{f}\delta f \tag{3.38}$$

$$\frac{\frac{\partial I}{\partial h}\delta h}{I} = -\frac{1}{h}\delta h \tag{3.39}$$

$$\frac{\frac{\partial I}{\partial a}\delta a}{I} = \frac{1}{a}\delta a \tag{3.40}$$

$$\frac{\frac{\partial I}{\partial b}\delta b}{I} = \frac{1}{b}\delta b \tag{3.41}$$

If the period $\tau$ is measured instead of the frequency $f$, the following can be written instead of Equation (3.38):

$$\frac{\frac{\partial I}{\partial \tau}\delta \tau}{I} = \frac{2}{\tau}\delta \tau \tag{3.42}$$

The frequency resolution $\Delta f$ of the FFT mentioned in Section 2.4.1 need not be considered. The uncertainty $\delta f$ is determined through type A evaluation, and therefore already accounts for the effects of discretization errors.

#### CoG Misalignment

A potentially important error source that is not explicit in Equation (2.4) is the misalignment of the CoG with respect to the geometrical center of the pendulum. A misaligned CoG affects the way the pendulum oscillates [24]. Figure 3.4 shows how the system would behave with a CoG (and center of rotation) $G$ not coincident with the center $C$ of the pendulum. The angular displacement $\theta$ of the body will result in two different rope inclinations $\alpha_A$ and $\alpha_B$.

To estimate the impact on the results, the equation of motion (EOM) of the misaligned system needs to be derived. Given the geometry of the system, the following relations between the angles can be written.

$$\begin{cases} \alpha_A = \frac{R_A}{h}\theta \\ \alpha_B = \frac{R_B}{h}\theta \end{cases} \tag{3.43}$$

The weight $W$ supported by each rope can be calculated from the tension $P$ on each of the ropes.

$$\begin{cases} W_A = P_A \cos(\alpha_A) \\ W_B = P_B \cos(\alpha_B) \end{cases} \tag{3.44}$$

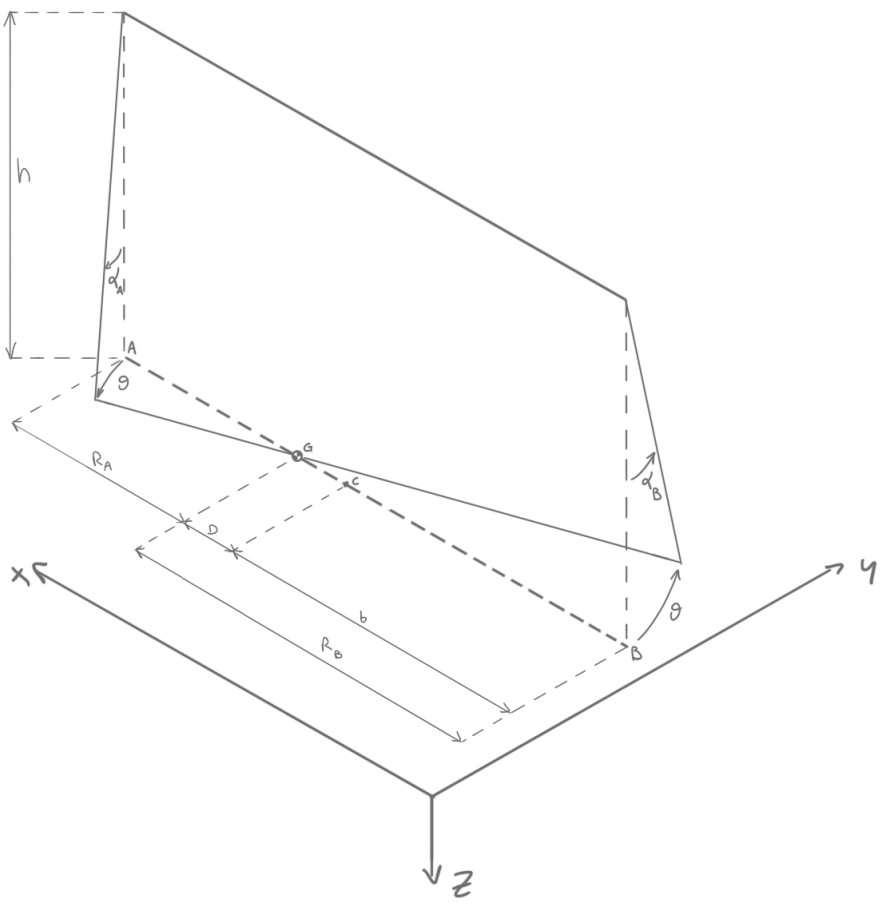


**Figure 3.4:** Scheme of bifilar oscillation with misaligned CoG

Introducing the dimensionless misalignment factor $\varphi_G = \frac{D}{b}$ and considering the equilibrium equation for torque about the CoG $R_A W_A = R_B W_B$ , Equations 3.44 can be rewritten as

$$\begin{cases} W_A = (1 + \varphi_G)\frac{W_{tot}}{2} \\ W_B = (1 - \varphi_G)\frac{W_{tot}}{2} \end{cases} \tag{3.45}$$

where $W_{tot} = W_A + W_B$.

The horizontal forces generating the restoring torque are

$$\begin{cases} F_A = W_A \tan(\alpha_A) \approx W_A \alpha_A \\ F_B = W_B \tan(\alpha_B) \approx W_B \alpha_B \end{cases} \tag{3.46}$$

Therefore, the torque on the body is

$$T_z = -F_A \cdot R_A - F_B \cdot R_B \tag{3.47}$$

Or, substituting equations 3.43, 3.44, and 3.46 into Equation (3.47):

$$T_z = -(1 - \varphi_G^2)\frac{b^2 W_{tot}}{h}\theta \tag{3.48}$$

Substituting into Newton's second law for rotation:

$$-(1 - \varphi_G^2)\frac{b^2 W_{tot}}{h}\theta = I\ddot{\theta} \tag{3.49}$$

Where $\ddot{\theta}$ is the angular acceleration of the body about the vertical axis going through the CoG.

Assuming simple harmonic motion, the solution can be written as a function of the angular frequency $\omega$.

$$(1-\varphi_G^2)\frac{b^2 W_{tot}}{h} - \omega^2 I = 0 \tag{3.50}$$

Substituting $\omega = \frac{2\pi}{\tau}$ and reorganizing results in

$$I = (1-\varphi_G^2)\frac{b^2 W_{tot}\tau^2}{4\pi^2 h} \tag{3.51}$$

The contribution to the uncertainty due to the misalignment error can now be calculated as for the other parameters.

$$\frac{\frac{\partial I}{\partial \varphi_G}\delta\varphi_G}{I} = -2\varphi_G \frac{b}{a}\delta\varphi_G \tag{3.52}$$

The combined uncertainty from all considered sources can be obtained through Equation (3.3).

$$\frac{\delta I}{I} \leq 2\varphi_G \frac{b}{a}\delta\varphi_G + \frac{1}{m}\delta m + \frac{2}{f}\delta f + \frac{1}{h}\delta h + \frac{1}{a}\delta a + \frac{1}{b}\delta b \tag{3.53}$$

These results are analogous to those reported by Du Bois et al. [24], despite the slightly different setup, bifilar rather than trifilar, and with unequal mounting radii $a \neq b$, rather than equal ones.

However, all contributions except the one related to CoG misalignment are independent of each other and can therefore be added in quadrature, for a more realistic, albeit less conservative estimate of the uncertainty.

$$\frac{\delta I}{I} = 2\varphi_G \frac{b}{a}\delta\varphi_G + \sqrt{\left(\frac{1}{m}\delta m\right)^2 + \left(\frac{2}{f}\delta f\right)^2 + \left(\frac{1}{h}\delta h\right)^2 + \left(\frac{1}{a}\delta a\right)^2 + \left(\frac{1}{b}\delta b\right)^2} \tag{3.54}$$

The misalignment effect is mostly relevant when the setup includes a suspended platform onto which the test item has to be placed. In this work, the ropes are attached directly to a roughly axisymmetric body, so the human error in centering the body on the pendulum's platform does not occur. Therefore, the only cause of CoG misalignment is the uneven mass distribution of the body making its CoG not lie on the roll axis.

An estimate of the impact of CoG misalignment on the final results can be calculated using data from the CAD model of the fully assembled OTV. The software predicts the CoG position at a distance of about $4mm$ from the roll axis. The holes used for the test are placed at a distance of around $2000mm$, therefore $b \approx 1000mm$. Then, the misalignment factor is $\varphi_G \approx \frac{4}{1000} = 0.004$. Assuming $\frac{b}{a} = 1$ (a conservative assumption, considering that in the designed test setup $b > a$), and $\delta\varphi_G = \varphi_G$, the fractional uncertainty due to this effect, calculated through Equation (3.52) is about $3.2{\cdot}10^{-5}$, or $0.0032\%$. For this reason, it can be safely neglected.

### Nonlinear Motion

Large oscillation amplitudes can introduce nonlinear effects into the motion of the tested body, reducing the accuracy of the results. This influence has been analyzed by Previati [25], and has been generally found to be most influent for bodies with a small radius of gyration or when the ratio $\frac{R}{L}$ between the mounting radius of the ropes and their length is large. In the case of the Redshift OTV, the radius of gyration about the roll axis is about $0.632m$, while for the ESPA it is $0.335m$. The diameter-to-length ratio is, in both cases, in the order of $\frac{R}{L} \approx 1$. Figure 3.5 illustrates the results of Previati [25] for 5 values of $\frac{R}{L}$ and 3 values of the radius of gyration $\rho$. At $\frac{R}{L} = 1$ and $\rho = 0.24m$ the error is below 1% at all amplitudes below 10°. For even higher radii of gyration, the effect is expected to be even smaller.

To confirm these results, the backbone of the system was derived, i.e., the amplitude dependent expression of the frequency, obtained through equivalent linearization of the non-linear EOM [26]. The non-linear EOM for a BFP is

$$I\ddot{\varphi} + \frac{ab}{h}mg\,\sin(\varphi) = 0 \tag{3.55}$$

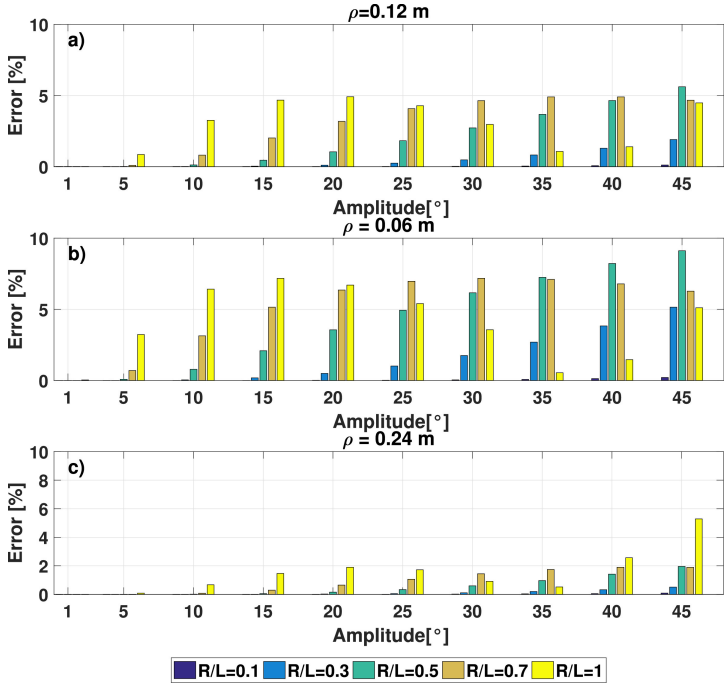


**Figure 3.5:** Estimated errors on oscillation period due to nonlinear motion as a function of oscillation amplitude, for different values of $\frac{R}{L}$ and radius of gyration $\rho$ [25]

By substituting $\sin(\varphi)$ with the first terms of its Taylor expansion at 0: $\sin(\varphi) \approx \varphi - \frac{\varphi^3}{3!} + \frac{\varphi^5}{5!}$, the equivalent linearization can be carried out, ultimately leading to the following backbone function:

$$f(A) = \frac{1}{2\pi}\sqrt{\frac{\frac{mgab}{h}(1 - \frac{A^2}{8} + \frac{A^4}{192})}{I}} \tag{3.56}$$

Figure 3.6a shows the plotted backbone for $h = 1349.34mm$, correspondent to a rope length of 1500mm, while Figure 3.6b shows the percentage error on the period of oscillation. This was calculated as the percentage difference between the period $T(A) = \frac{1}{f(A)}$ at $A = 0$ and at $A$. Given the chosen rope length and the geometry of the test rig, the $\frac{R}{L}$ ratio of the system is about 0.7. Given the radius of gyration of the ESPA $\rho = 0.335m$, the backbone predicts similar amplitude-dependent errors as the abovementioned study [25] up to an amplitude of $20°$, and diverges faster for larger amplitudes. Motion

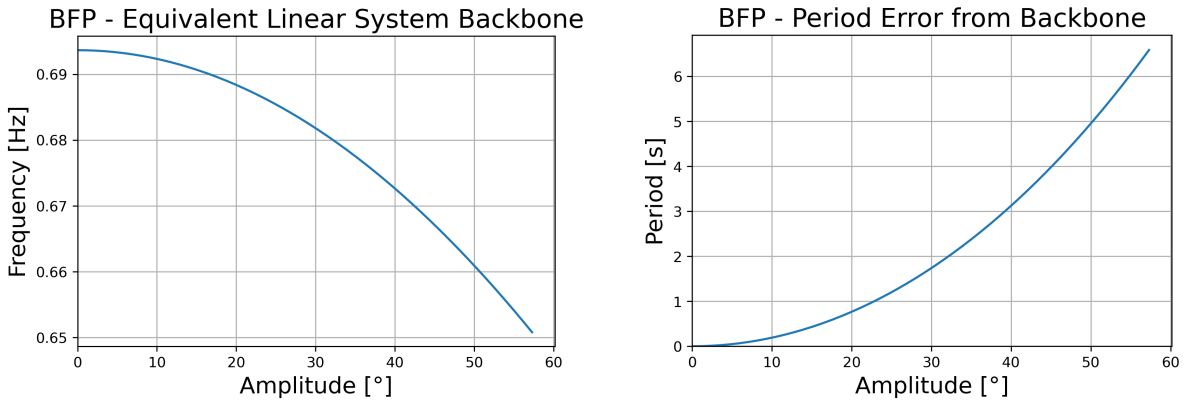


**(a)** Backbone

**(b)** Percentage uncertainty on the period

**Figure 3.6:** Backbone and period error of the ESPA system with $h = 1349.34mm$

amplitudes smaller than $10°$ are confirmed to cause very small errors. Since such amplitudes have

been found to be easily achievable during the tests, the amplitude-dependent nonlinear effects are mostly neglected in this study. When considered, they will be explicitly mentioned.

Another source of nonlinearities in the pendulum motion is the rig flexibility. This has been shown to impact the results in case very heavy bodies are tested on rigs of insufficient stiffness [27]. However, this is not the case in the present study. As discussed in Section 2.5, the structure used for the tests is very stiff, having been designed for much higher loads.

### 3.2.3. Compound Pendulum

The influence of all explicit parameters on the results of a CP test is presented here. The dependency of each parameter on the mounting height has been investigated in order to allow for an optimization of the rope length.

#### Sensitivity to Input Parameters

The derivations performed on Equation (2.6) confirm the results obtained by Blanes et al. [18].

$$\frac{\partial I_P}{\partial m} = \frac{g\zeta}{(2\pi f)^2} = \frac{I_P}{m} \tag{3.57}$$

$$\frac{\partial I_P}{\partial \zeta} = \frac{mg}{(2\pi f)^2} = \frac{I_P}{\zeta} \tag{3.58}$$

$$\frac{\partial I_P}{\partial f} = -\frac{mg\zeta}{2\pi^2 f^3} = -\frac{2}{f} I_P \tag{3.59}$$

However, the total uncertainty relative to the CP method is also highly dependent on the application of the Huygens–Steiner theorem. The derivation of the complete Equation (2.8), yields the following:

$$\frac{\partial I}{\partial m} = \frac{g\zeta}{(2\pi f)^2} - \zeta^2 = \frac{I_P - m\zeta^2}{m} = \frac{I}{m} \tag{3.60}$$

$$\frac{\partial I}{\partial \zeta} = \frac{mg}{(2\pi f)^2} - 2m\zeta = \frac{I_P}{\zeta} - 2m\zeta = \frac{I}{\zeta} - m\zeta \tag{3.61}$$

$$\frac{\partial I}{\partial f} = -\frac{mg\zeta}{2\pi^2 f^3} = -\frac{2}{f} I_P = -\frac{2}{f}(I + m\zeta^2) \tag{3.62}$$

In particular, Equation (3.62) sheds light on an important aspect. Since the order of magnitude of the frequency of oscillation will likely be $f < 1Hz$, the influence of the frequency uncertainty will be $\frac{\partial I}{\partial f} > -2I_p$. Therefore, a frequency uncertainty in the order of $\delta_f \approx 0.005Hz$ will still result in a MoI uncertainty larger than $0.01 \cdot I_p$. This can become an issue if $I_p \gg I$.

If $\tau$ is used instead of $f$, equations (3.60)-(3.62) can be rewritten as:

$$\frac{\partial I}{\partial m} = \frac{g\zeta\tau^2}{4\pi^2} - \zeta^2 = \frac{I_P - m\zeta^2}{m} = \frac{I}{m} \tag{3.63}$$

$$\frac{\partial I}{\partial \zeta} = \frac{mg\tau^2}{4\pi^2} - 2m\zeta = \frac{I_P}{\zeta} - 2m\zeta = \frac{I}{\zeta} - m\zeta \tag{3.64}$$

$$\frac{\partial I}{\partial \tau} = \frac{mg\zeta\tau}{2\pi^2} = \frac{2I_P}{\tau} = \frac{2}{\tau}(I + m\zeta^2) \tag{3.65}$$

The sum in quadrature of the three contributions from Equations (3.60)-(3.62) results in the following expression for the combined uncertainty on MoI measurement.

$$\delta I = \sqrt{\left(\frac{\partial I}{\partial m}\delta m\right)^2 + \left(\frac{\partial I}{\partial \zeta}\delta\zeta\right)^2 + \left(\frac{\partial I}{\partial f}\delta f\right)^2} \tag{3.66}$$

From this, the fractional uncertainty is obtained by dividing both sides by $I$.

$$\frac{\delta I}{I} = \sqrt{\left(\frac{\frac{\partial I}{\partial m}\delta m}{I}\right)^2 + \left(\frac{\frac{\partial I}{\partial \zeta}\delta\zeta}{I}\right)^2 + \left(\frac{\frac{\partial I}{\partial f}\delta f}{I}\right)^2} \tag{3.67}$$

The rightmost form in each of the Equations (3.60)-(3.65) is expressed as a function of the body's mass and MoI. In this form, it is possible to determine the dependency of each uncertainty component on the arm length $\zeta$. The mass component $\frac{\partial I}{\partial m}$, for example, is independent of $\zeta$, since it can be written as $\frac{I}{m}$, where both parameters are independent of $\zeta$. The $\zeta$ component $\frac{\partial I}{\partial \zeta}$, on the other hand, monotonously decreases with increasing $\zeta$. In particular, $\frac{\partial I}{\partial \zeta}$ is positive for small $\zeta$ values and negative for large ones. The optimum $\zeta$ value is the one that minimizes the absolute value of $\frac{\partial I}{\partial \zeta}$, since $\frac{\partial I}{\partial \zeta}$ multiplies $\delta\zeta$. Therefore, the optimum is achieved for $\frac{\partial I}{\partial \zeta} = 0$, yielding:

$$\zeta_{opt,\zeta} = \sqrt{\frac{I}{m}} \tag{3.68}$$

This is the radius of gyration of the body. It follows that, when the best estimate of the pendulum arm is equal to the radius of gyration of the body, the $\zeta$-dependent uncertainties become negligible.

Lastly, the frequency component $\frac{\partial I}{\partial f}$ also depends on $f$, which is in turn dependent on $\zeta$. By inverting equation (2.8), $f$ can be expressed as

$$f = \frac{1}{2\pi}\sqrt{\frac{mg\zeta}{I + m\zeta^2}} \tag{3.69}$$

Equation (3.62) then becomes

$$\frac{\partial I}{\partial f} = -4\pi\sqrt{\frac{(I + m\zeta^2)^3}{mg\zeta}} \tag{3.70}$$

Dividing both the numerator and denominator by $m$ and substituting the radius of gyration $\rho = \sqrt{\frac{I}{m}}$ yields

$$\frac{\partial I}{\partial f} = -4\pi m\sqrt{\frac{(\rho^2 + \zeta^2)^3}{g\zeta}} \tag{3.71}$$

Here, $\zeta$ appears both at the numerator and denominator, therefore the optimum pendulum length $\zeta_{opt,f}$ depends on the radius of gyration of the body. However, the optimum value grows with $\rho$, and reaches $\zeta_{opt,f} \approx 251mm$ for $\rho = 557mm$, corresponding to the radius of gyration of the OTV primary structures tested in the validation campaign.

Equations (3.68) and (3.71) can be used to optimize the rope length of the setup in order to minimize the propagation of uncertainties.

### Nonlinear Motion

The solution equation of the compound method is obtained from the equation of motion

$$I_P\ddot{\varphi} + mg\zeta\,\sin(\varphi) = 0 \tag{3.72}$$

This is generally linearized by introducing the small angles assumption $\sin(\varphi) \approx \varphi$, which allows the oscillation frequency to be easily derived as

$$f = \frac{1}{2\pi}\sqrt{\frac{mg\zeta}{I_P}} \tag{3.73}$$

Rearranging this, Equation (2.6) appears. The small angles assumption is common because small angular amplitudes are easily achieved in the CP method, as confirmed by the tests reported in Section 5.5. However, this neglects the influence of the oscillation amplitude. To assess the error introduced by this simplification, the backbone of the system can be calculated, i.e., the curve describing the relationship between oscillation frequency and motion amplitude.

To achieve this, the sine was substituted with the first terms of its Taylor expansion at 0: $\sin(\varphi) \approx \varphi - \frac{\varphi^3}{3!} + \frac{\varphi^5}{5!}$. The equivalent linear system could then be derived through equivalent linearization. From

this, the backbone of the system was derived, as described by Dimitriadis [26]. The resulting backbone equation is:

$$f(A) = \frac{1}{2\pi}\sqrt{\frac{mg\zeta\left(1 - \frac{A^2}{8} + \frac{A^4}{192}\right)}{I_P}} \tag{3.74}$$

Where $A$ is the amplitude of motion, in radians.

Substituting into Equation (3.74) the properties of the ESPA, with $\zeta = 1713.87mm$, corresponding to a rope length of 1500mm, yields the plot in Figure 3.7.

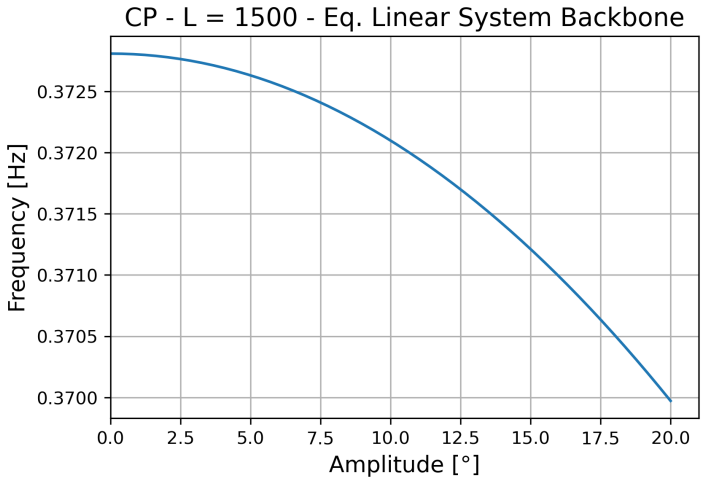


**Figure 3.7:** Backbone of equivalent linear system

# 4

# Verification Through Simulation

To verify the methodology and assess that all methods would yield the intended results, a CAD model of the test setup was created. Through this, the tests were performed virtually. This also allowed for some risk mitigation, ensuring that accidents such as the tested object crashing into the test rig would not happen.

The simulations have been run on the CAD model of the ESPA. In the simulations, the body, ropes, and test rig are treated as rigid bodies. This choice, which highly streamlined the process, is justified by the relative low impact of small deformations on the body's inertia properties, and by the use of steel wire ropes and a very stiff testing rig. The ropes, in particular, were modeled as simple sketch lines, constrained on one side to the body and on the other to the fixed frame. The constraints only locked the translational degrees of freedom, leaving the rope free to rotate. Unless otherwise specified, the ropes were modeled as 1500 mm long.

The results of each simulation are compared with the values extracted from the CAD model of the specimen. For the purposes of this simulation study, the CAD values are regarded as correct, since they are calculated by the CAD software with extremely low uncertainties (reportedly less than 0.01%). Therefore, the difference between the simulation results and the CAD predictions defines the error. For example, if the mass $m$ is estimated through the simulated test, the error will be $m - m_{CAD}$, while the relative error will be $\frac{m-m_{CAD}}{m_{CAD}}$.

Each simulation is followed by a sensitivity analysis. Here, small errors are introduced in the input quantities to simulate acquisition errors and assess their influence on the final results.

## 4.1. Simulation of Suspended Multi-Point Weighing

To simulate the suspended multi-point weighing test, the CAD model of the ESPA was suspended by three ropes (sketch lines). The simulation was initially given a high value for damping, in order to let the body achieve a state of equilibrium. This is similar to what happens in the physical test, in which the acquisition lasts several minutes to let the body stabilize. Then, the tension on each rope was read, simulating the acquisition through load cells, and multiplied by the cosine of the rope angle as per Equation (2.10). The horizontal coordinates $x_G$ and $y_G$ of the CoG were computed using Equation (2.14), while the mass resulted from the sum of the vertical components of the rope tensions divided by the gravitational acceleration. Finally, the results were compared with the values extracted from the CAD: $x_{G,CAD}$, $y_{G,CAD}$, and $m_{CAD}$. To allow for easier verification of the requirements introduced in Section 2.1, the fractional errors on the CoG coordinates were calculated as a percentage not of the CAD values, but of the maximum (envelope) dimension of the body in the direction of measurement: $x_{max}$, $y_{max}$, and $z_{max}$. Both these and the CAD values are presented in Table 4.1.

The measured input values $P_i$ and $\alpha_i$, as well as the results $x_G$, $y_G$, and $m$ are presented in Table 4.2. The source of the errors is to be found in the body orientation. The forces and angles on the ropes were calculated by inspecting the CAD model in its equilibrium position, and can therefore be

**Table 4.1:** CAD values of mass and CoG coordinates and envelope dimensions of ESPA

| Parameter | Value |
|---|---|
| $x_{G,CAD}$ | 264.14 mm |
| $y_{G,CAD}$ | 152.36 mm |
| $z_{G,CAD}$ | 429.88 mm |
| $m_{CAD}$ | 20.634 kg |
| $x_{max}$ | 690 mm |
| $y_{max}$ | 690 mm |
| $z_{max}$ | 945 mm |

**Table 4.2:** Inputs and results from MPW simulation

| | Parameter | Value | Percentage Error |
|---|---|---|---|
| Input | $P_1$ | 92.93 N | - |
| | $P_2$ | 82.68 N | - |
| | $P_3$ | 79.31 N | - |
| | $\alpha_1$ | 39.79° | - |
| | $\alpha_2$ | 39.13° | - |
| | $\alpha_3$ | 32.51° | - |
| Results | $x_G$ | 254.49 mm | 1.39% |
| | $y_G$ | 151.06 mm | 0.19% |
| | $m$ | 20.634 kg | 0.00% |

considered accurate. The only deviation from the ideal conditions is that, since the body was left free to find its equilibrium position on its own, the final orientation it settles at is not perfectly horizontal, as the hypotheses of the method would want. In this case, the tilt angle the body settled at was 0.96°. This shows the importance of taking the time to adjust the rope lengths and reach an equilibrium orientation with a low tilt.

The mass was calculated exactly as $m = 20.634kg = m_{CAD}$. This was to be expected, as this measurement depends solely on the forces and angles on the ropes. It is however a confirmation that the errors on these values is indeed negligible.

To assess the sensitivity of the results to the load cells readings, each of the rope forces was, in turn, first increased and then decreased by $0.1N$. In all cases, the influence of the simulated error on the calculated CoG coordinates was at most $0.08$% of the value of the coordinate, while their influence on the mass calculation was, in all cases, $0.04$%. If errors were introduced on multiple ropes, their propagated effects would often add up on some results but cancel out on others, and in any case never amount to more than $0.16$%. Considering the requirements and the accuracy of the load cells, this influence is absolutely marginal. The same method was applied to the rope tilt angles, increasing and decreasing each of them and combinations of them by 1°. In this case, the influence was always less than $0.8$% on the CoG coordinates, and less than $0.4$% on the mass.

It is important to note that these results agree with the analytical derivations. If the data from the model is substituted into Equations (3.16)-(3.26), the expected uncertainty propagating from an uncertainty $\delta P_i = 0.1N$ is about $0.05$% for CoG coordinates and about $0.04$% on the mass, while an uncertainty $\delta\alpha_i = 1°$ would result in a propagated uncertainty of about $0.5$% for both CoG coordinates and mass.

## 4.2. Simulation of Bifilar Suspension

The BS method was simulated by suppressing one of the ropes and repositioning the body at its stable equilibrium position. Then, the forces of the ropes and rope tilt angles were obtained in the same way as for the MPW method. The body tilt angle $\beta$ was measured. The solution equations were used to calculate $z_G$ and another estimate of $x_G$ and $m$. To do so, the value for $y_G$ was extracted from the results of the suspended MPW simulation. Finally, the percentage errors were calculated using the values in Table 4.1. The results are summarized in Table 4.3.

**Table 4.3:** Inputs and results from BS simulation

| | Parameter | Value | Percentage Error |
|---|---|---|---|
| Input | $P_1$ | 124.25 N | - |
| | $P_2$ | 124.25 N | - |
| | $\alpha_1$ | 35.45° | - |
| | $\alpha_2$ | 35.45° | - |
| | $\beta$ | 19.52° | - |
| Results | $x_G$ | 263.96 mm | 0.03% |
| | $m$ | 20.634 kg | 0.00% |
| | $z_G$ | 426.20 mm | 0.39% |

The calculated mass is, like in the MPW simulation, extremely accurate. The calculated $x_G$ is very close to the CAD value, which reflects the fact that the $x$ axis achieved a very low tilt in this configuration. Lastly, the error on $z_G$ is the same as the error on $y_G$ for the previous step. That is because $z_G$ is calculated through Equation (2.15), where $y_G$ is divided by the tangent of $\beta$. The latter was, in this case, measured directly on the CAD model, and introduced very small errors.

To verify the error propagation of each parameter onto the final result, the calculations were repeated with slightly modified values of $\beta$ and $y_G$. Modifying $\beta$ by $\Delta\beta = 1°$ led to a change in the resulting $z_G$ of $-5.28$% when $\beta$ was modified by excess, and of $5.83$% when $\beta$ was modified by defect. These are in close accordance with the value of $5.54$% predicted by Equation (3.30). It has also been verified that the values approach the analytical predictions as the introduced $\Delta\beta$ gets smaller. Modifying $y_G$ by $\Delta y_G = \pm 5mm$ led to a change in the resulting $z_G$ of $\pm 3.31$%, which equals the value predicted by Equation (3.29).

## 4.3. Simulation of Bifilar Pendulum

The third simulation reproduced the BFP method. The oscillation period was acquired and the MoI was obtained through the solution equation. To simulate the acquisition of the oscillating motion through the load cells as was initially intended, the time-dependent force at the top of the ropes was plotted. The resulting plot showed a very small difference between the maximum and minimum values. This might pose a challenge during the actual tests, as the acquisition noise may be larger than the difference in values to be measured. To address this issue, the simulation was rerun, this time measuring the acceleration on the body to simulate the acquisition through an accelerometer. Comparatively, the difference between the maximum and minimum values was much more significant in the latter case. Therefore, it was concluded that the accelerometer acquisition method is preferable.

All simulations were run for a duration corresponding to two complete oscillations, with a time discretization of $0.003s$, and for multiple values of the initial oscillation amplitude $A_0$. The relative error with respect to the value from the CAD was calculated as

$$err_I = \left| \frac{I_{CAD} - I}{I_{CAD}} \right| \tag{4.1}$$

With $I_{CAD} = 2.31kg \cdot m^2$. The results obtained from the forces on the ropes are shown in Table 4.4. Here, it is easy to spot a monotonous decrease of measurement error with decreasing oscillation

**Table 4.4:** BFP simulation results obtained from acquisition of rope loads with large oscillation amplitudes

| $A_0$ [°] | $\tau$ [$s$] | $I$ [$kg \cdot m^2$] | $err_I$ |
|---|---|---|---|
| 20 | 1.466 | 2.39 | 3.35% |
| 15 | 1.455 | 2.35 | 1.87% |
| 10 | 1.448 | 2.33 | 0.82% |
| 5 | 1.445 | 2.32 | 0.41% |

amplitudes. This can be attributed to the nonlinear effects of large-amplitude motion, as discussed in

Section 3.2.2. However, it is important to note how, even for a very large initial amplitude such as $20°$, the errors are well within the given constraints.

The most important result from this simulation is that, with amplitudes lower than $5°$, the variations in force on the ropes become so small that even the software can no longer plot a smooth curve, which appears instead broken up into steps, as if the force on the ropes did not vary continuously. Furthermore, the forces on the two ropes varied with slightly different frequencies, yielding separate results. The results are presented in Table 4.5.

**Table 4.5:** BFP simulation results obtained from acquisition of rope loads with small oscillation amplitudes

| $A_0$ [°] | $\tau_1$ [$s$] | $\tau_2$ [$s$] | $I_1$ [$kg \cdot m^2$] | $I_2$ [$kg \cdot m^2$] | $err_{I,1}$ | $err_{I,2}$ |
|---|---|---|---|---|---|---|
| 2 | 1.448 | 1.436 | 2.33 | 2.29 | 0.82% | 0.84% |
| 1 | 1.458 | 1.410 | 2.36 | 2.21 | 2.29% | 4.33% |

As shown in Table 4.6 and illustrated in Figure 4.1, when the period is obtained from the plot of the acceleration tangent to the rotational motion, the error keeps decreasing with the amplitude, at least until $A_0 = 1°$. This is because, even with such a small amplitude, the acceleration oscillates roughly between $+200\frac{mm}{s^2}$ and $-200\frac{mm}{s^2}$. This interval is well within the discerning capabilities of the software and of the available accelerometer. Conversely, this oscillation amplitude resulted in a maximum difference of 0.1 N between the maximum and minimum recorded forces. This represents a small fraction of the Full Scale of the used load cells. For these reasons, the decision was made to include an accelerometer in the test. Figure 4.1 also compares the MoI error from the simulation to the one obtained with the

**Table 4.6:** BFP simulation results obtained from acquisition of body acceleration

| $A_0$ [°] | $\tau$ [$s$] | $I$ [$kg \cdot m^2$] | $err_I$ |
|---|---|---|---|
| 20 deg | 1.466 | 2.39 | 3.35% |
| 15 deg | 1.455 | 2.35 | 1.87% |
| 10 deg | 1.448 | 2.33 | 0.82% |
| 5 deg | 1.445 | 2.32 | 0.41% |
| 2 deg | 1.443 | 2.31 | 0.2% |
| 1 deg | 1.443 | 2.31 | 0.2% |

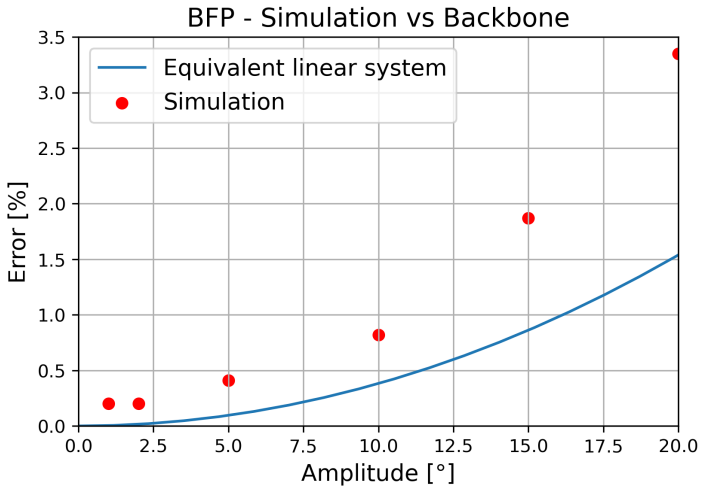


**Figure 4.1:** Comparison between MoI values obtained through simulation and from the backbone of the BFP

amplitude-dependent frequency backbone derived in Section 3.2.2. The trend is similar, with small differences at low amplitudes, due to the small errors in the simulation data. At amplitudes larger than 10°, the two data sets start to visibly diverge. At $A_0 \approx 20°$, the simulation error becomes twice as large as the analytical one.

As for the other methods, the error propagation of each parameter on the final result was assessed by repeating the calculations with slightly modified values. All results very closely matched the analytical derivations. The geometrical parameters $a$, $b$, and $h$ were all modified by $\pm 10mm$. The resulting variation in the calculated MoI was of $1.04\%$ for $a$ and $3.28\%$ for $b$, both matching the analytical predictions to 10 significant figures, while it was of about $0.74\%$ for $h$, matching the prediction to three significant figures. The mass $m$ was altered by $\pm 0.1kg$, resulting in a change in MoI of $0.48\%$, matching the predictions to 10 significant figures. Lastly, a change in the measured period $\tau$ of $\pm 0.01s$ resulted in an MoI change of about $1.39\%$, matching the prediction to two significant figures.

## 4.4. Simulation of Compound Pendulum

In general, two steps of CP are required to determine both the pitch and the yaw MoI. Here, however, only one step was carried out. The second step was deemed unnecessary, as the relevance of this simulation study is not in the results but rather in verifying the method and determining the influence of the involved parameters. All results from this simulation are reported in Appendix C.

Like the BFP simulations, the CP ones showed a very small difference between the maximum and minimum forces to be measured by the load cells. Again, measuring the acceleration instead resulted in a larger range, which led to the decision of using an accelerometer for all dynamic tests. The results discussed here are therefore those relative to the calculations run on the acceleration on the body.

The rope length was initially set as $L = 1500mm$, corresponding to $\zeta = 1713.87mm$ as in the previous simulations. The simulations were run for a duration corresponding to four complete oscillations, with a time discretization of $0.01s$. To solve Equation (2.8) the mass was extracted from the CAD, while the oscillation period resulted from the simulation itself, just like for the other methods. The pendulum arm length $\zeta$ was calculated through Equation (2.19), where $z_G$ was extracted from the results of the MPW and BS simulations. The relative errors were again calculated through Equation (4.1), this time with $I_{CAD} = 2.62kg \cdot m^2$. The calculated MoI values were also compared to those obtained with $\zeta = \zeta_{CAD}$, where $\zeta_{CAD}$ is the value of the distance between the pendulum axis and the CoG as measured directly on the CAD model. All results are reported in Table C.1.

This method, like the BFP, shows noticeable error reductions associated with lower oscillation amplitudes. As shown in Figure 4.2, the errors on $I_{\zeta_{CAD}}$ are in close accordance with the analytical backbone curve derived in Section 3.2.3. However, even for small amplitudes, the error is still quite large. This was attributed to the way errors propagate through the equations of the CP, discussed analytically in Section 3.2.3.

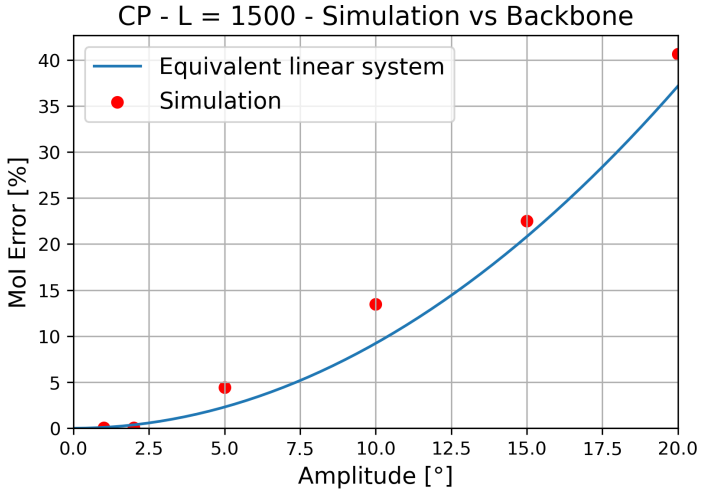


**Figure 4.2:** Comparison between MoI values obtained through simulation ($I_{\zeta_{CAD}}$) and from the backbone of the CP

Through Equation (3.68) the optimum value of $\zeta$ for which Equation (3.61) reaches 0 can be calculated as $\zeta_{opt,\zeta} = \sqrt{\frac{I}{m}} \approx 356.16mm$. This value is physically incompatible with the body, since it is

lower than the expected $z_G$, which would result in the body being suspended above the test rig, with the ropes acting in compression. The $\zeta_{opt,f}$ value that minimizes frequency-dependent uncertainties is even lower. Therefore, to minimize the combined uncertainty, the ropes should be shortened as much as possible. It should be noted that this result is not general, and for bodies of different shape and mass distribution there may indeed be a suitable value of $\zeta$ for which the $\frac{\partial I}{\partial \zeta}$ component goes to 0.

To verify the discussion above, the simulations were rerun for several different rope lengths: $L = 1500mm$ ($\zeta = 1713.87mm$), $L = 1250mm$ ($\zeta = 1409.74mm$), $L = 1000mm$ ($\zeta = 1061.63mm$), $L = 800mm$ ($\zeta = 627.76mm$). Again, the MoI was calculated from both $\zeta$ and $\zeta_{CAD}$. The comparison between $I$ and $I_{\zeta_{CAD}}$ enabled both the assessment of the effects of error propagation and the verification of the method itself. Like for the first simulation, the $I_{\zeta_{CAD}}$ values from all simulations closely matched the backbone. The results presented in Tables C.1-C.4 are a clear confirmation of the discussion above. For better visualization, these are also illustrated in Figures 4.3 and 4.4.

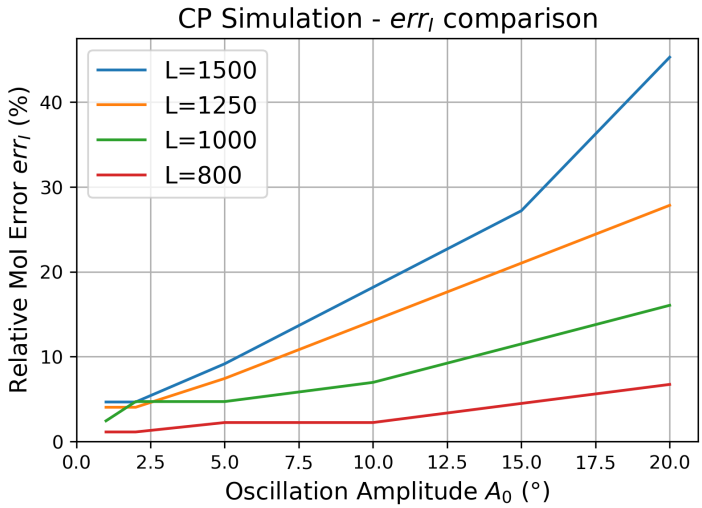


**Figure 4.3:** Simulated CP dependency of the MoI error on the oscillation amplitude for different values of rope length. MoI calculated with $\zeta$ from static simulations.

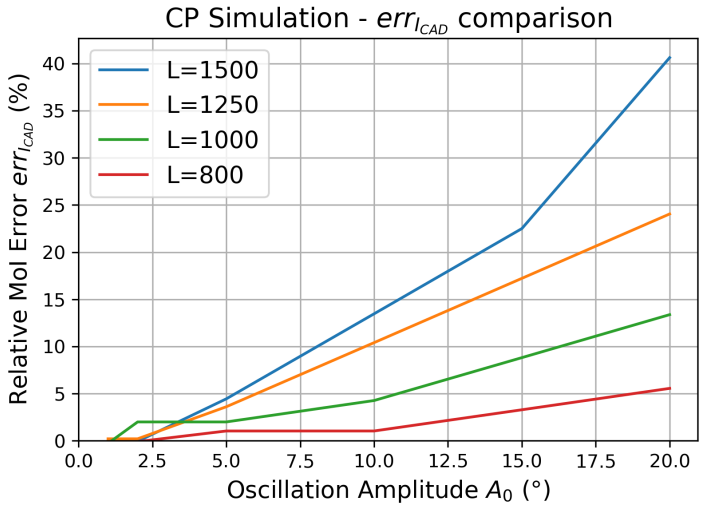


**Figure 4.4:** Simulated CP dependency of the MoI error on the oscillation amplitude for different values of rope length. MoI calculated with $\zeta$ measured from the CAD.

Both $I$ and $I_{\zeta_{CAD}}$ achieve achieve much lower errors with shorter ropes, especially at high oscillation amplitudes. In particular, $I_{\zeta_{CAD}}$ converges to negligible errors at low amplitudes for any rope length.

Yet, at an amplitude $A_0 = 20°$, it achieves an acceptable accuracy (<10%) only with the shortest ropes. Another important result is that $I$ did not converge to the same error levels for all rope lengths, but instead achieved much higher accuracy with shorter ropes. This, together with the differences in values between $I$ and $I_{\zeta_{CAD}}$, indicates that the error found on the first iteration ($L = 1500$) is a direct symptom of the error on $\zeta$ being amplified by the $\frac{\partial I}{\partial \zeta}$ term discussed in Section 3.2.3.

Lastly, to verify the results sensitivity to errors on the mass and the oscillation period, the calculations for $A_0 = 1°$ were rerun for all rope lengths with slightly modified values of these two parameters. The period value was increased and decreased by $0.01s$, which resulted in variations in the MoI consistently within 0.3% of the expected values from Equation (3.65). The mass was modified by $0.1kg$, which caused a change in MoI of $0.48$% in all cases, in accordance with the expected values from Equation (3.60).

# 5

# Pre-Validation Campaign

This chapter presents the results of the first round of tests, referred to as pre-validation. This was performed in order to validate the methodology for general purposes and identify criticalities and possible improvements. As such, the steps taken differ slightly from the definitive version of the test design described in Chapter 2. The differences are highlighted when present.

The chosen test item is an ESPA, a body of simple geometry and composed of a low number of parts of known materials. This allowed for a simplified validation step, which would make it easier to identify criticalities due to the lower number of variables.

The rope length was chosen in this case as a trade-off between the requirements displayed by Previati's study [25] on the BFP and the simulation results of the CP (Section 4.4). The former show that nonlinear effects generally increase for shorter rope lengths, while the latter found higher errors for longer ropes. Since the nonlinear effects on a BFP with the parameters of the proposed test were unknown, being outside of Previati's [25] scope, while the CP errors had been studied analytically and through simulation, the former was given higher priority in the trade-off. A rope length of $1200mm$ was chosen because, according to the simulations, it should have yielded acceptable results with the CP method, as long as the oscillation amplitude was smaller than 10 degrees, while still keeping the ratio $\frac{R}{L}$ of the mounting radius $R$ and the rope length $L$ as small as possible. However, the results were not acceptable, which led to greatly reducing the length of the ropes for the OTV test campaign.

All assumptions are stated, and all measurements and results are presented with justified uncertainty values and confidence levels, following the *GUM* guidelines [23]. The uncertainties on the results have been calculated by combining the standard deviations of the parameters, and multiplying the resulting value by the t-factor associated to the desired confidence level, according to the discussion in Section 3.1.3.

## 5.1. Test Objectives and Success Criteria

The test campaign had the following objectives:

- Practical evaluation of the testing methodology on the following parameters:
  - Total hardware cost
  - Total testing times
  - Uncertainties on mass, CoG, MoI
- Identify criticalities and possible future improvements

Given the test objectives, the test campaign would be declared successful based on the following success criteria:

- The total hardware cost of the campaign is below €5000, as per requirement C1

- The testing times do not exceed 48 man-hours, as per requirement S1
- Mass, CoG and MoI values are obtained, with justified uncertainty values and confidence levels
- No damage occurs to the tested object, based on visual inspection

Furthermore, the test campaign was intended to validate the developed testing methodology for general purposes. To achieve this, the obtained results would need to comply with all the applicable requirements among those listed in section 2.1.

## 5.2. Suspended Multi-Point Weighing

The suspended MPW test was performed as explained in Section 2.3.1, except for the fact that the inclinometer was not yet available, so all angles were measured with a protractor. The test item was suspended by three ropes, each equipped with a load cell and a turnbuckle for adjusting its length. Figure 5.1 shows a picture of the setup and its main functional parts.

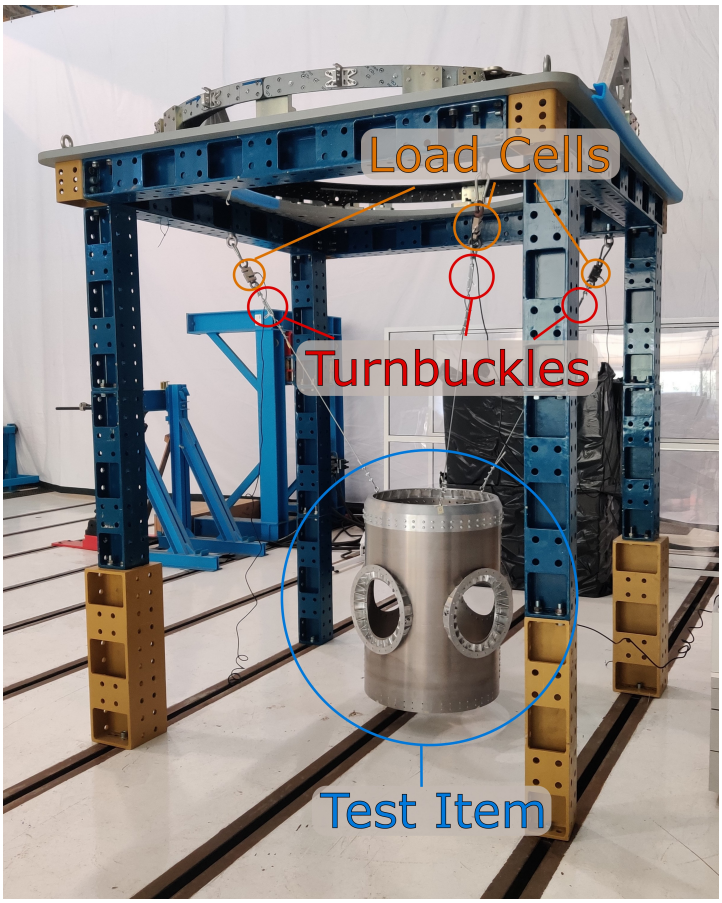


**Figure 5.1:** Test setup for suspended MPW

Three iterations of the test were performed, rotating the body by $120°$ each time to cycle the support points of the load cells. This was done to assess that the results are not strongly dependent on which load cell measures which point. If that were the case, it could either mean that the load cells are faulty, that the method itself is, or that something else is not working as expected.

Given the inclinometer was not available at the time of testing, the XY plane's horizontality was assessed with a level, while the rope tilt angles $\alpha_i$ were measured with a protractor, as shown in Figure 5.2. This involves of course much higher uncertainties, so these measurements were repeated 5 times for the first configuration ($A$) and 3 times for the following two ($B$, $C$), in order to calculate the statistical uncertainties. Table 5.1 shows the measured rope tilt angles for configurations A, B, and C. In the table, the letters A, B, or C represents the configuration, while the subscript numbers represent

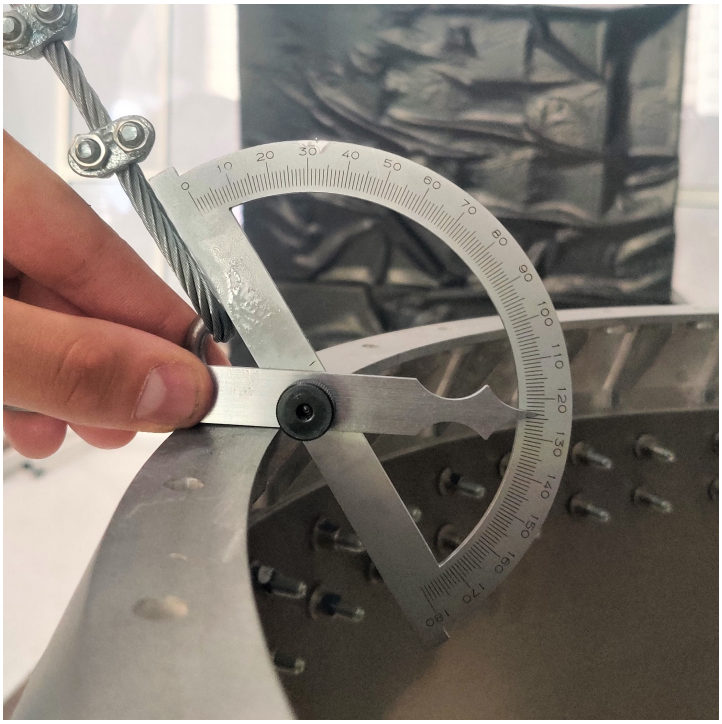

**Figure 5.2:** Measurement of the rope tilt with a protractor

the repeated acquisitions of the parameters. Given the low number of acquisitions, a t-distribution

**Table 5.1:** Measured parameters during the test

| Set | $\alpha_1$ [°] | $\alpha_2$ [°] | $\alpha_3$ [°] |
|---|---|---|---|
| $A_1$ | 34 | 33 | 30 |
| $A_2$ | 31 | 30 | 29 |
| $A_3$ | 30 | 29 | 28 |
| $A_4$ | 28 | 28 | 29 |
| $A_5$ | 31 | 29 | 29 |
| $B_1$ | 31 | 28 | 30 |
| $B_2$ | 30 | 27 | 30 |
| $B_3$ | 28 | 27 | 28 |
| $C_1$ | 29 | 30 | 30 |
| $C_2$ | 28 | 29 | 29 |
| $C_3$ | 28 | 28 | 28 |

was assumed (see Section 3.1.3), with a t-factor of $2.78$ for the first configuration, and of $4.30$ for the other two. These values were obtained from the table in Appendix B and correspond to a confidence level of 95%, under the assumption that the measurements are independent of each other. Given the low accuracy of the measurement method, an additional uncertainty due to systematic effects of $2°$ was assumed, with a confidence of 68%, equivalent to $3.92°$ with 95% uncertainty, assuming normal distribution. The combined uncertainty was calculated through Equation (3.9). This resulted in the average and uncertainty values presented in Table 5.2. The resulting uncertainties are quite high, which justifies the use of an inclinometer for the measurements.

The loads on the ropes are calculated by the post-processing script. The script loads the acquired load cells signal for each of the three configurations and calculates the average, removing the noisy first segment. It then transforms these average values into kilograms through the calibration coefficients, thus obtaining the $P_i$ required to solve Equation (2.14). The resulting values are shown in Table 5.2.

The maximum error of the load cells was provided by the manufacturer as 0.05% of the full scale load

**Table 5.2:** Average and uncertainty values of $\alpha_i$ for each of the three suspended MPW configurations

| Configuration | $\alpha_1$ [°] | $\alpha_2$ [°] | $\alpha_3$ [°] | $P_1$ [$kg$] | $P_2$ [$kg$] | $P_3$ [$kg$] |
|---|---|---|---|---|---|---|
| $A$ | $29.80 \pm 7.71$ | $29.00 \pm 5.90$ | $30.80 \pm 8.20$ | $8.17 \pm 0.12$ | $7.87 \pm 0.12$ | $8.17 \pm 0.12$ |
| $B$ | $29.67 \pm 10.82$ | $27.33 \pm 8.95$ | $29.33 \pm 9.93$ | $8.14 \pm 0.12$ | $7.89 \pm 0.12$ | $8.13 \pm 0.12$ |
| $C$ | $29.00 \pm 9.62$ | $28.33 \pm 8.95$ | $29.00 \pm 9.62$ | $8.19 \pm 0.12$ | $7.88 \pm 0.12$ | $8.07 \pm 0.12$ |

of $200kg$. The cells are certified C2 according to the OIML R 60 standard [28]. This standard features a maximum permissible error which cannot be exceeded for the certification to be granted. It follows that all 2000 measurements taken during the certification tests were within the specified interval. In this case, the variance of the results can be calculated through Equation (3.12). The resulting standard deviation is $\sigma_{Pi} = 0.06kg$, which, multiplied by the t-factor $t = 1.96$ for a 95% confidence, results in the reported uncertainty of $\delta P_i = 0.12kg$.

The locations of the three rope connection points $\begin{bmatrix} x_{B_i} \\ y_{B_i} \end{bmatrix}$ were determined from the CAD to be $\begin{bmatrix} 0 \\ 0 \end{bmatrix}$, $\begin{bmatrix} 527.929 \\ 0 \end{bmatrix}$, and $\begin{bmatrix} 263.965 \\ 457.200 \end{bmatrix}$. The first one is where the coordinate system is centered by definition.

Given that the coordinates of the rope connection points were extracted directly from the CAD, the uncertainty on the position of the points themselves was assumed to be equal to the dimensional tolerance of $0.1mm$ given to the manufacturer, with an attributed confidence of 95%. This was added in quadrature to the position uncertainty of the eye bolt itself, which is equal to the clearance between the bolt and the hole. In this case, the clearance was $0.5mm$. This as well was attributed a confidence level of 95%. The resulting 95% confidence interval is

$$\delta_{x_{B_i}} = \delta_{y_{B_i}} = \sqrt{0.1^2 + 0.5^2} = 0.51mm \tag{5.1}$$

Then, the standard deviation is $\sigma_{x_{B_i}} = \sigma_{y_{B_i}} = \frac{0.51}{1.96} = 0.26mm$

The gathered data was used to solve Equations (2.13), (2.14) for the mass and CoG coordinates, and (3.16)-(3.28) for the uncertainties.

The standard deviations of the results have been estimated through Equation (3.9), and were then multiplied by an appropriate t-factor to calculate the uncertainty. To do so, the standard deviations of the parameters must be known.

The t-factors for each result were calculated based on a confidence level of 95%. To determine the appropriate number of degrees of freedom for $\delta x_G$ and $\delta y_G$, the recommendations by Coleman and Steele [22] discussed in Section 3.1.3 were followed. The dominant terms were the ones related to the rope tilt $\alpha_i$. Therefore, the degrees of freedom were set equal to three times the degrees of freedom of $\delta\alpha_i$ (once for each rope). This led to the following degrees of freedom:

- Configuration $A$: $\nu_{x_G} = \nu_{y_G} = 3 \cdot 4 = 12$
- Configurations $B$, $C$: $\nu_{x_G} = \nu_{y_G} = 3 \cdot 2 = 6$

For the mass, the uncertainty contributions related to $\delta\alpha_i$ and $\delta P_i$ were equally important and with a different number of degrees of freedom. $\delta P_i$ was assumed to have a very high number of degrees of freedom $\nu \to \infty$. Therefore, the Welch–Satterthwaite formula was used (Equation (3.10)). This resulted in values very similar to those chosen for the other two results. Therefore, for all configurations, $\nu_m = \nu_{x_G} = \nu_{y_G}$.

This yielded the results in Table 5.3. The fourth row shows the values obtained from combining the results and uncertainties from the three configurations with the inverse-variance weighting method introduced in Section 3.1.5.

The fractional uncertainties on the CoG coordinates have been calculated as a percentage of the maximum dimension of the body in the direction of measurement $x_{max} = y_{max} = 690mm$. These range from 0.96% to 1.19%, and reduce to 0.60% and 0.58% when averaged. The uncertainties on the mass are within acceptable margins as well, ranging between 3.14% and 3.48% of the total mass for the single measurements, and reducing to 1.91% for the average estimate.

**Table 5.3:** Results of suspended MPW test on ESPA

| Configuration | $x_G\ [mm]$ | $\frac{\delta x_G}{x_{max}}$ [%] | $y_G\ [mm]$ | $\frac{\delta y_G}{y_{max}}$ [%] | $m\ [kg]$ | $\frac{\delta m}{m}$ [%] |
|---|---|---|---|---|---|---|
| $A$ | $264.89 \pm 8.23$ | 1.19 | $149.91 \pm 6.70$ | 0.97 | $20.99 \pm 0.73$ | 3.48 |
| $B$ | $263.14 \pm 7.09$ | 1.03 | $153.15 \pm 7.22$ | 1.05 | $21.17 \pm 0.70$ | 3.32 |
| $C$ | $265.46 \pm 6.63$ | 0.96 | $154.76 \pm 6.91$ | 1.00 | $21.16 \pm 0.66$ | 3.14 |
| Average | $264.51 \pm 4.17$ | 0.60 | $152.53 \pm 4.00$ | 0.58 | $21.11 \pm 0.40$ | 1.91 |

Overall, these results show that the uncertainty achievable on the mass and horizontal CoG coordinates can be satisfactory even using a low-precision instrument for the angle measurements. The results from the three configurations are compatible, i.e., the uncertainty ranges overlap.

The results show that it is not necessary to rotate the body three times on future tests. The slight reduction in uncertainty does not justify the extra work necessary to repeat all measurements.

## 5.3. Bifilar Suspension

The BS method, as introduced in Section 2.3.2, uses the body tilt $\beta$ achieved after detaching one of the ropes to determine the $z$ component of the CoG, as well as allowing the calculation of a new estimate of $x_G$ and $m$. The test setup is shown in Figure 5.3, with the body tilt angle highlighted.


**Figure 5.3:** Test setup for BS

The BS configuration is achieved by detaching one rope, leaving only the ones whose connection point lies on the $x$ axis of the coordinate system described in Section 2.3.1. The coordinates of the

connection points of the remaining ropes are $\begin{bmatrix}0\\0\end{bmatrix}$ and $\begin{bmatrix}527.929\\0\end{bmatrix}$ with the same uncertainties reported in Section 5.2.

The loads and tilts on the ropes and their uncertainties were obtained in the same way as in the suspended MPW step. The resulting values are $P_1 = 11.90 \pm 0.12kg$, $P_2 = 11.81 \pm 0.12kg$ for the loads and $\alpha_1 = 20.67 \pm 8.95°$, $\alpha_2 = 22.83 \pm 8.69°$ for the angles. The confidence on the angle uncertainties is, again, 95%.

The BS step requires to measure the body tilt $\beta$. This was, again, performed with a protractor, as shown in Figure 5.4. The $\beta$ measurement was repeated 5 times, resulting in an average of $19.30°$.

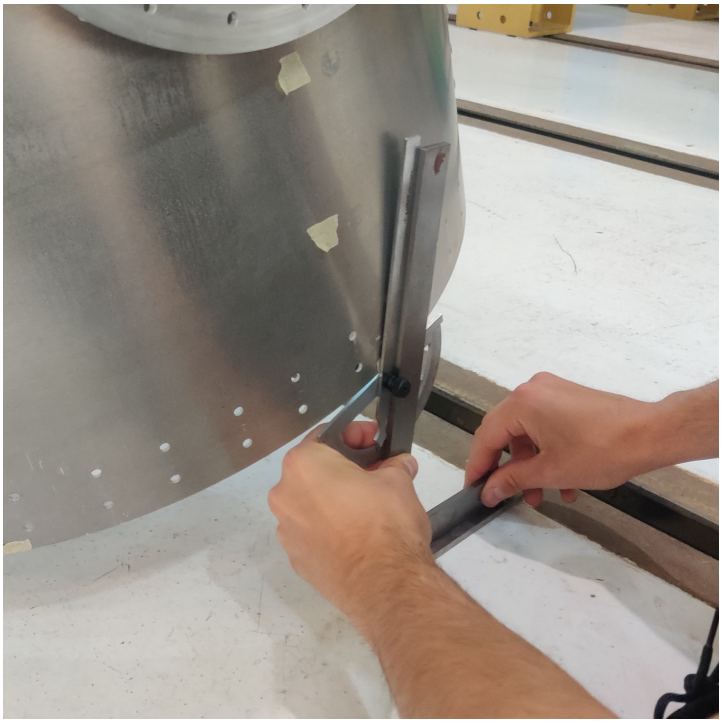

**Figure 5.4:** Measurement of the body tilt with a protractor

Assuming t-distribution with independent acquisitions, the uncertainty was calculated as $\pm 1.24°$ with 95% confidence. Lastly, $y_G$ is required to calculate $z_G$. This comes directly from the results of the suspended MPW step in Section 5.2.

The data on rope loads and tilts was used to obtain new estimates of $x_G$ and $m$, while the measured body tilt $\beta$ was combined with the previously known best estimate of $y_G$ (from the average of the three MPW configurations) to obtain $z_G$. The results are presented in Table 5.4.

**Table 5.4:** Results of BS test on ESPA

| Parameter | Value |
|---|---|
| $x_{G,susp}$ | $266.98 \pm 5.76mm$ |
| $m_{susp}$ | $22.02 \pm 0.48kg$ |
| $z_G$ | $435.57 \pm 33.16mm$ |

The reported uncertainties have been obtained analogously as for the MPW method, combining the standard deviations of the parameters and multiplying the result by the t-factor for 95% confidence. The degrees of freedom of $\delta x_{G,susp}$ and $\delta m_{susp}$ were calculated through the Welch–Satterthwaite formula (Equation (3.10)), while the degrees of freedom of $\delta z_G$ were assumed equal to the ones of $\delta\beta$, since this term is the dominant one.

- $\nu_{x_{G,susp}} = 5$

- $\nu_{m_{susp}} = 5$
- $\nu_{z_G} = 4$

The uncertainties on $x_G$ and $m$ are lower than all the ones from the previous test. This could be linked to the smaller number of uncertainty sources resulting from the use of two ropes rather than three. On the other hand, $z_G$ displayed a high uncertainty value, considering the low uncertainties on $y_G$ and $\beta$. This is still well within the given margins for CoG determination, at $3.51\%$ of the maximum height of the vehicle $z_{max} = 945mm$, but it is quite relevant, especially considering that $z_G$ is used in the CP solution equation as well, and contributes to its uncertainty. This high uncertainty propagation is due to the relatively small angle difference between the horizontal and tilted configuration, as previously discussed in Section 3.2.1.

The $x_{G,susp}$ and $m_{susp}$ values have been averaged with the previous results through the inverse-variance weighting method. The final, combined results of the suspended MPW and BS methods are reported in Table 5.5. All uncertainties are well in compliance with the requirements, and the values present a good accordance with the CAD. The $x_G$ and $y_G$ are both within less than 0.15% of the CAD predictions, while $z_G$ is within 1.32%. Lastly, the measured mass is 4.49% smaller than expected from the CAD model. Comparing the results with the CAD predictions provides a simple way to estimate whether the test results are plausible. If the test and the predictions are sufficiently close, the existence of very large errors in the methods can be excluded, such as incorrect equations or wrong assumptions.

**Table 5.5:** Combined Results of Suspended MPW and BS Methods

| Parameter | Value | Uncertainty | Deviation from CAD |
|---|---|---|---|
| $x_G$ | $265.36 \pm 3.38mm$ | 0.49% | 0.14% |
| $y_G$ | $152.53 \pm 4.00mm$ | 0.58% | 0.02% |
| $z_G$ | $435.57 \pm 33.16mm$ | 3.51% | 1.32% |
| $m$ | $21.49 \pm 0.31kg$ | 1.44% | 4.49% |

## 5.4. Bifilar Pendulum

The BFP method was used to calculate the roll MoI of the body. In this first campaign, the load cells and turnbuckles were kept as part of the suspension system, instead of being removed for the dynamic tests as described in Section 2.4.1. The oscillating motion was acquired 6 consecutive times through the load cells as well as a triaxial accelerometer. Figure 5.5 shows setup with the body suspended by two ropes, ready for the test.

The amplitude of the excited oscillation was not directly measured, but inspection of the footage revealed it to be approximately $10°$ each time.

To calculate the vertical distance between the connection points on the specimen and on the rig, the length and tilt of the two ropes had to be measured. The measurements were repeated three times and combined assuming t-distribution with independent measurements and 95% confidence. The results are presented in Table 5.6, with the aforementioned uncertainties being the ones listed under the label *Type A Uncertainty*.

**Table 5.6:** Measured angles and rope lengths during BFP test on ESPA

| Parameter | Value | Type A Uncertainty | Total Uncertainty |
|---|---|---|---|
| $\alpha_1$ | $30.3°$ | $2.5°$ | $4.6°$ |
| $\alpha_2$ | $28.0°$ | $0.0°$ | $3.9°$ |
| $L_1$ | $1264.33mm$ | $6.57mm$ | $20.67mm$ |
| $L_2$ | $1264.33mm$ | $9.93mm$ | $21.97mm$ |

The type A uncertainty obtained for $\alpha_2$ highlights a weakness of using statistical methods for determining uncertainties with such a low number of observations. If all measurements yield the same

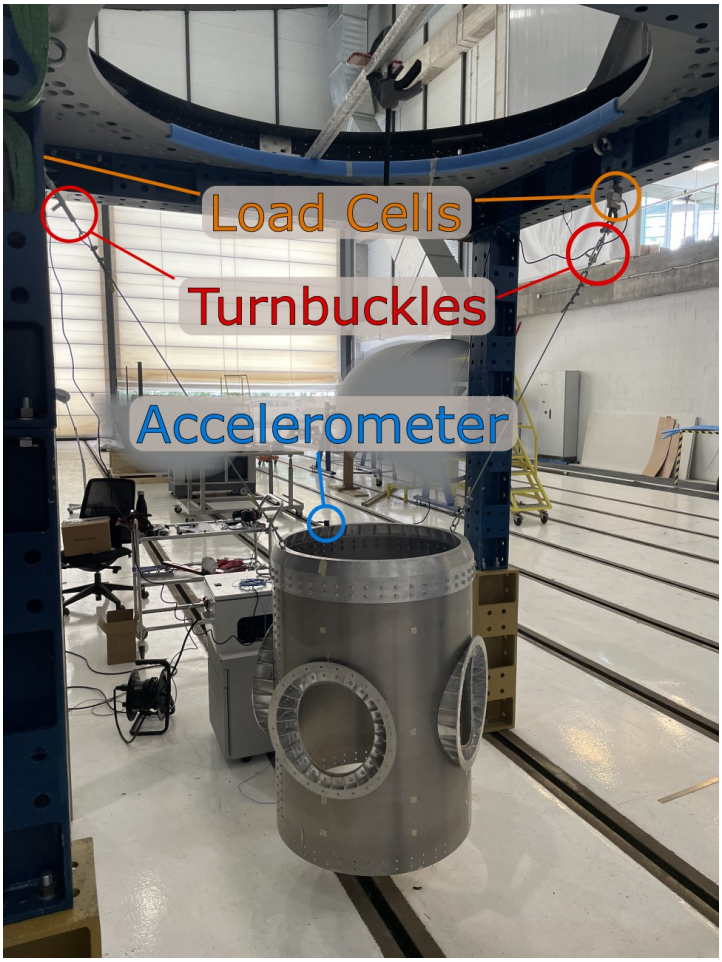


**Figure 5.5:** Test setup for BFP

value, the uncertainty is 0, which is unrealistic. The minimum number of direct measurements of a geometrical property with statistically-determined uncertainty was increased to 10 for the OTV tests to reduce the chance of this happening, as well as improve the overall quality of the gathered data.

Given the low accuracy associated with using a protractor for such measurements. The total uncertainty on the angles was increased by adding a systematic component of $3.92°$ in quadrature, like in the previous tests. The rope length presents a systematic error source as well. Given that the rope is not a simple one-dimensional rope, but is made of several components, it was found not easy to determine the exact points of beginning and end of the swinging portion. Therefore, an uncertainty component must be included and added in quadrature to the values above. After careful consideration of the rope setup and inspection of the test footage, the standard uncertainty due to this systematic effect was assumed to be of $10mm$, meaning $19.60mm$ with $95$% uncertainty, assuming normal distribution. The final uncertainty values are reported in Table 5.6 under column *Total Uncertainty*.

The length and tilt values were used to calculate $h_1$ and $h_2$ through Equation (2.18). Then the two values were combined through inverse-variance weighting to obtain the estimate of $h$ necessary for Equation (2.4). This resulted in $h = 1104.94 \pm 46.44mm$, with 95% confidence.

The mass $m$ of the object and its standard deviation $\sigma_m$ are the results of the static tests, while the values of the mounting radii $a = 960.0mm$ and $b = 304.8mm$ were obtained from the CAD, as justified in Section 2.4.1. The uncertainties on the mounting radii were set equal to the amount of clearance between the eye bolts and the holes in which they are respectively mounted. Assuming the bolts are initially centered, the maximum amount of relative movement they can have is twice the clearance itself. However, since their distances have been defined as $2a$ and $2b$ (see Figure 2.1), the uncertainty on $a$ and $b$ is half that amount. This results in $\delta a = 1.8mm$, $\delta b = 0.5mm$. These uncertainties were assumed

to encompass two standard deviations, so that $\sigma_a = \frac{\delta a}{2}$ and $\sigma_b = \frac{\delta b}{2}$. Given its negligible influence, the manufacturing error margin of $0.1mm$ considered for the suspended MPW method was not taken into account here.

The oscillation frequency was calculated by the post-processing Python script from the accelerometer signals. The signal was multiplied by a window function to reduce leakage, and a Fast Fourier Transform was performed to determine the frequency peaks. Then, the one relative to the oscillation was identified. All accelerometer axes were able to capture the motion: the $x$ axis was directed in tangential direction, so it measured the tangential acceleration; the $y$ axis was towards the center of the body, so it measured the centripetal acceleration; the z axis was pointing upwards, so it measured the vertical motion of the body due to the fixed length of the ropes (this has twice the frequency of the rotational oscillation). The results from the $z$ axis were discarded after being analyzed and deemed less accurate. While the $x$ and $y$ axes almost always agreed on the peak frequency, the $z$ axis often gave slightly different results. Furthermore, the frequency peaks generated by the $x$ and $y$ axes were found to be much sharper than those generated by the $z$ axis. This can be verified in Figure 5.6.

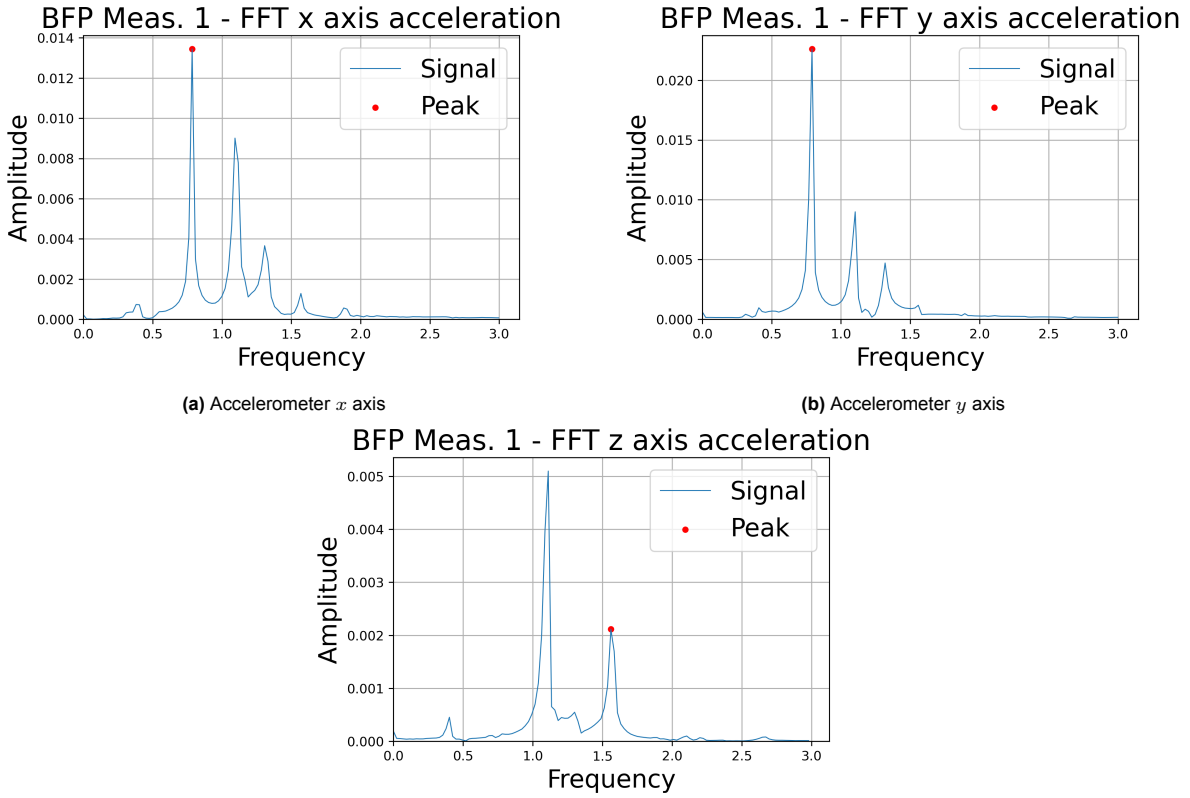


**(a)** Accelerometer $x$ axis

**(b)** Accelerometer $y$ axis

**(c)** Accelerometer $z$ axis

**Figure 5.6:** Plotted Fast Fourier Transform results, obtained from the readings of the $x$, $y$, and $z$ axes of the accelerometer

For each of the 6 acquisitions, the estimates from the $x$ and $y$ axes were averaged. This resulted in 6 frequency values, which were combined assuming t-distribution with 5 degrees of freedom, resulting in $f = 0.801 \pm 0.021Hz$ with 95% confidence. The motion was recorded using the load cells as well. The acquisition noise in the signals, however, proved much larger than the forces that needed to be measured, making the acquisition useless, as predicted in Section 4.3. For this reason, the cells were not employed for the ensuing tests.

To determine the influence of nonlinearities the useful portion of the signal (i.e., without the first part containing the initial impulse) was divided into three equal intervals. A Fourier transform was performed on all three, yielding compatible results. More importantly, the deviations were non-monotonous, meaning the measured frequency did not monotonously increase or decrease as the interval moved towards the end of the acquisition time span. This is a sign that nonlinearities due to structural or aerodynamic

damping, which would result in monotonous deviations, have very little influence.

The calculated MoI is $I = 2.20 \pm 0.15 kg \cdot m^2$. The uncertainty on the MoI has been calculated by propagating the standard deviations of all considered uncertainty sources and multiplying the results by the t-factor $2.57$, corresponding to $\nu_I = 5$ degrees of freedom at 95% confidence. The degrees of freedom have been set equal to the frequency ones, since the latter has a dominant influence on the combined uncertainty, in accordance to the discussion in Section 3.1.3.

Expressing the uncertainty as a percentage yields $\frac{\delta_I}{I} = 6.80\%$. On the other hand, the percentage difference between the calculated MoI and the value predicted by the CAD software ($I_{CAD} = 2.50 kg{\cdot}m^2$) is $\frac{I - I_{CAD}}{I_{CAD}} = -11.80\%$. This is almost twice as much as the estimated uncertainty, and is unlikely related solely to the differences between the physical object and the CAD model, especially considering that the measured mass is in close accordance with the CAD value. These results point to an undetected or underestimated source of systematic errors.

To try to identify the source of the observed errors, a second BFP test campaign was performed on the ESPA. The test was repeated twice. In the first iteration, the same setup was used as for the previous tests, except for the length of the rope assemblies, which was reduced to 800mm. This was done to test whether shorter ropes would result in lower errors, as was observed in the CP simulations. In the second test, the steel rope was substituted with slings (see Figure 5.7) of adjustable length, thus avoiding the need for turnbuckles and shackles. These rigid parts were observed during the tests to oscillate in a more constrained fashion, likely due to the friction forces preventing them from swinging freely. Substituting the steel assembly with slings, the system was expected to behave more closely to the ideal one from which the equations were derived. In addition, for these tests, the digital inclinometer shown in Figure 5.8 was available. This helped to reduce the uncertainties on the vertical distance between the body and the rig.

**Figure 5.7:** Sling model used for the tests

The results of both tests are reported in Table 5.7. The steel ropes show slightly improved uncertainty compared to the previous iteration, but lower accordance with the CAD values. Based on these results, the BFP method does not appear to be positively influenced by shortening the ropes. The combined uncertainty is largely dominated by the frequency component, with a frequency standard deviation of $\sigma_f = 0.014 Hz$ propagating to a MoI uncertainty of $0.14 kg \cdot m^2$. The other two components have a negligible impact. The increase in the $I - I_{CAD}$ difference was attributed to the increased $\frac{R}{L}$ ratio between the mounting radius of the ropes and their length. This, as discussed in Section 3.2.2, introduces nonlinear effects which can impact the results. For this reason, the mounting position of the ropes on the rig was changed in the following test involving the slings. Instead of supporting the body from two opposite beams as in Figure 5.5, the ropes were mounted on the same beam, at a much closer distance, similar to the diameter of the body. This made the slings almost perfectly vertical, with measured tilts of more than 88°. The results from this new test setup show a considerable reduction in the uncertainty due to a much smaller scatter between the measured frequencies. The standard deviation of the frequency measurements is of $\sigma_f = 0.006 Hz$, while the deviation from the CAD prediction is still above 10%. Therefore, substituting the steel ropes with slings led to a higher repeatability in the frequency readings, but did not improve the test's agreement with the CAD predictions. The consistently observed deviation of around $-12\%$ could be interpreted as a sign that the measured MoI


**Figure 5.8:** Inclinometer used for tilt measurements

**Table 5.7:** Results of second iteration of BFP tests on ESPA

| Rope Type | MoI $[kg \cdot m^2]$ | Uncertainty | Deviation from CAD |
|---|---|---|---|
| Steel Ropes | $2.16 \pm 0.14$ | $6.51\%$ | $-13.76\%$ |
| Slings | $2.21 \pm 0.07$ | $3.31\%$ | $-11.56\%$ |

is correct, while the CAD model presents some important inaccuracies that make it unrepresentative of the physical object. This, however, is unlikely, given the high level of accordance to the CAD displayed by the results of the static methods. The MoI is dependent on the mass and its distribution. Given that the mass measurements are much closer to the CAD predictions than the MoI ones, the deviations should be due in large part to the mass distribution. However, large variations in mass distribution would determine a shift in the CoG position. That is, unless the variations happened symmetrically around the CoG, which is unlikely. Therefore, since the measured CoG coordinates agree well with the predictions, the observed deviations are not justified.

## 5.5. Compound Pendulum

The last two steps of the test campaign measure the MoI values about the pitch and yaw axes. These employ the same method: the CP. The test setup, depicted in Figure 5.9, again features turnbuckles on each rope, and involves both the load cells and the accelerometer as motion sensing equipment. However, as for the BFP test, the load cells acquisition proved useless. The figure also highlights the way the ropes were connected. Two ropes on each side of the body connect to the same point on the test rig, forming a swing-like setup.

The amplitude of the excited oscillation was not directly measured, since the available equipment did not allow for it, but inspection of the footage revealed it to be smaller than $1°$ for each acquisition. This shows that low motion amplitudes can be achieved without issue, thus greatly reducing the risk of the amplitude-dependent errors discussed in section 4.4.

The rope lengths and tilts for all four ropes were evaluated as for the previous steps. These values were substituted into Equation (2.18) to calculate four estimates of the vertical component of the rope length $h_i$, which were then combined through inverse-variance weighting to obtain the best estimate $h$ and its standard uncertainty (68% confidence). This, added to the $z_G$ estimate from the static tests yields the pendulum arm length. The values obtained for the pitch configuration are reported in Table 5.8. The same procedure was followed for the yaw configuration, leading to an arm length of $\zeta_{\text{yaw}} = 1439.57$ with a standard uncertainty of $\sigma_{\zeta_{\text{yaw}}} = 17.76mm$.

The motion was acquired five times for each of the two configurations. Differently from the BFP test,

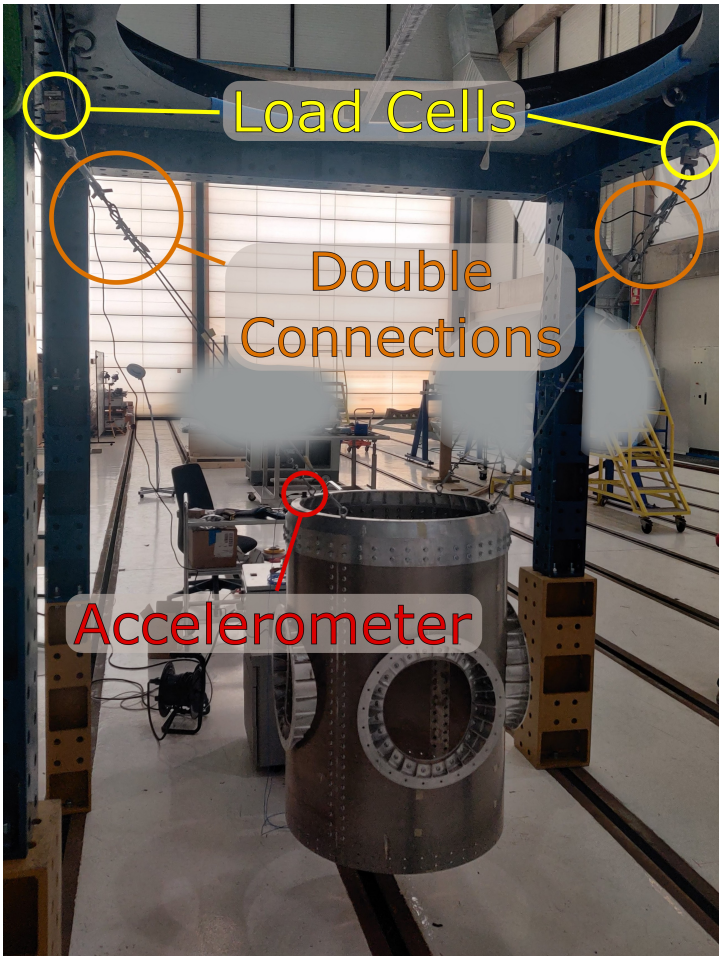


**Figure 5.9:** Test setup for CP test

only one accelerometer axis was used, i.e., the one pointing in the direction of the swinging motion. The frequencies were again obtained through a FFT on Python. The 5 values were combined assuming t-distribution with 4 degrees of freedom, resulting in $f_{\text{pitch}} = 0.417 \pm 0.006 Hz$ and $f_{\text{yaw}} = 0.417 \pm 0.014 Hz$, both with 95% confidence. Actively leakage reduction (discussed in Section 2.4.1) had a large impact especially on the pitch frequency estimate, reducing the standard deviation by more than four times.

Like in the BFP post-processing, the useful portion of the signal was divided into three equal intervals. The resulting frequencies were compatible, and the deviation were non-monotonous, demonstrating the small influence of non-linear effects.

The results of the CP test in pitch configuration are reported in Table 5.9. Here, $I_P$ is the MoI of the body with respect to the pendulum axis, while $I$ is its MoI about the prescribed pitch or yaw axis. The uncertainties are related to random errors alone, and have been calculated with a t-factor of $2.78$, corresponding to $\nu_I = 4$ degrees of freedom at 95% confidence. The degrees of freedom have been

**Table 5.8:** Vertical length of each rope $h_i$, their average $h_{\text{pitch}}$, and calculated pendulum arm $\zeta_{\text{pitch}}$

| Parameter | Value |
|---|---|
| $h_1$ | $993.68 \pm 26.88mm$ |
| $h_2$ | $994.08 \pm 26.16mm$ |
| $h_3$ | $998.95 \pm 27.03mm$ |
| $h_4$ | $992.62 \pm 26.90mm$ |
| $h_{\text{pitch}}$ | $994.81 \pm 13.37mm$ |
| $\zeta_{\text{pitch}}$ | $1430.38 \pm 17.92mm$ |

set equal to the frequency ones, since the latter has a dominant influence on the combined uncertainty, in accordance to the discussion in Section 3.1.3.

**Table 5.9:** Results of CP Test in Pitch and Yaw Configurations

| Parameter | Value |
|---|---|
| $I_{P,\text{pitch}}$ | $43.79 \pm 2.23\, kg \cdot m^2$ |
| $I_{\text{pitch}}$ | $-0.18 \pm 2.10\, kg \cdot m^2$ |
| $I_{P,\text{yaw}}$ | $44.10 \pm 3.18\, kg \cdot m^2$ |
| $I_{\text{yaw}}$ | $-0.43 \pm 3.10\, kg \cdot m^2$ |

Clearly, these results are far from acceptable. The uncertainties are close to 100% of the expected MoI $I_{CAD} = 2.84kg{\cdot}m^2$, and both configurations yielded negative values, which does not make physical sense. This happened even though the uncertainties on the input parameters were comparable to those achieved for the BFP test. However, it should be noted that both the $I_P$ estimates present uncertainties of less than $8$% of the respective $I_P$ values, and are relatively close to the expected values of approximately $47kg \cdot m^2$. The large errors on $I_{pitch}$ and $I_{\text{yaw}}$ appear due to out-of-scale influence of the Steiner term $-m\zeta^2$ in Equation (2.8). If the ropes are rather long, as in this case, the term becomes much larger in absolute value than the actual MoI of the body. Then, a small error in the MoI of the pendulum translates to a much larger error in the small MoI of the body.

Given the unsatisfactory results, the CP tests were repeated with modified parameters to investigate the error sources. The tests were run only in pitch configuration. Like in the previous BFP tests, the CP test was run first with steel ropes attached to opposite beams, and then with slings attached at a distance similar to the body diameter. The ropes were shortened to reduce the impact of the Steiner term on the calculated MoI. The initial length of 1200mm was reduced to 800mm, which reduced the pendulum arm length to $\zeta \approx 633mm$. The length of the slings was made the same as that of the steel ropes, to achieve a similar pendulum arm in both tests. Like in the repetition of the BFP tests, the digital inclinometer shown in Figure 5.8 was available. The results are presented in Table 5.10. While still far from the acceptability range, these results represent a vast improvement on the previous tests. The conspicuous accuracy increase was attributed to the only variable that was modified between the previous set of tests and the current test with steel ropes: the rope length. Furthermore, the switch to slings mounted closer together greatly reduced both the combined uncertainty and the divergence from the predictions. This suggests that either the rigidness of the turnbuckles or the rope attachment radius on the rig had a high impact on the results.

**Table 5.10:** Results of second iteration of CP tests on ESPA

| Rope Type | MoI $[kg \cdot m^2]$ | Uncertainty | Deviation from CAD |
|---|---|---|---|
| Steel Ropes | $1.36 \pm 1.24$ | $91.40$% | $-52.24$% |
| Slings | $2.03 \pm 0.94$ | $46.41$% | $-28.42$% |

## 5.6. Success Criteria and Requirements Satisfaction

Based on the success criteria listed in Section 5.1, the test campaign was declared successful. However, not all tests satisfied the requirements, so the methodology could not be declared validated. Table 5.11 lists the requirements pertaining to the pre-validation test campaign. For each requirement, the verification method and satisfaction status is shown.

The state of fulfillment of all functional and performance requirements can be verified from the discussion of the ESPA test campaign. The environmental requirement E1 was verified, since the test was conducted at the RFA Portugal facility, while requirement E2 was verified by comparing the dimensions of the setup with the available space at the German facility.

Furthermore, requirement S1's satisfaction can be verified from Table 5.12, listing the approximate time each step of the campaign took with a team of two, as the total man-hours employed for the tests is then twice the total from the table, resulting in 15 man-hours.

**Table 5.11:** Requirements satisfaction matrix for the inertia testing campaign on the ESPA

| ID | Statement | Verification Method | Satisfied |
|---|---|---|---|
| F1 | The procedure shall provide sufficient data to determine the mass of the vehicle. | Test | Yes |
| F2 | The procedure shall provide sufficient data to determine the CoG coordinates of the vehicle. | Test | Yes |
| F3 | The procedure shall provide sufficient data to determine the MoI of the vehicle about its specified roll, pitch, and yaw axes. | Test | Yes |
| F4 | The results shall include justified uncertainty values. | Uncertainty analysis | Yes |
| P1 | The total uncertainty on the mass measurement shall be below 10% of the measured value. | Uncertainty analysis | Yes |
| P2 | The total uncertainty on the determination of the $x$ coordinate of the CoG coordinate shall be below 10% of the vehicle's maximum dimension in $x$ direction. | Uncertainty analysis | Yes |
| P3 | The total uncertainty on the determination of the $y$ coordinate of the CoG coordinate shall be below 10% of the vehicle's maximum dimension in $y$ direction. | Uncertainty analysis | Yes |
| P4 | The total uncertainty on the determination of the $z$ coordinate of the CoG coordinate shall be below 10% of the vehicle's maximum dimension in $z$ direction. | Uncertainty analysis | Yes |
| P5 | The total uncertainty on the measurement of the roll MoI shall be below 10% of the measured value. | Uncertainty analysis | Yes |
| P6 | The total uncertainty on the measurement of the pitch MoI shall be below 10% of the measured value. | Uncertainty analysis | No |
| P7 | The total uncertainty on the measurement of the yaw MoI shall be below 10% of the measured value. | Uncertainty analysis | No |
| E1 | The test setup shall fit the RFA Portugal test facility. | Visual inspection | Yes |
| E2 | The test setup should fit the RFA Germany test facility. | Geometrical measurements | Yes |
| S1 | The full test campaign should not require more than 48 man-hours. | Schedule | Yes |
| C1 | The cost for the company of newly bought hardware shall not exceed €5000. | Cost assessment | Yes |
| C2 | The cost for the company of newly bought hardware should not exceed €1000. | Cost assessment | Yes |

Lastly, cost requirements C1 and C2 were both satisfied, as the total hardware-related cost for the company was below €300.

The most critical results, both in terms of uncertainty and of prediction matching, come from the CP method. To improve these results, the uncertainties $\sigma_m$, $\sigma_\zeta$, and $\sigma_f$ could be further reduced. Additionally, an optimum value of the pendulum arm $\zeta$ could be determined that minimizes the respective

**Table 5.12:** Duration of each step in the ESPA test campaign

| Test | Duration |
|---|---|
| Preparation | 60 min |
| Calibration | 60 min |
| Suspended Multi-Point Weighing | 90 min |
| Bifilar Suspension | 60 min |
| Bifilar Pendulum | 60 min |
| Compound Pendulum – Pitch MoI | 60 min |
| Compound Pendulum – Yaw MoI | 60 min |

influences of each of the three uncertainty sources. These aspects have been analyzed in a study on the influence of the main parameters involved in the method. This is presented in Chapter 6.

# 6

# Compound Pendulum Optimization Study

The results presented in Section 5.5 highlighted an important limitation of the CP method: its high sensitivity to the uncertainty on frequency measurements. This chapter presents a parametric study that investigates in detail which parameters can be fine-tuned to reduce the effect of the frequency uncertainty on the final results, and attempts to estimate the optimum combination of acquisition length and number to minimize the total test time.

## 6.1. Parametric Study

The frequency sensitivity of the CP, together with its high dependency on the arm length uncertainty discussed in Section 4.4 poses stringent requirements on the test setup design. To investigate said requirements, a study was conducted on the influence of the following parameters on the combined uncertainty:

- Body mass $m$
- Measured MoI $I$
- Radius of Gyration $\rho$
- Pendulum arm length $\zeta$
- Standard uncertainty on the mass value $\sigma_m$
- Standard uncertainty on the arm length value $\sigma_\zeta$
- Standard uncertainty on the frequency value $\sigma_f$

A python script takes as input the mass of the vehicle and its uncertainties on the mass, arm length, and frequency along with the body's mass. Then, it iterates through several values of $\rho$ and calculates, for a large variety of $m$ and $\zeta$ values, the combined uncertainty $\delta I$.

The use of the radius of gyration instead of the MoI allows the mass and MoI to be treated as a single variable. For convenience, the square of the radius of gyration is used here, equal to:

$$\rho^2 = \frac{I}{m} \tag{6.1}$$

Therefore, for each value of $\rho$, the MoI is uniquely determined by the mass. This greatly simplifies the visualization of the results with no loss of generality. Instead of dedicating two plot axes to the mass and MoI, only one is used to represent both, and the $\rho^2$ value is reported.

The independent variables, $m$, $\zeta$, and $\rho^2$ each assume a range values designed to represent a variety of use cases. Specifically, $m$ varies between 10 and 1000 kg, $\zeta$ varies between 100 and 2000

mm, and $\rho^2$ assumes the following values:

$$\rho^2 \in \{1,\ 1.1,\ 2,\ 3,\ 3.1,\ 4,\ 5\} \cdot 10^5\, mm^2 \tag{6.2}$$

These values are representative of a wide range of potential test items, including the ones treated in this work. The ESPA has a mass of about 20 kg and a $\rho^2 \approx 1.1 \cdot 10^5 mm^2$, and was tested with a $\zeta = 1430.38mm$. The tested OTV structures have a mass of 79 kg and a $\rho^2 \approx 3.1 \cdot 10^5 mm^2$. The fully assembled OTV will have a mass of about $350kg$ and a $\rho^2 \approx 4 \cdot 10^5 mm^2$. The frequency of oscillation is calculated from Equation (3.73).

The standard uncertainties on the input parameters were initially set as follows, to represent the ones obtained during the first pre-validation tests:

- $\sigma_m = 0.15kg$
- $\sigma_\zeta = 20mm$
- $\sigma_f = 0.01Hz$

The t-factor associated with the distribution of the frequency readings and, as a result, the calculated MoI values (see Section 3.1.3), was set as 2.78, assuming 5 independent readings. This was done in order to calculate a value for the combined uncertainty, but it does not impact the most important results of this study, which is the optimum length of the pendulum arm.

Figure 6.1a shows the dependency of $\delta I$ on $m$ and $\zeta$ for $\rho^2 = 3.1 \cdot 10^5 mm^2$, corresponding to the OTV primary structures to be tested. The same is plotted in Figure 6.1b for the fractional uncertainty $\frac{\delta I}{I}$.

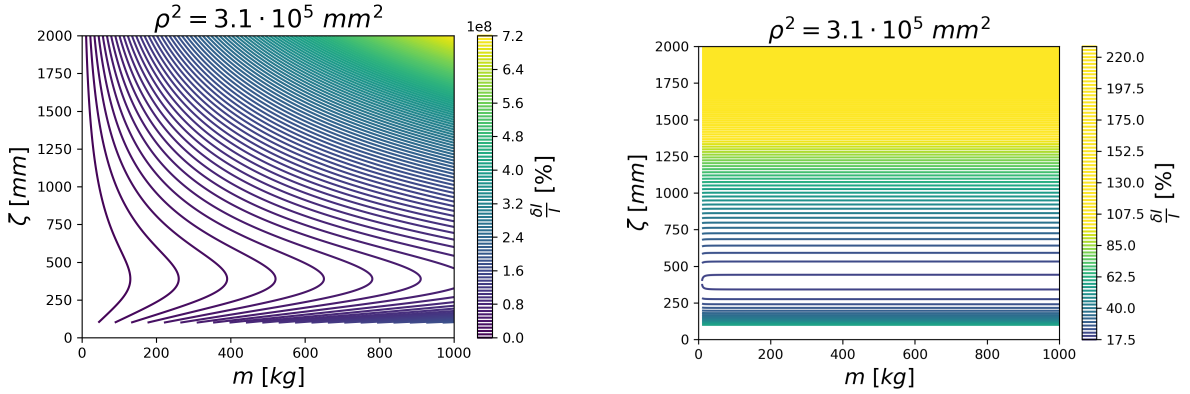


**(a)** Absolute uncertainty

**(b)** Fractional uncertainty

**Figure 6.1:** MoI uncertainty as a function of $m$ and $\zeta$ for $\rho^2 = 3.1 \cdot 10^5 mm^2$, $\sigma_m = 0.15kg$, $\sigma_\zeta = 20mm$, $\sigma_f = 0.01Hz$

The results show that, for a given value of $\rho^2$, the fractional uncertainty is almost independent of the mass (and MoI) of the body. The only dependency is registered for very low masses and, even then, it is very weak. For this reason, the uncertainty can be plotted as a function of $\zeta$ alone, as in Figure 6.2.

The plots show that the fractional uncertainty presents a minimum at an optimum value $\zeta_{opt} = 389mm$. This is the result of the interplay between the propagation of $\sigma_f$ and $\sigma_\zeta$. According to the discussion in Section 3.2.3, the former presents a minimum at $\zeta_{opt,f} = 251mm$, while the latter has its minimum at $\zeta_{opt,\zeta} = 560.94mm$. The optimum $\zeta$ value is a trade-off between the two effects.

The uncertainty values, its minimum, and the $\zeta_{opt}$ at which it can be achieved are all dependent on the specimen's radius of gyration $\rho$. Figure 6.3 shows how, for the aforementioned set of input uncertainties, the minimum achievable uncertainty slightly increases with growing values of $\rho$. On the other hand, the uncertainties for higher values of $\zeta$ show a strong decrease with increasing $\rho$. This decrease reduces the dependency of the uncertainty on $\zeta$, especially for $\zeta \approx \zeta_{opt}$. Therefore, for bodies of high radius of gyration it becomes less critical to achieve $\zeta = \zeta_{opt}$. To summarize, while a lower radius of gyration makes it possible to achieve a slightly lower uncertainty for a given set of input

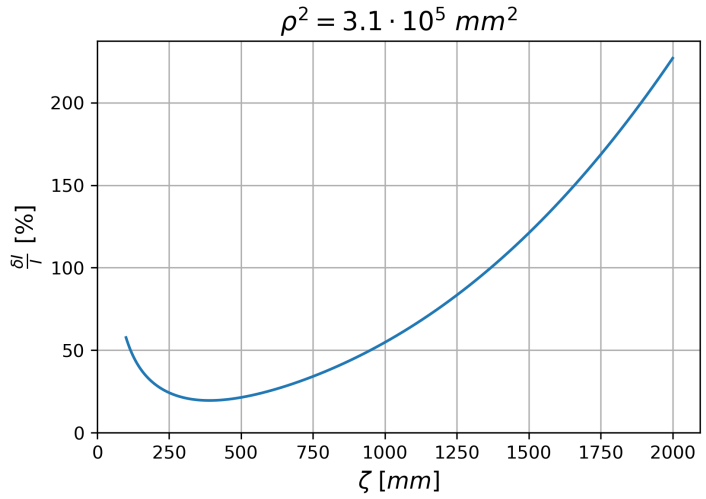


**Figure 6.2:** MoI uncertainty as a function of $\zeta$ for $\rho^2 = 3.1 \cdot 10^5 mm^2$, $\sigma_m = 0.15kg$, $\sigma_\zeta = 20mm$, $\sigma_f = 0.01Hz$

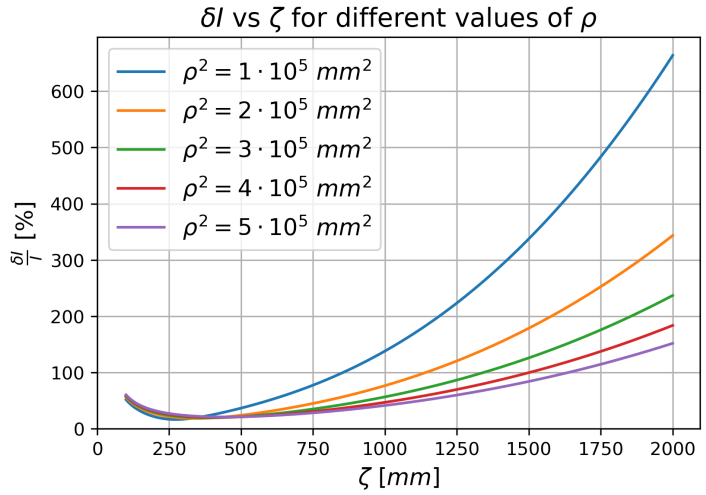


**Figure 6.3:** Influence of the radius of gyration on the MoI uncertainty curve for fixed values of the input uncertainties $\sigma_m$, $\sigma_{zeta}$, and $\sigma_f$

uncertainties, a higher one makes it easier to obtain low values in general. It is important to note that the input uncertainties cannot be accurately known until after the tests have been performed, hence the tool developed here is dependent on the assumption of said uncertainties. As a result, it can happen that the predicted $\zeta_{opt}$ is not the same as the actual one. For this reason, a low uncertainty dependency is highly preferable, which makes the CP more suited for bodies with a high radius of gyration. Another factor in favor of bodies with a high $\rho$ is that $\zeta_{opt}$ increases with increasing $\rho$. A high $\zeta_{opt}$ is desirable, since low $\zeta$ values can be difficult or even impossible to achieve, depending on the geometry of the body.

With the chosen input, the percentage uncertainty at $\zeta_{opt}$ is 16.41% (for $\rho^2 = 1 \cdot 10^5 mm^2$) and 20.91% (for $\rho^2 = 5 \cdot 10^5 mm^2$). This shows that it is impossible to achieve the required uncertainty levels with the chosen parameters. Since the inertia parameters of the body cannot be modified, the only way to ensure compliance with the requirements is to reduce the input uncertainties and then tune the value of $\zeta$ to achieve a value as close as possible to the minimum output uncertainty for the chosen parameters.

Furthermore, it was observed that $\sigma_m$ and $\sigma_\zeta$ have negligible impact on the minimum combined uncertainty, with respective contributions of approximately $0.04$% and $0.10$%. As a result, only a reduction to the frequency uncertainty $\sigma_f$ can significantly reduce the minimum achievable uncertainty on the

MoI.

It should be clarified that the statement above does not imply that $\sigma_\zeta$ has a small impact on the combined uncertainty in general, but rather that it does not highly affect the achievable minimum combined uncertainty. The reason behind this is that said minimum uncertainty is calculated at $\zeta_{opt}$. This is relatively close to $\zeta_{opt,\zeta}$ (Equation (3.68)) which minimizes the influence of $\sigma_\zeta$ on the combined uncertainty. Therefore, it is natural that $\sigma_\zeta$ would have such a small impact on that specific result. However, this does not imply that $\zeta$ has a small impact in general. For example, for $\rho^2 = 4 \cdot 10^5 mm^2$ and $\zeta = 1000mm$, a standard uncertainty of $\sigma_\zeta = 20mm$ would propagate to a fractional uncertainty of $\left(\frac{\sigma_I}{I}\right)_{\sigma_\zeta} = 3\%$, which, multiplied by a t-factor of 2.78, would result in an uncertainty of 8.34% without even considering the other sources. To replicate these calculations, Equations (3.61) and (6.1) can be substituted into Equation (3.67), setting $\sigma_f = \sigma_m = 0$.

As stated above, to reduce the overall uncertainty it is necessary to reduce the frequency uncertainty $\sigma_f$. If $\sigma_f$ is reduced from 0.01 Hz to 0.005 Hz while keeping all other input uncertainties unchanged, the uncertainty minimums almost halve. The minimum for $\rho^2 = 1 \cdot 10^5 mm^2$ then becomes 8.63%, with $\zeta_{opt} = 300mm$, while for $\rho^2 = 5 \cdot 10^5 mm^2$ it becomes 11.52%, with $\zeta_{opt} = 541mm$. Intermediate radii of gyration will result in intermediate minimum uncertainties. For example, the OTV's $\rho^2 = 3.1 \cdot 10^5 mm^2$ achieves a $\sigma_f$ of 10.73% at $\zeta_{opt} = 467mm$. This is still insufficient to satisfy the requirements.

The uncertainty must then be further reduced to $\sigma_f = 0.003Hz$. This yields, for $\rho^2 = 3.1 \cdot 10^5 mm^2$, the plot in Figure 6.4. In this case, the minimum uncertainty for $\rho^2 = 3.1 \cdot 10^5 mm^2$ is 6.76%, with $\zeta_{opt} = 511mm$.

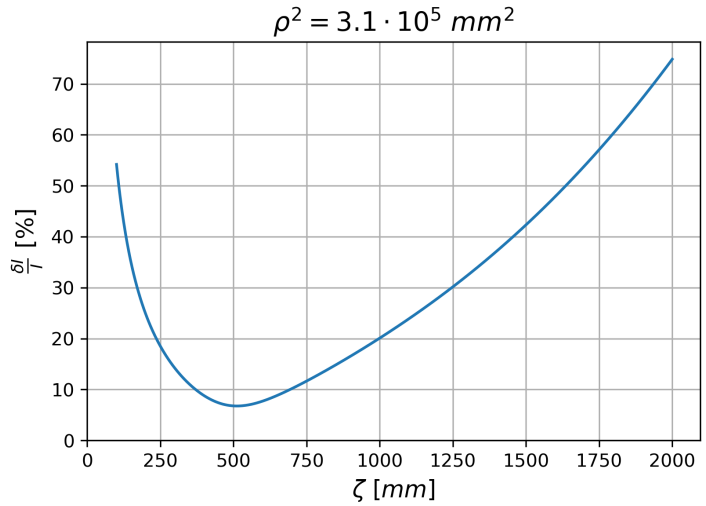


**Figure 6.4:** MoI uncertainty as a function of $\zeta$ for $\rho^2 = 3.1 \cdot 10^5 mm^2$, $\sigma_m = 0.15kg$, $\sigma_\zeta = 20mm$, $\sigma_f = 0.003Hz$

For a fixed value of $\rho$, a gradual increase in $\zeta_{opt}$ can be observed with decreasing $\sigma_f$. This is due to the reducing influence of $\sigma_f$ as the other two input uncertainties are left unchanged. As discussed before in this section, the optimum $\zeta$ depends on $\sigma_f$ and $\sigma_\zeta$. As $\sigma_f$ gets smaller, the effect of $\sigma_\zeta$ increases. As a result, $\zeta_{opt}$ approaches $\zeta_{opt,\zeta}$.

Based on the study presented in this section, in order to comply with the uncertainty constraint of 10% introduced in Section 2.1, the standard uncertainty on the oscillation frequency should be 0.003Hz or smaller in the OTV CP tests. The OTV tests were designed to achieve this requirement.

## 6.2. Test Time Optimization

There are two ways to increase the accuracy of the frequency acquisition and achieve the desired frequency uncertainty:

- Increasing the number of acquisitions

- Increasing the length of each acquisition.

The former decreases the standard deviation of the best estimate, as shown in Equation (3.6), as well as the t-factor needed to achieve the desired confidence level. The latter decreases the uncertainty on the single frequency measurement according to Equation (2.17). To determine the optimum number and duration of the tests, a trade-off between the two must be performed.

Substituting Equation (3.13) into Equation (3.15) yields the following equation for the frequency uncertainty:

$$\sigma_f^2 = \frac{1}{\sum_i \frac{1}{\sigma_{f_i}^2}} \tag{6.3}$$

Now, assuming the uncertainty due to the frequency resolution of the FFT algorithm is a measure of its standard uncertainty $\sigma_{f_i} \approx \delta f_i$, Equation (2.17) can be substituted into Equation 6.3, yielding

$$\sigma_f^2 = \frac{1}{\sum_i t_{acq,i}^2} \tag{6.4}$$

If all acquisitions are carried out for approximately the same amount of time, it can be assumed that $t_{acq,i} = t_{acq,j} = t_{acq}$. Then, for $N$ acquisitions, $\sum_i t_{acq,i}^2 = N \cdot t_{acq}^2$. Substituting into Equation (6.4) and taking the square root:

$$\sigma_f = \frac{1}{\sqrt{N} \cdot t_{acq}} \tag{6.5}$$

This is an expression of the standard deviation of the best estimate of the frequency. To take into account the effect of the t-factor, the combined uncertainty on the MoI must be introduced. This is calculated through Equation (3.66). However, since it has been determined in Section 6.1 that the contributions of $\sigma_m$ and $\sigma_\zeta$ are much smaller than that of $\sigma_f$, it can be assumed that $\sigma_I \approx \frac{\partial I}{\partial f}\sigma_f$. This, substituted into Equation (3.8), results in the following expression for the total uncertainty on the MoI for a given confidence level:

$$\delta I = t_p \cdot \frac{\partial I}{\partial f}\sigma_f \tag{6.6}$$

Substituting Equation (6.5) into the above yields:

$$\delta I = \frac{\partial I}{\partial f}\frac{t_p}{\sqrt{N} \cdot t_{acq}} \tag{6.7}$$

For each repetition of the test, the total time required will be a sum of the acquisition and setup times. If the setup time is assumed to be a fixed fraction of the acquisition time, the total time required by each test will be

$$t_{test,i} = c_1 \cdot t_{acq} \tag{6.8}$$

Where $c_1 > 1$ is a non-dimensional constant.

Then, the total testing time required for $N$ repetitions of the test can be expressed as

$$t_{tot} = N \cdot c_1 \cdot t_{acq} \tag{6.9}$$

Reordering and substituting this into Equation (6.7) yields

$$\delta I = \frac{\partial I}{\partial f}\frac{\sqrt{N} \cdot t_p \cdot c_1}{t_{tot}} \tag{6.10}$$

Since $\frac{\partial I}{\partial f}$ is not dependent on $t_{acq}$ or $N$ it can be grouped with $c_1$ into a new constant $c_2 = \frac{\partial I}{\partial f}c_1$. Then, reorganizing the equation, an expression of the total testing time can be obtained.

$$t_{tot} = c_2\frac{\sqrt{N} \cdot t_p}{\delta I} \tag{6.11}$$

Therefore, for a given required value of $\delta I$, the number and length of the tests can be optimized by minimizing the numerator $\sqrt{N} \cdot t_p$.

Since $\sigma_f$ is the dominant source of uncertainty, the t-factor for the combined uncertainty can be assumed to be the same as for the frequency. Therefore, assuming the $N$ acquisitions are independent, the degrees of freedom are determined by Equation (3.7). The optimum number of tests $N_{opt}$ can then be calculated. Table 6.1 shows the values of $\sqrt{N} \cdot t_p$ for a confidence level of 95%, up to $N = 10$. The lowest value is achieved for $N_{opt} = 5$. Given the above assumptions are valid, this is a general result for the CP. No specific parameters were introduced at this stage. Moreover, this result is valid to minimize the frequency-dependent uncertainties in the BFP as well.

**Table 6.1:** Determination of the optimum number of tests to minimize testing time for the CP. The lowest value in the third column identifies $N_{opt}$

| $N$ | $t_p$ | $\sqrt{N} \cdot t_p$ |
|---|---|---|
| 2 | 12.71 | 17.97 |
| 3 | 4.30 | 7.45 |
| 4 | 3.18 | 6.36 |
| 5 | 2.78 | 6.22 |
| 6 | 2.57 | 6.30 |
| 7 | 2.45 | 6.48 |
| 8 | 2.36 | 6.68 |
| 9 | 2.31 | 6.93 |
| 10 | 2.26 | 7.15 |

. (All values in this table are non-dimensional)

To determine the minimum acquisition time $t_{acq}$ required to achieve the desired frequency uncertainty $\sigma_f$, Equation (6.5) needs to be reorganized as

$$t_{acq} = \frac{1}{\sqrt{N} \cdot \sigma_f} \tag{6.12}$$

Here, $N = N_{opt} = 5$ from the results above. The minimum standard uncertainty on the frequency $\sigma_f$ has been calculated in Section 6.1 as $0.003Hz$. This results in an acquisition time of $149.07s$. For the validation campaign, the number of acquisitions was set as $N = 6$, and the acquisition time as $t_{acq} = 200s$, to be slightly more conservative and allow for the removal of noisy portions of the signal.

# 7

# Validation Campaign

The validation campaign was conducted on the OTV's primary structures, to validate the testing methodology for the specific use case for which it was developed. In this campaign, the ropes for the static tests were assembled the same way as in the pre-validation campaign, while the ones for the dynamic tests did not include turnbuckles, since in the previous tests this component showed an overly rigid behavior. The ropes were clipped directly around the eye bolts in order for their behavior to resemble as much as possible that of an ideal rope. The rope length was chosen so that it would result in a pendulum arm length close to the optimum one calculated in Section 6.1, while the motion acquisition was taken 6 times for a total of 200 s, to comply with the guidelines from Section 6.2. All reported uncertainties refer to a confidence level of 95%.

## 7.1. Test Objectives and Success Criteria

The test campaign had the following objectives:

- Validate the testing methodology for specific use on the Redshift OTV, with respect to the following:
  - Total cost
  - Total testing times
  - Uncertainties on mass, CoG, MoI
- Identify criticalities and possible future improvements

Given the test objectives, the test campaign would be declared successful based on the following success criteria:

- Mass, CoG and MoI values are obtained, with justified uncertainty values and confidence levels
- All applicable requirements are satisfied
- No damage occurs to the tested object, based on visual inspection

## 7.2. Mass and CoG Tests

The MPW and BS tests were conducted with no relevant variations from the previous iteration. The results are accurate and no major criticalities arose. Compared to the pre-validation campaign, the use of more accurate measuring equipment, especially in the measurement of the tilt angles, allowed even lower uncertainties to be achieved. Furthermore, such high precision was achieved without rotating the body three times to compensate for possible systematic errors in the load cells, as had been done in the pre-validation campaign. The combined results from the two tests are listed in Table 7.1. Here, it is relevant to note the small error on $z_G$, made possible by a much larger tilt $\beta$ compared to the tests on the ESPA (see Section 3.2.1).

**Table 7.1:** Combined Results for Mass and CoG

| Parameter | Value | Fractional Uncertainty | Deviation from CAD |
|---|---|---|---|
| $m$ | $78.43 \pm 0.18$ kg | $0.23\%$ | $-0.73\%$ |
| $x_G$ | $809.59 \pm 1.64$ mm | $0.09\%$ | $-0.10\%$ |
| $y_G$ | $468.03 \pm 1.78$ mm | $0.09\%$ | $-0.02\%$ |
| $z_G$ | $268.91 \pm 3.63$ mm | $0.54\%$ | $-1.13\%$ |

## 7.3. Bifilar Pendulum

The BFP acquisition was repeated 6 times. The measured set of frequencies shows a high precision, meaning that the uncertainty on each measured value as well as on the final result are satisfactory. However, the measured MoI differs considerably from the CAD value $I_{CAD} = 41.83kg \cdot m^2$.

Since the OTV's diameter is very close to the width of the rig, the two ropes supporting the body in the BFP configuration were almost perfectly vertical, with angles smaller than $1°$. This is an advantage. The cosine of angles smaller than $5°$ is so close to 1 that the exact value of the rope tilt can be entirely neglected, removing it as a source of uncertainty.

**Table 7.2:** Measured input parameters and calculated MoI in OTV BFP test

| Parameter | Value | Fractional Uncertainty | Deviation from CAD |
|---|---|---|---|
| $a$ | $960.00 \pm 1.00$ mm | - | - |
| $b$ | $937.00 \pm 1.00$ mm | - | - |
| $m$ | $78.43 \pm 0.18$ kg | - | - |
| $h$ | $738.41 \pm 3.01$ mm | - | - |
| $f$ | $0.864 \pm 0.019$ Hz | - | - |
| $I$ | $31.75 \pm 1.42$ kg · m$^2$ | $4.47\%$ | $-24.09\%$ |

The measured input parameters and the calculated MoI are reported in Table 7.2. The MoI uncertainty is low, but presents a high deviation from the MoI value predicted by the CAD. As argued in more detail in Section 5.4, such a high deviation is implausible, given the high level of accordance displayed by the static tests. An undetected source of errors must then be impacting the results. Given that the geometrical constraints are directly measured with quite high confidence, and the mass was obtained with low uncertainty, the frequency is the only plausible cause for this effect. However the oscillation frequency expected from a body with $I = I_{CAD}$, obtained from inverting Equation (2.4) is $f_{exp} = 0.753Hz$, much lower than the measured one.

## 7.4. Compound Pendulum

The CP method was performed with 6 acquisitions for both the pitch and the yaw configurations. Similarly to the BFP test, it yielded precise (low uncertainty) results, but displayed low accordance with the CAD predictions. The input values and results are presented in in Table 7.3.

**Table 7.3:** Results of CP tests on OTV

| Parameter | Value | Fractional Uncertainty | Deviation from CAD |
|---|---|---|---|
| $\zeta_{\text{pitch}}$ | $810.91 \pm 3.22\,mm$ | - | - |
| $f_{\text{pitch}}$ | $0.497 \pm 0.005\,Hz$ | - | - |
| $I_{\text{P,pitch}}$ | $63.95 \pm 1.29\,kg \cdot m^2$ | - | - |
| $I_{\text{pitch}}$ | $12.37 \pm 1.25\,kg \cdot m^2$ | $10.08\%$ | $-50.34\%$ |
| $\zeta_{\text{yaw}}$ | $809.91 \pm 3.22\,mm$ | - | - |
| $f_{\text{yaw}}$ | $0.489 \pm 0.003\,Hz$ | - | - |
| $I_{\text{P,yaw}}$ | $66.01 \pm 0.91\,kg \cdot m^2$ | - | - |
| $I_{\text{yaw}}$ | $14.57 \pm 0.84\,kg \cdot m^2$ | $5.78\%$ | $-41.23\%$ |

The body could not be tested as $\zeta = \zeta_{opt}$ due to geometrical constraints on the test rig. Instead,

$\zeta \approx 810mm$ was achieved. According to the study performed in Section 6.1, this $\zeta$ value would result in a MoI uncertainty of 13.5%. However, lower measurement uncertainties were achieved in this campaign compared to the previous ones. This led to lower combined uncertainties of about 10% for the pitch configuration and less than 6% for the yaw configuration. In particular, the acquisition length of 200s determined a very high repeatability in the frequency measurement, achieving standard uncertainties of $\sigma_{f,\text{pitch}} = 0.002Hz$ and $\sigma_{f,\text{yaw}} = 0.001Hz$ (68% confidence).

The measured MoI values deviate considerably from the predicted $I_{CAD}$, with the former being about half of the latter. As in the BFP test, the oscillation frequency is the only possible cause of this effect. The mass has too little influence on the results, while no real value of $\zeta$ exists that would result in $I = I_{CAD}$. Inverting the solution Equation (2.8) in order to find the expected oscillation frequency for a body of mass $m_{CAD}$ and MoI $I_{CAD}$, results in $f_{exp} = 0.455Hz$. This is also confirmed by the results of a dynamic simulation run on the OTV, similar to the one described in Section 4.4. However, this value is incompatible with the frequency uncertainty, even for a 5-sigma interval. Furthermore, the recordings confirm the body was swinging at the measured frequency, and not at the expected one. It follows that a neglected physical effect was causing the body to consistently oscillate at a faster frequency than expected.

## 7.5. Hollow Beam Campaign

All performed BFP and CP tests, both on the ESPA and on the OTV structures, yielded consistently lower MoI values compared to the predictions. This has been found to be a symptom of systematic errors on the oscillation frequency which were not accounted for in the analytical derivations in Chapter 3.

A possible explanation for the observed deviations was offered by a NASA paper [29] reporting a significant dependency of the measured frequency on the oscillation amplitude in CP tests. The frequency was observed to gradually reduce with increasing amplitude, with a measured shift of about 0.05Hz determining a MoI shift of 70%. Interestingly, the authors report a very high amplitude dependency at low amplitudes, while the measurements stabilize for larger amplitudes, while at the same time approaching the expected value. This is contrary to the generally accepted notion that measurements on small oscillations are more reliable in virtue of their more linear behavior. Additionally, it is in contradiction with the findings of the equivalent linearizations presented in Chapter 3, as well as with the simulation study presented in Chapter 4, both of which associate a higher accuracy to lower oscillation amplitudes.

A test campaign was conducted in order to shed light on these apparently contradictory findings and determine if they could be causing the observed deviations from the predicted values. The chosen test item for the campaign is a simple square hollow beam of outer dimensions 2000x70x70 mm and wall thickness 4mm, made of stainless steel. The extremely simple geometry of this body allows for the accurate analytical prediction of the inertia parameters, making large deviations such as the ones observed during the OTV tests unacceptable. Given the proven accuracy of the static methods, these were not performed on the beam. The mass of the object was obtained by simply weighing it on a scale, while the CoG was assumed to be at the geometrical centroid of the body. Then, all three principal moments of inertia were measured. The BFP measured one of the two transverse MoI, while two configurations of CP were used for the longitudinal and the other transverse MoI. Each of the three principal MoI values of the beam can be calculated as the difference between the corresponding MoI of two rectangular cuboids with the same length as the beam, one of which has thickness $t = t_{ext}$, while the other has $t = t_{int}$, where $t_{ext}$ is the outer thickness of the beam, while $t_{int}$ is its inner thickness, or the thickness of the hollow part. The MoI of a rectangular cuboid of dimensions $a$, $b$, and $c$, around the axis parallel to $c$ and passing through its CoG is[1]

$$I_c = \frac{1}{12} m(a^2 + b^2) \tag{7.1}$$

Other than investigating the aforementioned frequency shift, the tests gathered data to further assess the influence of the CP arm length and the rope type. Furthermore, the test item features a very

[1] Source: `https://www.mikipulley.co.jp/EN/Services/Tech_data/tech24.html` (accessed on 19/10/2023)

large difference between the MoI about the longitudinal axis and those about the two transverse axes, allowing for the comparison of results obtained for different radii of gyration.

### 7.5.1. Bifilar Pendulum

The BFP test was performed first using steel wire ropes with no turnbuckles, as in Figure 7.1, and then using slings of two different lengths. In all cases, the mounting radii on the structure and on the body were equal ($a = b = 400mm$).

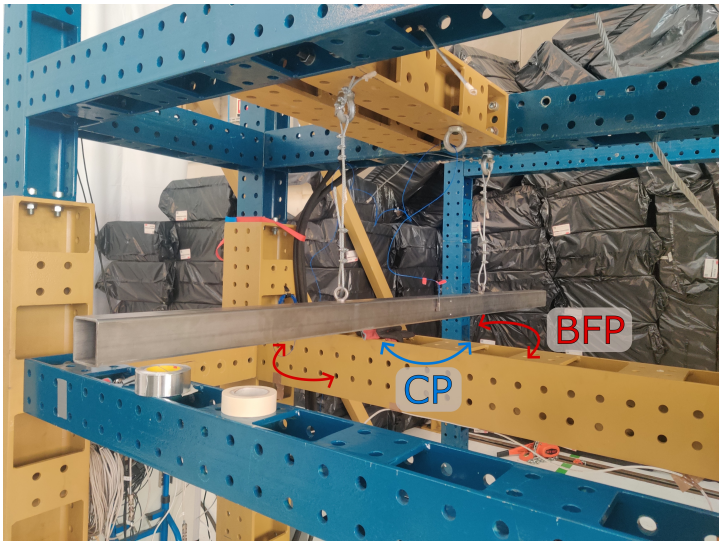


**Figure 7.1:** Steel ropes configuration for BFP and longitudinal CP for hollow beam

Table 7.4 reports the results from the three configurations. Here, $L$ is the length of the ropes, and $\Delta f_{shift}$ is the maximum observed frequency shift. As in the previous tests the measured MoI is smaller than the predicted one, meaning the oscillation frequency is larger than the expected one. The measured MoI values and their uncertainties have been compared with the predicted MoI $I_{CAD} = 5.64kg{\cdot}m^2$ and show deviations too large to be attributed only to the differences between the ideal and real body.

**Table 7.4:** Results from the BFP tests on the hollow beam

| | $L\ [mm]$ | $I\ [kg \cdot m^2]$ | $\frac{\delta I}{I_{CAD}}$ | $\frac{I - I_{CAD}}{I_{CAD}}$ | $\Delta f_{shift}\ [Hz]$ |
|---|---|---|---|---|---|
| Short slings | 225.75 | 4.15 | 58.34% | −26.56% | 0.206 |
| Steel ropes | 421.60 | 4.55 | 11.36% | −19.32% | 0.143 |
| Long Slings | 1439.00 | 4.80 | 29.31% | −14.92% | 0.007 |

The results are consistent with the observations in Section 5.4, which saw a smaller deviation from the predictions at longer rope lengths. The precision also improves, with an uncertainty achieved with longer slings of about half of that obtained with the short ones. For the steel ropes, the uncertainty drops even further. Based on these results, a test with long, steel ropes is expected to yield lower uncertainties and deviations from the CAD.

Table 7.4 also presents the values of the observed frequency shift between the maximum and minimum amplitudes tested. The abovementioned paper [29] did not observe this effect in their tests, but here it was found to be quite significant. Even the apparently small shift observed for the long slings causes the MoI to increase by almost 5%. One issue, however, is that the frequencies show very weak convergence. Most plots exhibit a behavior resembling that of Figure 7.2a in which a weak convergence could be assumed at high amplitudes, but without certainty. The remaining ones appear roughly linear, like in Figure 7.2b, exhibiting no signs of convergence. Based on this data, no conclusions can be drawn on whether the frequency shift stabilizes at high amplitudes for the BFP method.

However, the downward trend is observed in all cases. This can be partly due to the nonlinear

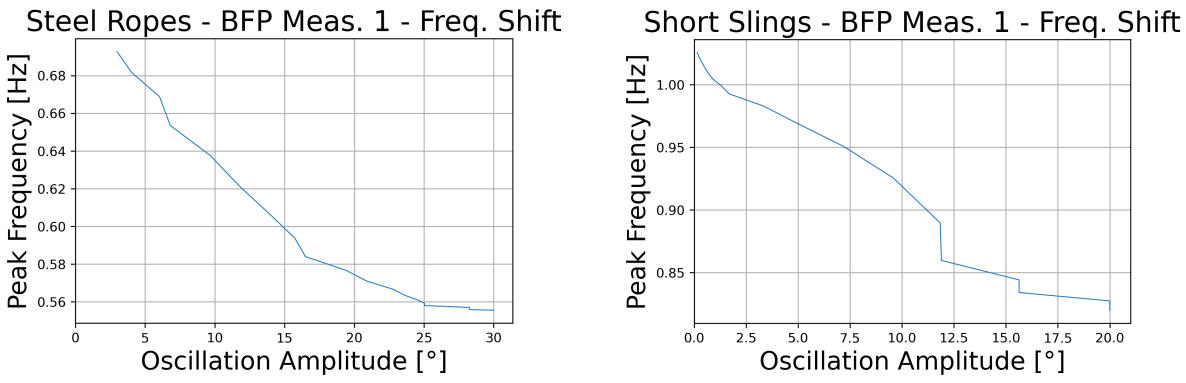


**(a)** Weak convergence

**(b)** No convergence

**Figure 7.2:** Examples of frequency shift plots in BFP tests with hollow beam

effect of the amplitude on the frequency previously discussed in Section 3.2.2, but this only contributes in small part. Figure 7.3 compares the derived backbone with the measured shift. It is clear from the figure that the experimental shift is both larger in scale and shifted towards higher frequencies.

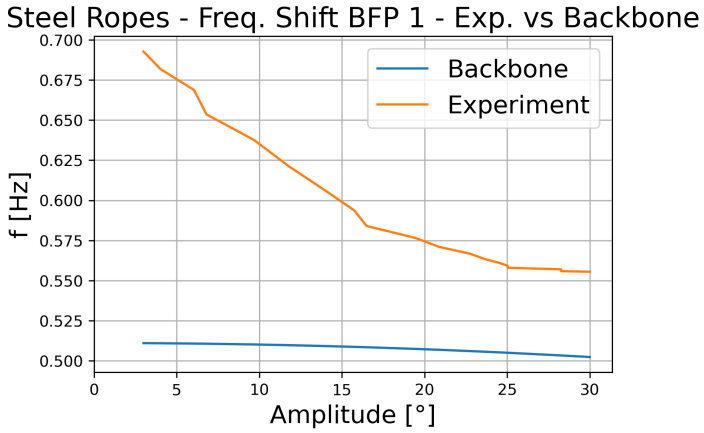


**Figure 7.3:** Comparison between BFP backbone and experimentally measured frequencies

## 7.5.2. Compound Pendulum

The CP method was implemented in both the longitudinal and transverse orientation, first with steel ropes of short length, and then with slings of increasing length. Given the low thickness of the object, only two ropes were used instead of the usual four. In all tests, the motion acquisition was repeated 6 times.

### Longitudinal MoI

The configuration used to measure the longitudinal MoI of the beam is the same as the BFP one, shown in Figure 7.1. The body is pushed in the direction perpendicular to the beam axis. The pendulum axis is therefore parallel to the axis of the beam.

The beam's radius of gyration about this axis is very small, at $\rho_L = 39.67mm$. As discussed in Section 6.1, a small radius of gyration determines a low optimum pendulum length $\zeta_{opt}$. As illustrated in Figure 7.4, in this case, $\rho_L$ is so small that the optimum length is almost 0 mm, making it unachievable. Furthermore, the uncertainties grow very quickly to above 100%.

The expected MoI of the body in this orientation is $I_{CAD} = 2.46 \cdot 10^4 kg \cdot mm^2$, while the Steiner term is, even for the shortest sling length, $m\zeta^2 = 122.04 \cdot 10^4 kg \cdot mm^2$, which is almost 50 times larger. This

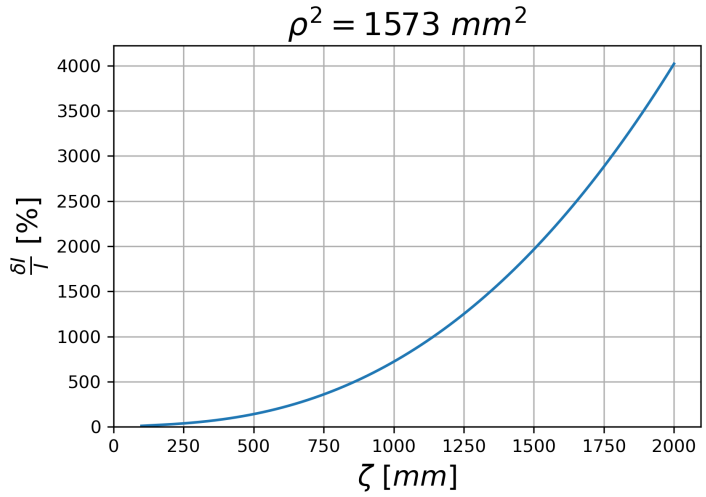


**Figure 7.4:** MoI uncertainty for the hollow beam as a function of $\zeta$, for $\sigma_m = 0.01kg$, $\sigma_\zeta = 0.7mm$, $\sigma_f = 0.001Hz$

large disproportion made it impossible to achieve acceptable results, and caused the measured MoI to reach even more negative values than in the first tests on the ESPA. Nonetheless, the results in Table 7.5 helped to achieve a deeper understanding of the CP method.

**Table 7.5:** Results from longitudinal CP tests

| | $\zeta$ [$mm$] | $I$ [$kg \cdot mm^2$] | $\frac{\delta I}{I_{CAD}}$ | $\frac{I - I_{CAD}}{I_{CAD}}$ | $\Delta f_{shift}$ [$Hz$] | $I_{stab}$ [$kg \cdot mm^2$] |
|---|---|---|---|---|---|---|
| Short slings | 279.25 | -2.89 $\cdot 10^4$ | 1254.47% | -217.55% | 0.017 | Not converged |
| Medium slings | 475.10 | -5.16 $\cdot 10^4$ | 3216.44% | -309.61% | 0.163 | Not converged |
| Long slings | 1122.50 | -47.53 $\cdot 10^4$ | 6579.71% | -2030.34% | 0.013 | -17.77 $\cdot 10^4$ |
| Very long slings | 1492.50 | -65.18 $\cdot 10^4$ | 7916.37% | -2747.10% | 0.010 | 12.88 $\cdot 10^4$ |
| Steel ropes | 475.10 | -11.77 $\cdot 10^4$ | 219.98% | -578.20% | 0.134 | 2.26 $\cdot 10^4$ |

Firstly, the results from the sling tests show a very clear $\zeta$-dependency of the MoI uncertainty $\delta_I$ and difference from the predictions ($I - I_{CAD}$). Both of these are presented in Table 7.5 as a percentage of the expected value, for ease of interpretation. As expected, both improve with shorter sling length. However, regardless of the pendulum length, all measured MoI are smaller than the predictions. The steel ropes, of roughly the same length as the medium slings, obtained considerably smaller uncertainties, with the difference being more than a factor of 10. The slings of medium length did yield a MoI value closer to the predictions, but with such high uncertainty ($\delta I > 10|I - I_{CAD}|$), the accuracy of a measurement is indicative at best.

The amplitude-dependent frequency shift is evident from the graphs. Almost all tests show a very clear stabilization trend, as exemplified by Figure 7.5 for a test with steel ropes. Despite this, however, the converged results $I_{stab}$ are still not sufficiently close to the predictions to be acceptable. The converged result for the steel ropes is within 10% of the expectations, but the uncertainties are so high that the result is meaningless. Another notable finding of this frequency shift study is the very high amplitude dependency registered at low amplitudes. In the acquisition plotted in Figure 7.5, the acquired frequency at an amplitude of 2° is almost 0.01 Hz higher than at an amplitude of 2.5°. This causes an MoI shift $\Delta I = 9.3kg \cdot mm^2 = 3.79 \cdot I_{CAD}$. It follows that such measurements are completely unreliable.

### Transverse MoI

To measure the transverse MoI, the beam was suspended by two ropes connected on the same point on the rig, like an inverted V. The setup is shown in Figure 7.6 with slings. In this orientation, $I_{CAD} = 5644311.55kg \cdot mm^2$, and the radius of gyration is $\rho = 600.55mm$, quite close to that of the tested OTV structures. The higher radius of gyration made it possible to test the body with the optimum rope length.

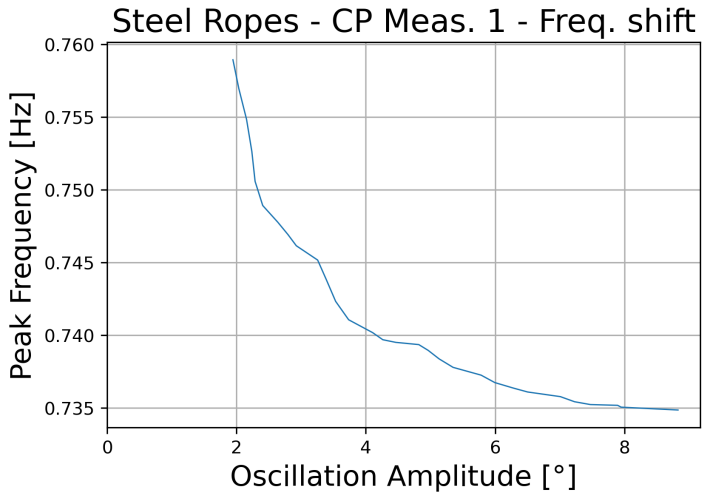


**Figure 7.5:** Example of frequency shift plot in longitudinal CP tests with hollow beam

**Figure 7.6:** CP with slings, measuring the transverse MoI of the hollow beam

Table 7.6 shows all results. The first thing that can be noticed is that all tests yielded sufficiently low uncertainties, with the optimum and medium-sized slings being the ones with the lowest spread in the results. Despite this, the deviations from the predictions are all above 20%, which is not plausible for such a simple test object. This makes it clear that, while a high radius of gyration and an optimized rope length can minimize uncertainties and increase the overall accuracy, they can still not be sufficient to achieve accurate measurements.

Like in most of the previous measurements, the steel ropes achieved lower uncertainties and higher accordance with the predictions compared to slings of equal length. This is an important result, as it proves that this suspension system is consistently better than the slings, which were previously shown to yield better results than the steel ropes with turnbuckles equipped. This means that the rope type has a large impact on the results. The equations are based on an idealized model of the test, in which the ropes are represented by inextensible segments which swing without friction, bending, or torsion. On the other hand, the real system presents all these effects, with bending being especially observed in the tests featuring turnbuckles, at the attachment between the rope and the rigid component, and torsion being observed in the tests with slings, which feature two different bending stiffnesses causing them to twist to face the swinging direction with the least stiff side. It makes sense, then, that the most accurate results would come from the setup that most resembles the idealized rope: a steel rope

**Table 7.6:** Results from longitudinal CP tests

| | $\zeta\ [mm]$ | $I\ [kg \cdot m^2]$ | $\frac{\delta I}{I_{CAD}}$ | $\frac{I - I_{CAD}}{I_{CAD}}$ | $\Delta f_{shift}\ [Hz]$ | $I_{stab}\ [kg \cdot m^2]$ |
|---|---|---|---|---|---|---|
| Short slings | 218.60 | 2.60 | 6.80% | -42.53% | 0.063 | Not converged |
| Optimum slings | 306.00 | 3.77 | 0.90% | -33.26% | 0.019 | Not converged |
| Medium slings | 414.80 | 4.01 | 0.49% | -28.93% | 0.061 | 4.38 |
| Long slings | 636.80 | 3.94 | 4.16% | -30.28% | 0.022 | 4.56 |
| Very long slings | 1470.00 | 4.31 | 8.31% | -23.71% | 0.004 | 4.84 |
| Steel ropes | 220.40 | 3.46 | 4.89% | -38.66% | 0.106 | 3.73 |

forming a direct connection between rig and body.

Again, all measured MoI were smaller than the predicted values due to the body swinging at higher frequencies than expected. The most accurate results, i.e., the closest to the predictions, have been achieved for the longest slings. This appears to be in contradiction with the discussion in Section 6.1, which maintained that the pendulum should be brought as close as possible to the optimum length. However, the optimum $\zeta$ was calculated to minimize known uncertainty sources, related mainly to the explicit parameters in the solution equation. As shown in Table 7.6, the results present very low uncertainty for $\zeta \approx \zeta_{opt}$. The large discrepancies with the predictions are due to a source of large systematic errors which was not accounted for during uncertainty analysis.

The study of the frequency shift yielded conflicting results in this case. Almost all tests yielded converging graphs. However, the convergence only partially improved the accuracy of the results. The most accurate are achieved by the longest slings, which, after convergence, show a deviation of -14.19%. Again, this deviation is too large to be considered a simple consequence of modeling imperfections. In particular, the tests performed with steel ropes all resulted in a strong convergence at high amplitudes. On the other hand, all tests performed with the optimum pendulum length resulted in graphs similar to the one in Figure 7.7, from which no clear trend can be extracted.

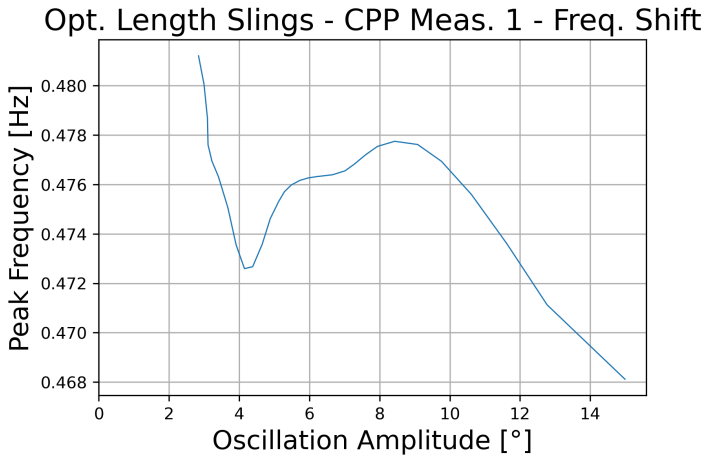


**Figure 7.7:** Frequency shift plot in transverse CP tests with hollow beam, $\zeta = \zeta_{opt}$

## 7.6. Requirements Satisfaction Matrix

Table 7.7 shows the requirements pertaining to the OTV test campaign, as well as their verification methods and satisfaction statuses. As in the pre-validation campaign (see Section 5.6), almost all requirements are verified. In particular, requirements P1-P4, relative to the mass and CoG coordinates, are satisfied with even wider margins, since the uncertainties on these measurements are smaller than previously achieved. Requirement P5 is satisfied, thanks to the low uncertainties achieved by the BFP method in the tests on the OTV. Requirement P6 is, as in the tests on the ESPA, not verified, even though this time the uncertainty was only slightly above 10%. Requirement P7 is satisfied, thanks to

the low uncertainties achieved in the Yaw MoI test.

**Table 7.7:** Requirements satisfaction matrix for the inertia testing campaign on the OTV

| ID | Statement | Verification Method | Satisfied |
|---|---|---|---|
| F1 | The procedure shall provide sufficient data to determine the mass of the vehicle. | Test | Yes |
| F2 | The procedure shall provide sufficient data to determine the CoG coordinates of the vehicle. | Test | Yes |
| F3 | The procedure shall provide sufficient data to determine the MoI of the vehicle about its specified roll, pitch, and yaw axes. | Test | Yes |
| F4 | The results shall include justified uncertainty values. | Uncertainty analysis | Yes |
| P1 | The total uncertainty on the mass measurement shall be below 10% of the measured value. | Uncertainty analysis | Yes |
| P2 | The total uncertainty on the determination of the $x$ coordinate of the CoG coordinate shall be below 10% of the vehicle's maximum dimension in $x$ direction. | Uncertainty analysis | Yes |
| P3 | The total uncertainty on the determination of the $y$ coordinate of the CoG coordinate shall be below 10% of the vehicle's maximum dimension in $y$ direction. | Uncertainty analysis | Yes |
| P4 | The total uncertainty on the determination of the $z$ coordinate of the CoG coordinate shall be below 10% of the vehicle's maximum dimension in $z$ direction. | Uncertainty analysis | Yes |
| P5 | The total uncertainty on the measurement of the roll MoI shall be below 10% of the measured value. | Uncertainty analysis | Yes |
| P6 | The total uncertainty on the measurement of the pitch MoI shall be below 10% of the measured value. | Uncertainty analysis | No |
| P7 | The total uncertainty on the measurement of the yaw MoI shall be below 10% of the measured value. | Uncertainty analysis | Yes |
| E1 | The test setup shall fit the RFA Portugal test facility. | Visual inspection | Yes |
| E2 | The test setup should fit the RFA Germany test facility. | Geometrical measurements | Yes |
| S1 | The full test campaign should not require more than 48 man-hours. | Schedule | Yes |
| C1 | The cost for the company of newly bought hardware shall not exceed €5000. | Cost assessment | Yes |
| C2 | The cost for the company of newly bought hardware should not exceed €1000. | Cost assessment | Yes |

The satisfaction of schedule Requirement S1 can be verified from Table 7.8, listing the approximate time each step of the campaign took with a team of two. The total man-hours employed for the tests is then twice the total from the table, resulting in less than 16 man-hours. Lastly, the functional, cost and environment requirements are also verified, since very little changed in the test setup and procedure

since the previous campaign.

**Table 7.8:** Duration of each step in the OTV test campaign

| Test | Duration |
|---|---|
| Preparation | 90 min |
| Suspended Multi-Point Weighing | 90 min |
| Bifilar Suspension | 40 min |
| Bifilar Pendulum | 90 min |
| Compound Pendulum – Pitch MoI | 90 min |
| Compound Pendulum – Yaw MoI | 75 min |

Since not all requirements were satisfied, the test campaign cannot be declared fully validated. However, the static tests used to determine the mass and CoG of the body yielded very low uncertainties. Therefore, at least these tests can be considered validated.

# 8

# Conclusion

A complete testing methodology for the determination of the mass, Center of Gravity (CoG), and principal Moments of Inertia (MoI) of a small rocket stage was developed, tested, and evaluated. The methodology consists of five consecutive tests, including two static tests and three dynamic ones. The static tests are novel implementations of two widely accepted methods to measure the mass and CoG coordinates of the body: the multi-point weighing (MPW) method and the suspension method. The former has been redesigned into a suspended version, to adapt it to the test setup required by the other four tests, thus also widening its range of applicability. The latter was modified into the Bifilar Suspension (BS) method, with two ropes instead of the usual one, which considerably increases its robustness and the safety of the test item. The three dynamic tests each return the value of one MoI: the roll MoI is calculated through the Bifilar Pendulum (BFP) method, while the pitch and yaw MoI result from two iterations of the Compound Pendulum (CP) method. All methods can be performed on a common test stand with minimal repositioning needed before each new test. As a result, the campaign requires a team of two less than 8 hours to complete, and the extra hardware cost for the company was of less than 300 euros.

## 8.1. Outcome

All methods were subjected to uncertainty analysis to analytically determine the impact of parameters explicitly or implicitly influencing the accuracy of the results. From this phase emerged that the body tilt would be a critical factor in the BS test, while the rope length would highly impact the results of the CP method. Furthermore, the nonlinear effects arising in the dynamic tests due to large oscillations were investigated and an analytical expression for the amplitude-dependency was derived.

Following the analytical uncertainty analysis, a simulation study was performed to verify the validity of the methods, as well as the analytical results of the uncertainty analysis. Both assessments yielded positive results: all virtual tests returned accurate values, hence verifying the procedures and their solution equations, and the propagation of errors agreed closely with the derived uncertainty equations. Furthermore, an amplitude-dependent error growth was detected in both the BFP and CP methods, compatibly with the outcome of the uncertainty analysis. In the CP method, these errors were observed to scale with the pendulum arm length.

The validation phase of the developed methodology consisted in three consecutive testing campaigns, each investigating different aspects of it. The first campaign was run on a cylindrical payload adapter, suspended by steel ropes equipped with turnbuckles for length adjustment. The second was run on the primary structure of an OTV, RFA's Redshift, using steel ropes with no turnbuckles. Lastly, the dynamic tests were run on a simple hollow square beam alternately suspended by different rope types to better understand their influence on the accuracy and precision of the results. The static tests consistently yielded acceptable results, proving the mass and CoG coordinates can be determined with a maximum uncertainty of 0.54%. In particular, the uncertainty on the CoG height $z_G$ saw a large reduction when the BS test was performed with a high body tilt.

The BFP method was able to achieve uncertainties below 7% in two of the test campaigns, but presented unexpectedly large deviations from the CAD-predicted values, always larger than 10%. Nonetheless, this study led to some notable findings which will contribute to the shared knowledge on this method. For example, it was discovered that the results improve with increasing rope length, both in terms of uncertainty and of agreement with the numerical predictions. Furthermore, from a comparison of all test results it was concluded that, in both the BFP and CP tests, the type of suspension system has a large impact on both the uncertainty and the accuracy of the results. Notably, the MoI errors are always negative, which excludes the possibility of this impact being due to the influence of the added MoI of the ropes. Instead, it is due to the behavior of the rope, and to how much this diverges from the behavior of an ideal rope. The presence of turnbuckles, for example, overly stiffens the rope at the top, causing it to swing in a different way. Out of the three suspension systems tried in this study, the best results were obtained with steel ropes that did not feature any additional rigid parts. These still resulted in too high errors, however, which warrants further study into a more suitable substitute.

The CP method was the main focus of this study, due to the large number of complications that arose from it. In fact, in its first implementation, this method even yielded negative MoI values with uncertainties close to 100% of the expected value. This was attributed to the predominance acquired by the Steiner term within the CP solution equation at high values of the pendulum length $\zeta$. Several repetitions of this method confirmed this fact, as well as revealing that, for bodies with larger radii of gyration, the errors and uncertainties reduced. This was verified by repeating the test on the same item, a hollow steel beam, in two configurations featuring very different radii of gyration. The results improved immensely for the configuration with the highest radius of gyration. Further insight on the influence of the rope length was provided by an optimization study which revealed that, for a given set of input uncertainties, it is possible to calculate the optimum pendulum length $\zeta_{opt}$ that minimizes the combined uncertainty. One more factor highly impacting the CP results is the accuracy of the frequency readings. In fact, even uncertainties of 0.01 Hz were in some cases observed to propagate to very large MoI uncertainties. Lastly, the tests on the hollow beam revealed the amplitude-dependent frequency nonlinearities to be much wider in range and following a different trend compared to the analytical formulation for both the BFP and CP methods. This suggests the presence of an additional source of amplitude-dependent errors, other than the linearization of the equations of motion. Most of the tests show the frequency converging to a stable value at high amplitudes, but the converged value, while closer to the predictions, still presents large errors. The source of these errors could not be conclusively determined, and further study is required on the matter.

Based on the knowledge acquired during this study, some design guidelines were formulated to aid future researchers and engineers obtain more accurate and precise results from CP tests. Firstly, very low uncertainties can be achieved by adapting the test setup to the optimum pendulum length $\zeta_{opt}$. Secondly, for a given set of input uncertainties, a higher radius of gyration results in a lower dependency of the uncertainty on the pendulum length $\zeta$, meaning that acceptable results can be obtained even for $\zeta \neq \zeta_{opt}$. Conversely, bodies with a low radius of gyration exhibit a strong dependency on the pendulum length, leading to very high uncertainties unless the optimum condition is satisfied. In addition, $\zeta_{opt}$ decreases with decreasing radii of gyration. As a result, with a low radius of gyration it can be complicated or even impossible to achieve the optimum condition. Lastly, the ropes or suspension mechanisms used should behave as closely as possible to inextensible segments pinned at the extremes.

## 8.2. Recommendations for Future Work

While this study achieved many of its intended objectives, there are still areas that require further development. The static methods, for example, yielded excellent results. Nonetheless, upcoming studies could investigate the mass and CoG uncertainties obtainable when substituting the suspended MPW step with a second iteration of bifilar suspension, given that the latter method produced lower uncertainties compared to the former. This would also bring the additional advantage of a test methodology whose methods all require only two attachment points on the test rig. The rig could then be simplified from a table-like structure with four legs to an arch-like structure with two legs. This would greatly reduce both the assembly times and the bulkiness of the setup.

On the other hand, all dynamic tests continue to exhibit a strong dependency of the measured

frequency on the oscillation amplitude. This is believed to be largely due to the suspension system not being sufficiently in line with the idealized setup on which the equations are based. Both the tests on the ESPA and on the hollow beam were run using different suspension systems. The ESPA was suspended first by steel ropes with turnbuckles, and then by slings. The hollow beam was suspended by steel ropes with no extra components, and then by slings, as well. The ESPA tests show highly improved results associated with the slings, while the hollow beam tests achieved consistently better results with the steel ropes. Therefore, the best performing system were the steel ropes without turnbuckles. Out of the three this is the most similar to an ideal rope, since the turnbuckle overly stiffened the top part, while the slings present two different bending stiffnesses in the two principal directions. Then, the direction to follow for further improvements is, according to the author, the one that brings the setup closest to the ideal model from which the equations are derived. To do this, bearings should be implemented, possibly on both sides of the rope.

Another topic worthy of being investigated is related to the implementation of the BFP method. As discussed in Section 2.2.3, the choice of the bifilar pendulum over the trifilar or quadrifilar versions was justified by its simplicity, lower requirements on the test rig, and motion regularity. However, this method also presents a disadvantage: the impossibility of adjusting the body tilt outside of the plane of the two ropes. With three or more ropes, the length can be adjusted to ensure the body is vertical and the pendulum oscillation happens about the intended axis. In this thesis, this was assumed not to impact the results in a relevant way, given the almost perfect symmetry of the tested bodies and the relatively low position of the CoG. A CoG very close to the suspension plane, or even above it, would cause the body to tilt or be overturned. The same is true for a CoG whose position is far from the plane of the ropes. Future work could investigate using small weights or other methods to bring the body to a horizontal orientation, subtracting their influence from the obtained results. This would make it possible to exploit the advantages of a BFP setup even for less balanced bodies.

Furthermore, the optimal rope length for the CP was obtained in Chapter 6 through a numerical study, which yielded $\zeta_{opt}$. Then, the rope length was determined by imposing this pendulum arm length on the CAD model of the setup. The shared knowledge on this method would profit from the development of an analytical formula, with the body and the rig parameters as inputs, that directly calculates the rope length required to minimize uncertainty propagation.

Another issue that was encountered with the application of both the CP and BFP methods is the uncertainty on how to correctly measure the physical length of the ropes. In theory, the rope is imagined as a one-dimensional line connecting a point on the rig to a point on the body, as in Figure 2.1. However, reality is more complex, and the body is actually suspended by assemblies of ropes and other parts. It then becomes difficult to determine exactly how much of the rope assembly contributes to the swinging motion and how much is fixed, becoming part of the rig or of the body. This causes uncertainties on the measured length of the ropes. Future work could focus on a dynamic study of pendulums, to extract guidelines on how to correctly measure the length of the swinging portion of the rope.

Additionally, a large fraction of the total time required by the tests was occupied by the direct measurements such as rope tilt, rope length, and such. The testing methodology could benefit from an optimization study to determine how many times each measurement should be repeated for an optimal trade-off between time and accuracy. The use of more advanced instruments should also be considered to reduce the time required by these measurements. For example, laser-tilt sensors are able to measure both distance and tilt at the same time.

Lastly, it is important that future studies investigate the possibility of injection pulling, in which the frequencies of the two systems tend to converge towards one another [30]. This effect could explain the convergence of the non-linear frequency shift at high amplitudes, since a high amplitude oscillation is less easily disturbed. In the case of the pendula studied here, the effect could be due to vibrations in the test rig or to body vibration modes other than the desired one. One source of vibration that could potentially be responsible for this is the undesired oscillation of the body around its other axes. The imperfection of the initial push, as well as external sources such as friction and air resistance, make it impossible to only excite the oscillation about the intended axis. Therefore, the body will necessarily oscillate about other axes too and, in all the tested items, two out of three principal MoI values are very similar, due to the symmetry of the bodies, meaning they will oscillate at similar frequencies.

# References


[1] A. Witze, "2022 was a record year for space launches," *Nature*, vol. 613, no. 7944, pp. 426–426, Jan. 2023, ISSN: 0028-0836. DOI: 10.1038/d41586-023-00048-7. [Online]. Available: https://www.nature.com/articles/d41586-023-00048-7.

[2] "Technical study for use of the Saturn V, Int-21 and other Saturn V derivatives to determine an optimum fourth stage (Space Tug)," NASA, Tech. Rep., 1971.

[3] T. A. Heppenheimer, *The Space Shuttle Decision: NASA's Search for a Reusable Vehicle*. 1999.

[4] R. C. Hibbeler, *Engineering Mechanics: Dynamics*, 14th ed. 2016, pp. 591–595, ISBN: 9780133915389.

[5] J. H. Williams, *Fundamentals of Applied Dynamics*. John Wiley & Sons, 1996, p. 296. [Online]. Available: https://books.google.nl/books?hl=it&lr=&id=axPGDwAAQBAJ&oi=fnd&pg=PA1&ots=JJ45xVVEHF&sig=4iPdHsJGPOqt3nGF03Cyw7RCf8c&redir_esc=y#v=onepage&q&f=false.

[6] C. Schedlinski and M. Link, "A survey of current inertia parameter identification methods," en, *Mechanical Systems and Signal Processing*, vol. 15, no. 1, pp. 189–211, Jan. 2001, ISSN: 0888-3270. DOI: 10.1006/mssp.2000.1345. [Online]. Available: https://www.sciencedirect.com/science/article/pii/S0888327000913451.

[7] G. Genta and C. Delprete, "Some considerations on the experimental determination of moments of inertia," en, *Meccanica*, vol. 29, no. 2, pp. 125–141, Jun. 1994, ISSN: 1572-9648. DOI: 10.1007/BF01007497.

[8] M. Wang, X. Zhang, W. Tang, and J. Wang, "A structure for accurately determining the mass and center of gravity of rigid bodies," English, *Applied Sciences*, vol. 9, no. 12, p. 2532, 2019, ISSN: 2076-3417. DOI: 10.3390/app9122532.

[9] S. Patel and J. Topiwala, "Measuring a centre of gravity of an object using 4 load transducer method," en, *International Journal of Engineering Research and*, vol. V6, no. 01, Jan. 2017, ISSN: 2278-0181. DOI: 10.17577/IJERTV6IS010100. [Online]. Available: http://www.ijert.org/view-pdf/16199/measuring-a-centre-of-gravity-of-an-object-using-4-load-transducer-method.

[10] X. Zhang, H. Yu, W. Tang, and J. Wang, "General mass property measurement equipment for large-sized aircraft," English, *Sensors*, vol. 22, no. 10, 2022, ISSN: 1424-8220. DOI: 10.3390/s22103912.

[11] X. Zhang, M. Wang, W. Tang, and J. Wang, "A flexible measurement technique for testing the mass and center of gravity of large-sized objects," English, *Measurement Science and Technology*, vol. 31, no. 1, 2020, ISSN: 0957-0233. DOI: 10.1088/1361-6501/ab39ee.

[12] D. Modenini, G. Curzi, and P. Tortora, "Experimental verification of a simple method for accurate center of gravity determination of small satellite platforms," English, *International Journal of Aerospace Engineering*, vol. 2018, 2018, ISSN: 1687-5966. DOI: 10.1155/2018/3582508.

[13] L. Zhang, M. Wang, and P. Liu, "Inertia property determination by spectrum analysis of damped oscillation detection signal," 2020. DOI: 10.1049/smt2.12008.

[14] Y. Zhao, B. Zhang, F. Han, H. Tian, X. Yu, and J. Zhu, "Instantaneous characteristics of nonlinear torsion pendulum and its application in parameter estimation of nonlinear system," *Mathematical Problems in Engineering*, 2018. DOI: 10.1155/2018/7858403. [Online]. Available: https://doi.org/10.1155/2018/7858403.

[15] B. Wang, Z. X. Hou, X. Z. Gao, and S. Q. Shan, "The application of inertial measurement unit in inertia parameter identification," *Advanced Materials Research*, vol. 201-203, pp. 974–981, Feb. 2011, ISSN: 1662-8985. DOI: 10.4028/www.scientific.net/AMR.201-203.974. [Online]. Available: https://www.scientific.net/AMR.201-203.974.

[16] M. Gobbi, G. Mastinu, and G. Previati, “A method for measuring the inertia properties of rigid bodies,” en, *Mechanical Systems and Signal Processing*, vol. 25, no. 1, pp. 305–318, Jan. 2011, ISSN: 0888-3270. DOI: 10.1016/j.ymssp.2010.09.004. [Online]. Available: https://www.sciencedirect.com/science/article/pii/S0888327010003092.

[17] L. Tang and W.-B. Shangguan, “An improved pendulum method for the determination of the center of gravity and inertia tensor for irregular-shaped bodies,” en, *Measurement*, vol. 44, no. 10, pp. 1849–1859, Dec. 2011, ISSN: 0263-2241. DOI: 10.1016/j.measurement.2011.09.004. [Online]. Available: https://www.sciencedirect.com/science/article/pii/S0263224111002995.

[18] C. Blanes, A. Correcher, P. Beltrán, and M. Mellado, “Identifying the inertial properties of a padel racket: An experimental maneuverability proposal,” *Sensors*, vol. 22, no. 9266, p. 9266, Nov. 2022, ISSN: 1424-8220. DOI: 10.3390/S22239266. [Online]. Available: https://doaj.org/article/7d0dc42f68174c0aaa74c8b701e16f63.

[19] M. H. Junos, N. Mohd Suhadis, and M. M. Zihad, “Experimental determination of the moment of inertias of USM e-UAV,” in *Applied Mechanics and Materials*, vol. 465-466, 2014, pp. 368–372, ISBN: 9783037859339. DOI: 10.4028/www.scientific.net/AMM.465-466.368.

[20] R. Gabl, T. Davey, E. Nixon, and D. M. Ingram, “Accuracy analysis of the measurement of centre of gravity and moment of inertia with a swing,” English, *Applied Sciences*, vol. 11, no. 12, 2021, ISSN: 2076-3417. DOI: 10.3390/app11125345.

[21] J. R. Taylor, *An Introduction to Error Analysis: The Study of Uncertainties in Physical Measurements*, English, 2nd ed. Sausalito, California: University Science Books, 1997, ISBN: 978-0-935702-42-2.

[22] H. W. Coleman and W. G. Steele, *Experimentation, Validation, and Uncertainty Analysis for Engineers*, 4th ed. Wiley, 2018. [Online]. Available: https://tudelft.on.worldcat.org/oclc/1137059761.

[23] Joint Committee for Guides in Metrology, *Evaluation of Measurement Data — Guide to the Expression of Uncertainty in Measurement*. 2008, vol. 100:2008, pp. 1–116.

[24] J. L. du Bois, N. A. J. Lieven, and S. Adhikari, “Error analysis in trifilar inertia measurements,” en, *Experimental Mechanics*, vol. 49, no. 4, pp. 533–540, Apr. 2008, ISSN: 1741-2765. DOI: 10.1007/s11340-008-9142-4. [Online]. Available: https://doi.org/10.1007/s11340-008-9142-4.

[25] G. Previati, “Large oscillations of the trifilar pendulum: analytical and experimental study,” en, *Mechanism and Machine Theory*, vol. 156, p. 104 157, Feb. 2021, ISSN: 0094-114X. DOI: 10.1016/j.mechmachtheory.2020.104157. [Online]. Available: https://www.sciencedirect.com/science/article/pii/S0094114X20303748.

[26] G. Dimitriadis, *Introduction to Nonlinear Aeroelasticity*, 1st ed. Chichester, West Sussex, UK: Wiley, 2017. [Online]. Available: http://ebookcentral.proquest.com/lib/delft/detail.action?docID=4817836..

[27] G. Previati, M. Gobbi, and G. Mastinu, “Measurement of the mass properties of rigid bodies by means of multi-filar pendulums – Influence of test rig flexibility,” en, *Mechanical Systems and Signal Processing*, vol. 121, pp. 31–43, Apr. 2019, ISSN: 0888-3270. DOI: 10.1016/j.ymssp.2018.11.011. [Online]. Available: https://www.sciencedirect.com/science/article/pii/S0888327018307313.

[28] Organisation Internationale de Metrologie Légale, *Metrological regulation for load cells*, R 60. 2000.

[29] D. Wolfe and C. Regan, “Frequency shift during mass properties testing using compound pendulum method,” NASA, Tech. Rep., 2012. [Online]. Available: http://www.sti.nasa.gov.

[30] B. Razavi, “A study of injection locking and pulling in oscillators,” in *IEEE Journal of Solid-State Circuits*, vol. 39, Sep. 2004, pp. 1415–1424. DOI: 10.1109/JSSC.2004.831608.

[31] F. Ruggeri, R. S. Kenett, and F. W. Faltin, *Encyclopedia of Statistics in Quality and Reliability*. John Wiley & Sons, Dec. 2007, ISBN: 9780470018613. DOI: 10.1002/9780470061572. [Online]. Available: https://app.knovel.com/hotlink/toc/id:kpESQRV002/encyclopedia-statistics/encyclopedia-statistics.

# A

# Technical Details

This appendix collects some information that does not contribute to the scientific value of the thesis, but that can be useful to recreate the tests in the future.

## A.1. Test Equipment

The following is a list of all the necessary equipment for the testing campaign:

- Test rig
- Rope assembly
  - Wire rope
  - Turnbuckles x4
  - Rope grips for wire rope x24
  - 11mm carabiners x3
- Bolting
  - Load cells eye bolts + washers x6
  - Body eye bolts + washers + nuts x4
  - Rig eye bolts + washers + nuts x3
- Sensors and measurement equipment
  - S-type load cells x3
  - Inclinometer
  - Accelerometer
  - Tape measure

## A.2. Load Cells Calibration

The calibration step was necessary given the load cells were new and did not come with a calibration certificate.

The calibration of each cell was achieved by suspending a crate from it and gradually increasing the load on the cell by placing weights of known value inside the crate. The steps taken for the calibration of each load cell were:

1. Connect the load cell to the test rig using a carabiner through the top eye bolt.
2. Connect slings to the crate.
3. Weigh the crate with slings attached.

4. Weigh the weights and label each with their respective mass.
5. Connect slings to the bottom eye bolt of the load cell.
6. Connect the load cells to the data acquisition system.
7. Place weights one by one, waiting 40 seconds after each new placement for the load cell signal to stabilize. Write down the sequence of placement.
8. Decrease the load by removing the weights in the opposite order (from the last to the first placed).
9. Perform linear regression of data to determine the calibration coefficients.

The loading steps are shown in Table A.1. The weights were added in the order shown, up to a total load of $150.95kg$, which is higher than any load the cells will need to measure during this or the following test campaign.

**Table A.1:** Sequence of weight increase for load cells calibration

| Object | Weight [$kg$] |
|---|---|
| $W_{crate}$ | 13.55 |
| $W_1$ | 19.55 |
| $W_2$ | 19.40 |
| $W_3$ | 19.45 |
| $W_4$ | 19.70 |
| $W_5$ | 19.55 |
| $W_6$ | 10.15 |
| $W_7$ | 10.10 |
| $W_8$ | 9.65 |
| $W_9$ | 9.85 |

The linear regression was performed through a Python script. To assess its quality, the coefficient of determination $R^2$ was used. This is an indicator of how well a regression curve fits the experimental data [31]. It can range from 0 to 1, with 1 being a perfect fit and values close to 0 indicating a very poor one. All three load cells displayed coefficients of correlation larger than 0.99999.

# B

# T-Factors Table

| Degrees of freedom | Fraction $p$ in percent | | | | | |
|---|---|---|---|---|---|---|
| $v$ | 68,27[a)] | 90 | 95 | 95,45[a)] | 99 | 99,73[a)] |
| 1 | 1,84 | 6,31 | 12,71 | 13,97 | 63,66 | 235,80 |
| 2 | 1,32 | 2,92 | 4,30 | 4,53 | 9,92 | 19,21 |
| 3 | 1,20 | 2,35 | 3,18 | 3,31 | 5,84 | 9,22 |
| 4 | 1,14 | 2,13 | 2,78 | 2,87 | 4,60 | 6,62 |
| 5 | 1,11 | 2,02 | 2,57 | 2,65 | 4,03 | 5,51 |
| 6 | 1,09 | 1,94 | 2,45 | 2,52 | 3,71 | 4,90 |
| 7 | 1,08 | 1,89 | 2,36 | 2,43 | 3,50 | 4,53 |
| 8 | 1,07 | 1,86 | 2,31 | 2,37 | 3,36 | 4,28 |
| 9 | 1,06 | 1,83 | 2,26 | 2,32 | 3,25 | 4,09 |
| 10 | 1,05 | 1,81 | 2,23 | 2,28 | 3,17 | 3,96 |
| 11 | 1,05 | 1,80 | 2,20 | 2,25 | 3,11 | 3,85 |
| 12 | 1,04 | 1,78 | 2,18 | 2,23 | 3,05 | 3,76 |
| 13 | 1,04 | 1,77 | 2,16 | 2,21 | 3,01 | 3,69 |
| 14 | 1,04 | 1,76 | 2,14 | 2,20 | 2,98 | 3,64 |
| 15 | 1,03 | 1,75 | 2,13 | 2,18 | 2,95 | 3,59 |
| 16 | 1,03 | 1,75 | 2,12 | 2,17 | 2,92 | 3,54 |
| 17 | 1,03 | 1,74 | 2,11 | 2,16 | 2,90 | 3,51 |
| 18 | 1,03 | 1,73 | 2,10 | 2,15 | 2,88 | 3,48 |
| 19 | 1,03 | 1,73 | 2,09 | 2,14 | 2,86 | 3,45 |
| 20 | 1,03 | 1,72 | 2,09 | 2,13 | 2,85 | 3,42 |
| 25 | 1,02 | 1,71 | 2,06 | 2,11 | 2,79 | 3,33 |
| 30 | 1,02 | 1,70 | 2,04 | 2,09 | 2,75 | 3,27 |
| 35 | 1,01 | 1,70 | 2,03 | 2,07 | 2,72 | 3,23 |
| 40 | 1,01 | 1,68 | 2,02 | 2,06 | 2,70 | 3,20 |
| 45 | 1,01 | 1,68 | 2,01 | 2,06 | 2,69 | 3,18 |
| 50 | 1,01 | 1,68 | 2,01 | 2,05 | 2,68 | 3,16 |
| 100 | 1,005 | 1,660 | 1,984 | 2,025 | 2,626 | 3,077 |
| ∞ | 1,000 | 1,645 | 1,960 | 2,000 | 2,576 | 3,000 |

a) For a quantity $z$ described by a normal distribution with expectation $\mu_z$ and standard deviation $\sigma$, the interval $\mu_z \pm k\sigma$ encompasses $p$ = 68,27 percent, 95,45 percent and 99,73 percent of the distribution for $k$ = 1, 2 and 3, respectively.

**Figure B.1:** Value of $t_p(\nu)$ from the t-distribution for degrees of freedom $\nu$ that defines an interval $-t_p(\nu)$ to $+t_p(\nu)$ that encompasses the fraction $p$ of the distribution [23]

# C

# Compound Pendulum Simulation Results

This appendix presents the results from the simulation of the CP method discussed in Section 4.4. The simulation was repeated for four different values of the rope length $L$. The results regarding $L = 1500mm$ are presented in Table C.1, the ones for $L = 1250mm$ are shown in Table C.2, the ones for $L = 1000mm$ are in Table C.3, and the ones for $L = 800mm$ are in Table C.4. In all tables, $I$ is calculated using the $\zeta$ value resulting from the static simulations, while $I_{\zeta_{CAD}}$ is calculated with $\zeta = \zeta_{CAD}$, directly measured on the CAD model.

**Table C.1:** CP simulation results for $L = 1500mm$

| $A_0$ [°] | $\tau$ [$s$] | $I$ [$kg \cdot m^2$] | $err_I$ | $I_{\zeta_{CAD}}$ [$kg \cdot m^2$] | $err_{I_{\zeta_{CAD}}}$ |
|---|---|---|---|---|---|
| 20 | 2.705 | 3.80 | 45.28% | 3.68 | 40.63% |
| 15 | 2.695 | 3.33 | 27.19% | 3.21 | 22.50% |
| 10 | 2.690 | 3.09 | 18.17% | 2.97 | 13.46% |
| 5 | 2.685 | 2.86 | 9.16% | 2.73 | 4.44% |
| 2 | 2.683 | 2.74 | 4.66% | 2.62 | -0.07% |
| 1 | 2.683 | 2.74 | 4.66% | 2.62 | -0.07% |

**Table C.2:** CP simulation results for $L = 1250mm$

| $A_0$ [°] | $\tau$ [$s$] | $I$ [$kg \cdot m^2$] | $err_I$ | $I_{\zeta_{CAD}}$ [$kg \cdot m^2$] | $err_{I_{\zeta_{CAD}}}$ |
|---|---|---|---|---|---|
| 20 | 2.475 | 3.35 | 27.83% | 3.25 | 24.05% |
| 15 | 2.470 | 3.17 | 21.02% | 3.07 | 17.22% |
| 10 | 2.465 | 2.99 | 14.22% | 2.89 | 10.4% |
| 5 | 2.460 | 2.81 | 7.43% | 2.71 | 3.6% |
| 2 | 2.458 | 2.72 | 4.04% | 2.62 | 0.2% |
| 1 | 2.458 | 2.72 | 4.04% | 2.62 | 0.2% |

**Table C.3:** CP simulation results for $L = 1000mm$

| $A_0$ [°] | $\tau$ [$s$] | $I$ [$kg \cdot m^2$] | $err_I$ | $I_{\zeta_{CAD}}$ [$kg \cdot m^2$] | $err_{I_{\zeta_{CAD}}}$ |
|---|---|---|---|---|---|
| 20 | 2.195 | 3.04 | 16.05% | 2.97 | 13.37% |
| 15 | 2.190 | 2.92 | 11.5% | 2.85 | 8.81% |
| 10 | 2.185 | 2.80 | 6.97% | 2.73 | 4.26% |
| 5 | 2.183 | 2.74 | 4.71% | 2.67 | 1.99% |
| 2 | 2.183 | 2.74 | 4.71% | 2.67 | 1.99% |
| 1 | 2.180 | 2.68 | 2.44% | 2.61 | -0.28% |

**Table C.4:** CP simulation results for $L = 800mm$

| $A_0$ [°] | $\tau$ [$s$] | $I$ [$kg \cdot m^2$] | $err_I$ | $I_{\zeta_{CAD}}$ [$kg \cdot m^2$] | $err_{I_{\zeta_{CAD}}}$ |
|---|---|---|---|---|---|
| 20 | 1.840 | 2.79 | 6.73% | 2.76 | 5.55% |
| 15 | 1.835 | 2.73 | 4.49% | 2.70 | 3.28% |
| 10 | 1.830 | 2.68 | 2.24% | 2.64 | 1.03% |
| 5 | 1.830 | 2.68 | 2.24% | 2.64 | 1.03% |
| 2 | 1.827 | 2.65 | 1.13% | 2.61 | -0.1% |
| 1 | 1.827 | 2.65 | 1.13% | 2.61 | -0.1% |